AZIMUTHAL ANISOTROPY IN HEAVY ION COLLISIONS

A dissertation submitted to

Kent State University in partial

fulfillment of the requirements for the

degree of Doctor of Philosophy

by

Yadav Pandit

December, 2012

Dissertation written by

Yadav Pandit

B. Sc., Tribhuvan University, Nepal, 1993

M. Sc., Tribhuvan University, Nepal, 1996

Ph.D., Kent State University, 2012

Approved by

_____ Dr. Declan Keane, Professor, Physics
Chair, Doctoral Dissertation Committee

_____ Dr. Spyridon Margetis, Professor, Physics

_____ Dr. Bryon Anderson, Professor, Physics

_____ Dr. Antal I. Jakli, Professor, Liquid Crystal Institute

_____ Dr. Mark L. Lewis, Professor, Mathematics

Accepted by

_____ Dr. James T. Gleeson, Chair, Department of Physics

_____ Dr. Raymond A. Craig, Dean, College of Arts
and Sciences

Table of Contents

List of Figures

List of Tables

Acknowledgements

First of all, I would like to extend my heartfelt thanks to my advisor, Dr. Declan Keane, for his tremendous help ranging from overall guidance and constant encouragement of my Ph.D. research, to making sure my presentations went well. Declan is not only an advisor in physics but also a friend and a mentor in life. Thank you for the loving care for me and my family.

My sincere thanks to Dr. Wei-Ming Zhang for his guidance, especially in the beginning days, to make me familiar with C++ programming, root and with the STAR software environment. My gratitude also goes to Gang Wang, Paul Sorensen, Aihong Tang and Art Poskanzer, with whom I had stimulating discussions on numerous occasions, which helped me understand flow physics in heavy ion collisions. It was a wonderful experience working with them. Special thanks to Akio Ogawa for extensive support and guidance to help me understand the intricate details of the BBC detector both in hardware and software.

I would like to express my thanks to all the faculty members of the Physics Department and especially to Dr. James Gleeson for his counseling as my academic advisor. I would also like to extend my appreciation to all the office staff in the Physics Department: Cindy Miller, Loretta Hauser, Chris Kurtz, and Kim Birkner for their quick response and instant solutions for problems that I encountered.

I also owe many thanks to all the friends at BNL and Kent State who have contributed in one way or another towards my personal and/or academic progress.

I am deeply indebted to my family members for their support, encouragement, and love. I would like to thank my wife, Ambika Gyawali-Pandit, from the bottom of my heart for

her love and support, which has been a tremendous source of inspiration and strength for me. My sons Ayush and Erish deserve my special thanks for their understanding that their dad had some other important work to finish if he was not available when they needed him the most.

Thanks are also due to the RHIC Operations Group and RCF at BNL for their support, and to the members of the STAR collaboration.

Chapter 1

INTRODUCTION

1.1 Heavy Ion Collisions

A fundamental question of physics is what happens to nuclear matter as it is heated or compressed. Understanding the properties of matter under extreme conditions is crucial for learning about the equation of state that controlled the evolution of the early universe as well as the structure of compact stars [1]. High-energy heavy-ion collisions can experimentally probe very high energy density and temperature [2]. The Relativistic Heavy Ion Collider (RHIC) at Brookhaven National Laboratory has been in use for this purpose since 2000. It collides two beams of heavy ions (such as gold ions) after they are accelerated to relativistic speeds (close to the speed of light). The beams, with energy per nucleon up to 100 GeV, travel in opposite directions around a 2.4-mile two-lane racetrack. At six intersections, the beams cross, leading to collisions. The two ions approach each other like two disks, due to relativistic length contraction. Then they collide, smashing into and passing through one another, and the resulting hot volume called a "fireball" is created. Under these extreme conditions, we expect a transition from matter consisting of baryons and mesons, in which quarks are confined, to a state with liberated quarks and gluons. This new phase of matter is called the Quark Gluon Plasma [3].

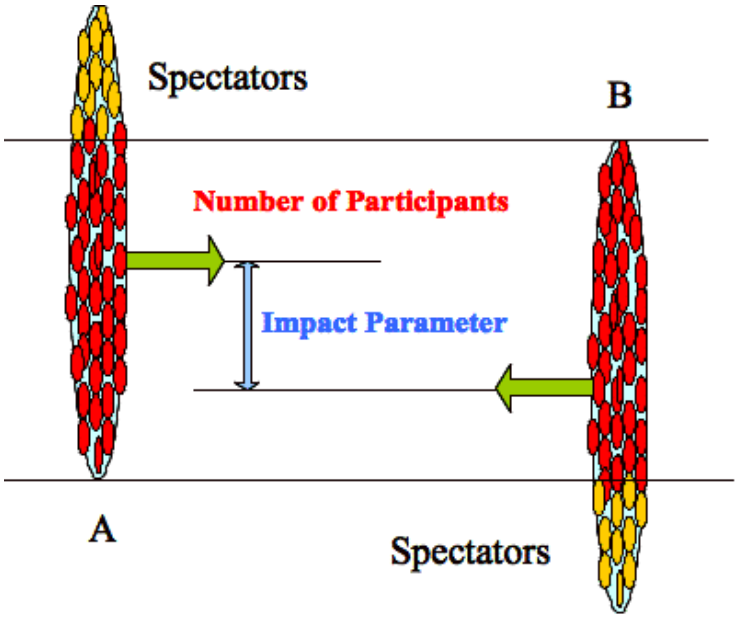

Figure 1.1: Collision of two nuclei A and B, with a non-zero impact parameter. The participants and the spectators are also shown. The nuclei have a spherical shape in their own rest frames, but are Lorentz-contracted when accelerated. At maximum RHIC energy, the contraction factor (about 100) is much greater than illustrated here.

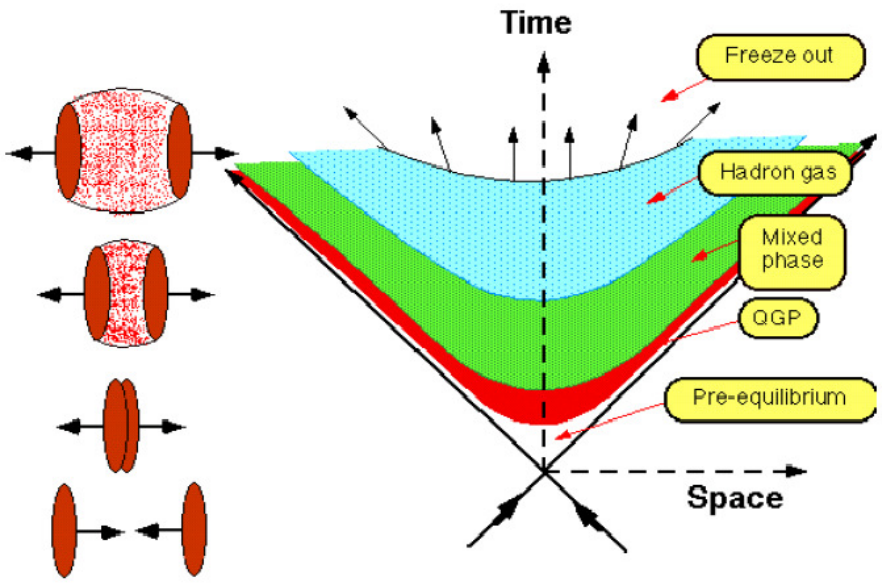

Figure 1.2: Space-time diagram and different evolution stages of a relativistic heavy-ion collision

1.2 Quark Gluon Plasma and the QCD Phase Diagram

Quantum chromodynamics (QCD) is the theory of the strong interaction, which describes the quarks and gluons found in hadrons. At high energy, the strong coupling constant becomes smaller, which results in the quarks and gluons interacting very weakly. A quark-gluon plasma (QGP) or quark soup is a phase of matter which exists at extremely high temperature and/or density with free quarks and gluons. Inside a hadron, when quarks become asymptotically close, they behave as non-interacting particles.

The QCD phase diagram includes two phase regions - the QGP phase, where the relevant degrees of freedom are quarks and gluons, and the hadronic phase. The results at top RHIC energies suggest that the QGP is created and that it is in local thermal equilibrium at a very early stage, because of its observed hydrodynamic expansion patterns [4]. Finite

temperature lattice QCD calculations [5, 6] at baryon chemical potential μ_B= 0 suggest a cross-over above a critical temperature T_c of 170 to 190 MeV from the hadronic to the QGP phase. At large μ_B, several QCD-based calculations [7] predict the quark-hadron phase transition to be of first order. In this scenario, the point in the QCD phase plane (T vs. μ_B) where the first-order phase transition has its end point corresponds to a critical point, and occurs at an intermediate value of the temperature and baryon chemical potential.

Exploring the QCD phase diagram is one of the important tasks in the study of heavy ion collisions. The search for the QCD critical point and the effort to locate the QCD phase boundary in the phase diagram has been of great interest to the high-energy heavy-ion theorists as well as experimentalists. Experimental collaborations that are at present focusing on these exciting physics issues are STAR (Solenoidal Tracker At RHIC) [8] and PHENIX (Pioneering High Energy Nuclear Interaction eXperiment) [9] at RHIC, and SHINE (SPS Heavy Ion and Neutrino Experiment) [10] at SPS (the Super Proton Synchrotron) at CERN in Switzerland. The near future experiments which aim to search for a possible critical point are CBM (Compressed Baryonic Matter) [11] at FAIR (Facility for Antiproton and Ion Research) at Darmstadt in Germany, and NICA (Nuclotron-based Ion Collider fAcility) at Dubna [12] in Russia. These will cover somewhat different regions of the phase diagram and hence are complementary to each other.

1.3 Beam Energy Scan at RHIC

The QCD phase diagram can be accessed by varying temperature T and baryonic chemical potential μ_B. Experimentally this can be achieved by systematically varying the colliding beam energy which provides an opportunity to probe the different regions of the QCD phase diagram. This may uncover evidence of a first-order phase transition and of the critical point associated with it. The search for the critical point and the onset of deconfinement

is a subject of the ongoing Beam Energy Scan (BES) [8] program being carried out by the STAR collaboration.

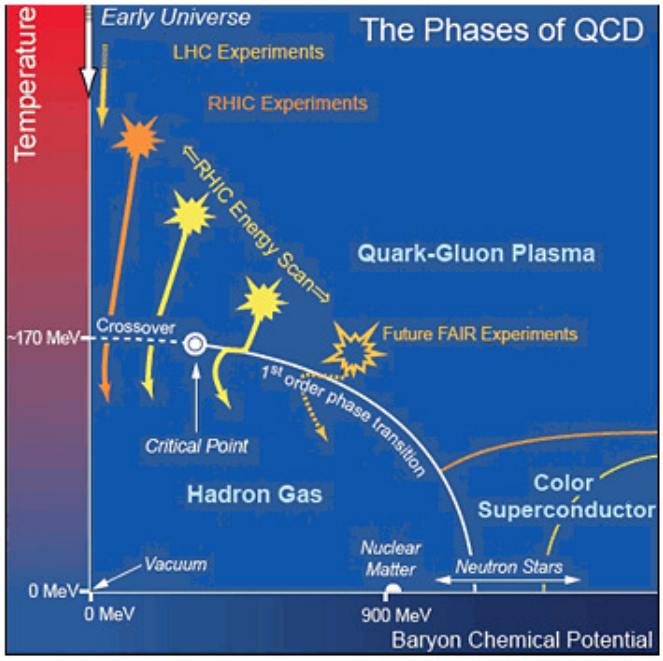

Figure 1.3: Schematic picture of QCD phase diagram shown in $T - \mu_B$ space

The region under study as part of the RHIC BES program is also indicated in the schematic phase diagram in Fig. 1.3. The STAR detector at RHIC has taken data at various beam energies in the past, such as at 19.6 GeV in the 2002 running period and at 22.4 GeV in 2004 running period. These test runs laid the ground work for the Beam Energy Scan Program at RHIC. As a first step of this program, a test run was conducted at RHIC in the year 2008 by colliding AuAu ions at $\sqrt{s}_{NN}$ = 9.2 GeV. The successful analyses of various observables and the beautiful results [13] demonstrated the readiness of the STAR experiment and hence the RHIC collider to perform the critical point search. The anisotropic

flow measurements from these test runs are also included in chapter 5 and chapter 6 of this dissertation.

The main part of the BES phase-one data taking happened successfully in 2010 (Run 10) and 2011(Run 11). STAR took data at $\sqrt{s}_{NN}$=7.7, 11.5 and 39 GeV in the year 2010 and at $\sqrt{s}_{NN}$ =19.6 and 27 GeV in the year 2011. The corresponding μ_B coverage of these energies is estimated to be $112 < \mu_B < 410$ MeV. Anisotropic flow analysis of these data is one of the main objectives of this dissertation.

1.4 Physics Observables for RHIC Energy Scan

The most important physics observables identified for the BES program are broadly classified into two groups [8]. The first group of observables is studied to search for "turn-off" of the QGP signatures already established at the top RHIC energies as we scan down in beam energy. The second group of observables has promise in the search for a first-order phase transition and for a critical point. Some selected observables are reviewed below.

1.4.1 QGP Signatures

It is generally recognized that there is no single unique signal which allows an unequivocal identification of quark-gluon plasma. Here we discuss some of the observables which may strengthen evidence for the presence of the de-confined phase.

Number of Constituent-Quark (NCQ) Scaling of v_2

The azimuthal distribution of particles with respect to the reaction plane allows a measurement of anisotropic flow and it is conveniently characterized by the Fourier coefficients [14]

$$v_n = \langle \cos n(\phi - \Psi_r) \rangle \tag{1.1}$$

where the angle brackets indicate an average over all the particles used, ϕ denotes the azimuthal angle of an outgoing particle, n denotes the Fourier harmonic, and Ψ_r is the azimuth of the reaction plane. The reaction plane is defined by the beam axis and the vector connecting the centers of the two colliding nuclei. Elliptic flow, v_2, is the second

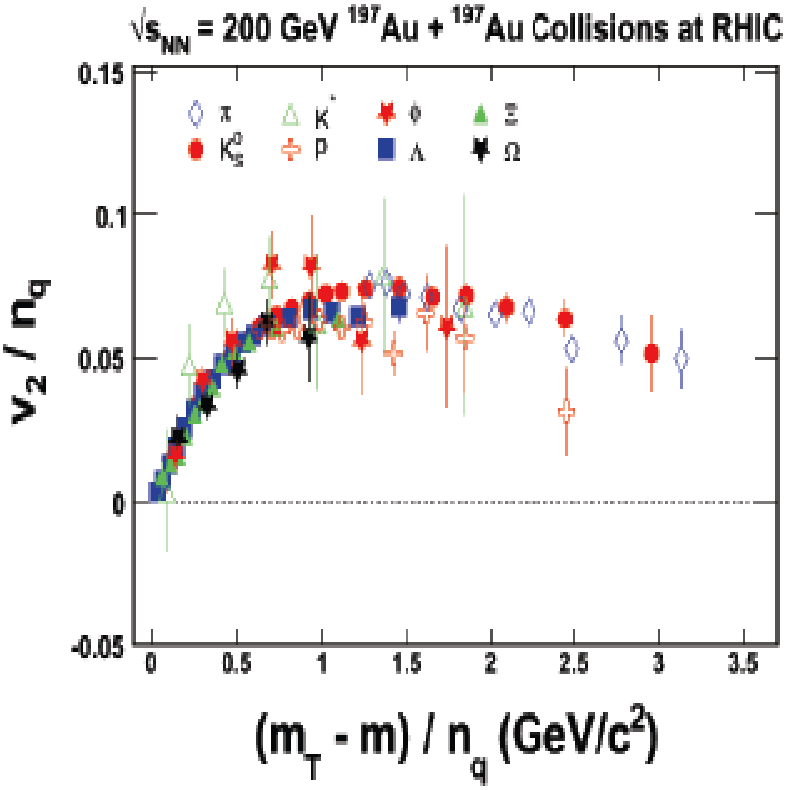

Figure 1.4: Identified particle v_2 as a function of $m_T - m$ scaled by number of constituent quarks at 200 GeV [15].

harmonic coefficient of the Fourier expansion. When elliptic flow v_2 is plotted versus transverse kinetic energy $(m_T - m)$, where $m_T = \sqrt{(}p_T^2 + m^2)$ with m being the mass of

the particle, v_2 for all identified particles below $m_T - m$ = 0.9 GeV/c^2 falls on a universal curve. Above that, meson and baryon v_2 deviates, with baryon v_2 rising above meson v_2 and saturating at a value approximately 50 % larger than for mesons; however, upon dividing each axis by the number of constituent quarks (n_q = 2 for mesons and 3 for baryons), the meson and baryon curves merge very impressively into a single curve over a wide range of $m_T - m$. This well-known scaling behavior is one of the most striking pieces of evidence for the existence of partonic degrees of freedom during the AuAu collision process at 62.4 and 200 GeV [15]. An observation of this NCQ scaling behavior turning off below some threshold beam energy would be a very powerful confirmation of our current understanding of the de-confined phase. Elliptic flow will be discussed in detail in the second chapter.

High and Intermediate p_T Spectra

High transverse momentum (p_T) particles, emerging from hard scatterings, encounter energy loss and angular deflection while traversing and interacting with the medium produced in heavy-ion collisions. The stopping power of a QGP is predicted to be higher than that of hadronic matter, and this results in jet quenching — a suppressions of high p_T hadron yield relative to the expectation from p+p collisions scaled by the number of elementary nucleon-nucleon interaction [16].

$$R_{AA}(p_T) = \frac{d^2N_{AA}/dp_T dy}{T_{AA} d^2\sigma_{pp}/dp_T dy} \tag{1.2}$$

where $T_{AA} = \langle N_{\rm bin}\rangle/\sigma_{pp}^{\rm inel}$ is the nucleus overlap function calculated from a Glauber model [17].

Instead of normalizing the AA spectra with respect to reference pp spectra (which are not always available), an alternative ratio involves normalizing instead by spectra measured

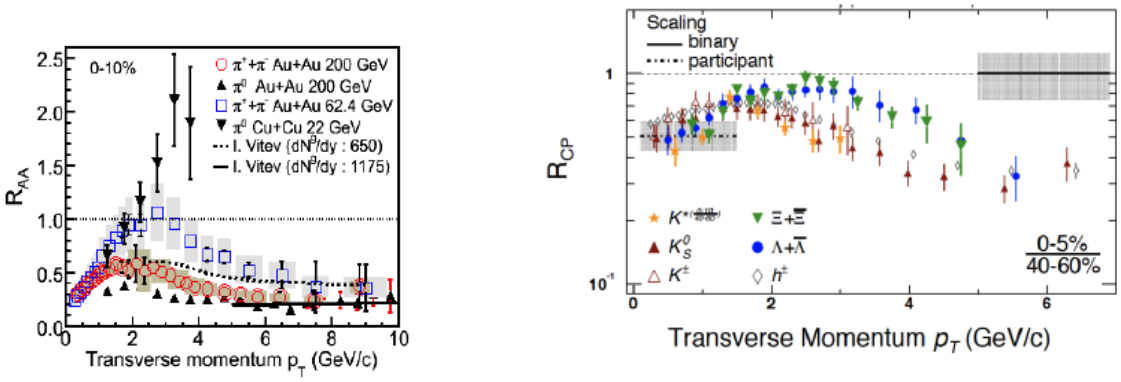

.

Figure 1.5: Left panel: Nuclear Modification Factor R_{AA} as a function of transverse momentum. Right panel: R_{CP} as a function of transverse momentum. Both plots are from Ref. [8]

in peripheral collisions:

$$R_{CP}(p_T) = \frac{(d^2N_{AA}/dp_T d\eta)_{[\text{central}]}/N_{\text{coll}}}{(d^2N_{AA}/dp_T d\eta)_{[\text{peripheral}]}/N_{\text{coll}}}. \tag{1.3}$$

In 200 and 62.4 GeV AuAu collisions, the high p_T hadrons are strongly suppressed indicating that the strong jet quenching seen at top RHIC energies may set in somewhere below 62.4 GeV. The particle type dependence of the nuclear modification factor R_{AA} shows a dependence on constituent quark number rather than mass, indicating that baryon yields increase faster with the matter density than meson yields. The energy dependence of the baryon to meson ratio is a particularly stringent test of models such as the recombination and coalescence models that rely on the interplay between a falling p_T spectrum and recombination or flow to describe the baryon enhancement [8, 16].

Two particle $\Delta\eta$ and $\Delta\phi$ correlations

Two-particle correlation studies in $\Delta\phi$ and $\Delta\eta$ at top RHIC energy reveal a correlation structure strongly elongated in $\Delta\eta$ at small $\Delta\phi$ as shown in Fig. 1.6. This structure is

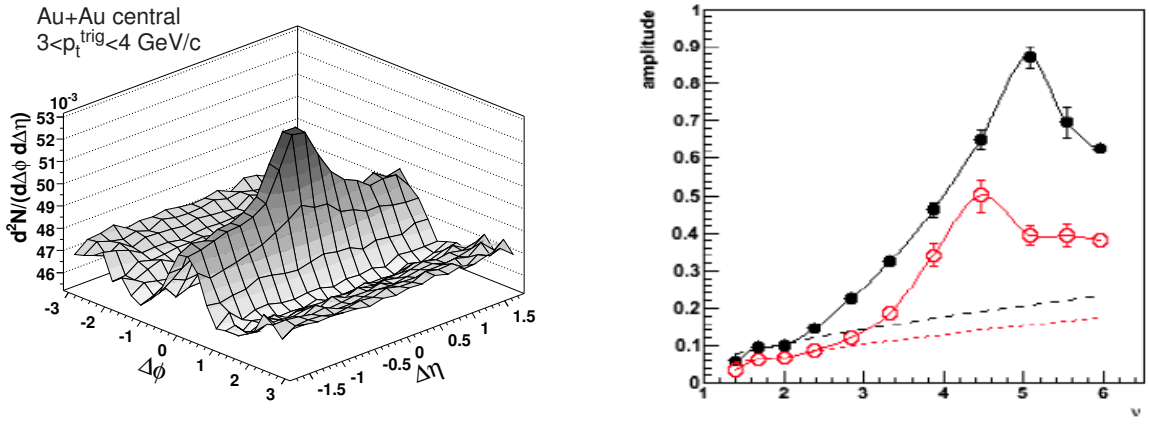

Figure 1.6: Two-particle correlation on $\Delta\eta$ and $\Delta\phi$ of a central event in 200 GeV AuAu collisions [18] showing the ridge in the left panel and the ridge amplitude as a function of centrality on the right.

known as the ridge. The amplitude of this ridge-like correlation rises rapidly, reaches a maximum, and then falls in the most central collisions.

Models based on Glasma flux tubes and Mach cones [19] tried to explain this ridge phenomenon with a partial success. Recently, it has been argued that the ridge is a natural outcome of the higher flow harmonics [20, 21], especially the third harmonic popularly known as "Triangular Flow". Analysis of triangular flow (v_3) is one of the main topics of this dissertation.

Local Parity Violation in Strong Interactions

In non-central heavy ion collisions, a large orbital angular momentum vector (L) exists normal (90°) to the reaction plane, leading to a very intense localized magnetic field (due to the net charge of the system). If the system is deconfined, there can be strong parity violating domains, and different numbers of left- and right-hand quarks, leading to preferential emission of like-sign charged particles along L. In the azimuthally anisotropic emission of

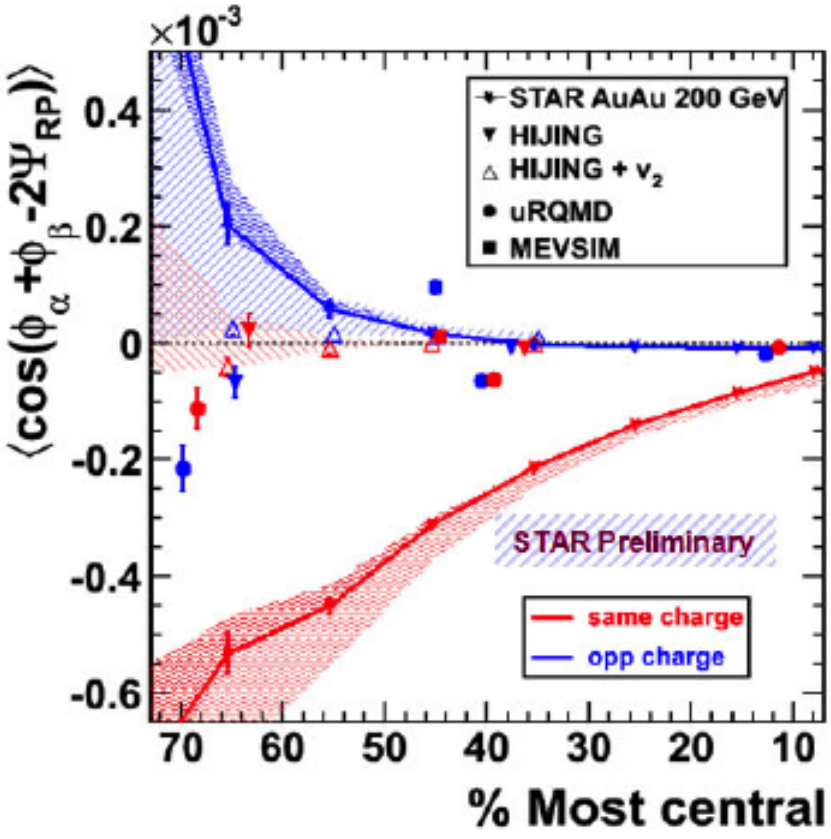

Figure 1.7: Signal associated with local parity violation (LPV) at 200 GeV [22]

particles,

$$\frac{dN_{\pm}}{d\phi} \propto 1 + 2a_{\pm}\sin(\phi - \Psi_r) + ... \tag{1.4}$$

the coefficient a represents the size of the local parity violating (LPV) signal, and the remaining terms (not shown explicitly) are the familiar ones with coefficients v_n for directed and elliptic flow, etc. However, the coefficient a averages to zero when integrated over many parity violating domains in many events. The STAR collaboration has measured this signal using a parity-even two-particle correlator, $\langle\cos(\phi_\alpha + \phi_\beta - 2\Psi_R)\rangle$ proposed by Voloshin [23] for like sign (LS) and of unlike-sign (US) particle pairs, where ϕ_α and ϕ_β are the azimuthal angles of the two particles and Ψ_R is the reaction plane azimuth. The observed results are consistent with the expected signal for parity violation, especially the centrality dependence, as seen in Fig. 1.7. LPV is an emerging and important RHIC discovery in its own right and is generally believed to require deconfinement, and thus also is expected to turn-off at lower energies.

1.4.2 Signatures of a Phase Transition and a Critical Point

Similar to the signatures of quark-gluon plasma, it is difficult to single-out one particular signature for a critical point or a first-order phase transition. The following physics observables are considered to be the most promising indicators for a first-order phase transition or a critical point.

Directed Flow

Directed flow, v_1, is the first harmonic coefficient of the Fourier expansion of the final-state momentum-space azimuthal anisotropy, and it reflects the collective sidewards motion of the particles in the final state. Both hydrodynamic and nuclear transport models indicate that directed flow is a promising observable for investigating a possible phase transition,

especially in the region of relatively low beam energy in the BES range [8]. In particular, the shape of v_1 as a function of rapidity, y, in the midrapidity ($|y| < 1.0$) region is of interest because it has been argued that it offers sensitivity to crucial details of the expansion of the participant matter during the early stages of the collision [24]. I discuss this in detail in the second chapter.

Fluctuation Measures

Fluctuations are well known phenomena in the context of phase transitions. In particular, second-order phase transitions are accompanied by fluctuations of the order parameter at all length scales, leading to phenomena such as critical opalescence [25]. Dynamical fluctuations in global conserved quantities such as baryon number, strangeness or charge may be observed near a QCD critical point. The characteristic signature of the existence of a critical point is an increase, and divergence, of fluctuations [26].

Particle Ratio Fluctuations Particle ratios, e.g. K/π and p/π, probe medium dynamics at chemical freeze out. They are also convenient to study because volume effects are canceled. The beam energy and centrality dependences of the dynamical fluctuations of the particle ratio may be sensitive to a critical point or a phase transition [27].

Mean p_T Fluctuations Average transverse momentum fluctuations are discussed in the literature in the context of a search for the QCD critical point. It is expected that close to the critical point, long-range correlations are very strong, resulting in enhanced momentum fluctuations, especially for small momenta. Small p_T values are important because correlation length r diverges at the Critical Point and $\Delta r \Delta p \sim \hbar/2$. In addition to the transverse momentum fluctuations for all charged particles, one can investigate p_T fluctuations of the negative and positive charges independently, as well as the cross correlations between them.

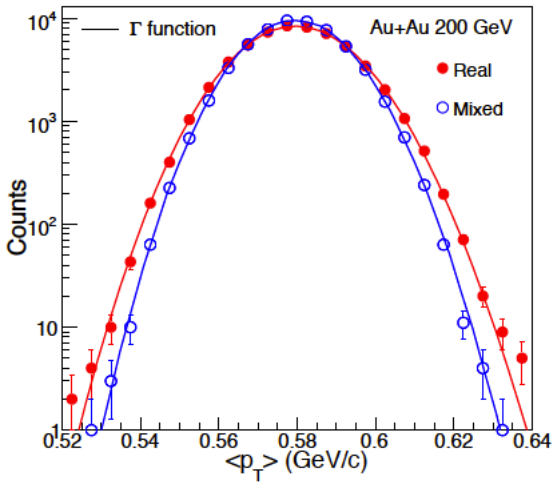

Figure 1.8: Event-wise mean p_T distribution for the most central AuAu collisions at 200 GeV, measured in the STAR experiment [28]

Fig 1.8 shows the event-wise mean p_T distribution in 200 GeV AuAu collisions [28].

Higher Moments and Kurtosis

Due to their high sensitivity to the correlation length and their direct connection to the thermodynamic susceptibilities, higher moments (Skewness (S), Kurtosis (κ) etc.) of conserved quantities, such as net-baryons, net-charge and net-strangeness have been extensively studied to search for the QCD critical point and to probe the bulk properties. It is expected that the evolution of fluctuations from the critical point to the freeze-out point may lead to a non-Gaussian shape in the event-by-event multiplicity distributions [29]. The measurement of higher moments of event-by-event identified-particle multiplicity distributions will provide a direct connection between experimental observables and Lattice Gauge Theory calculations.

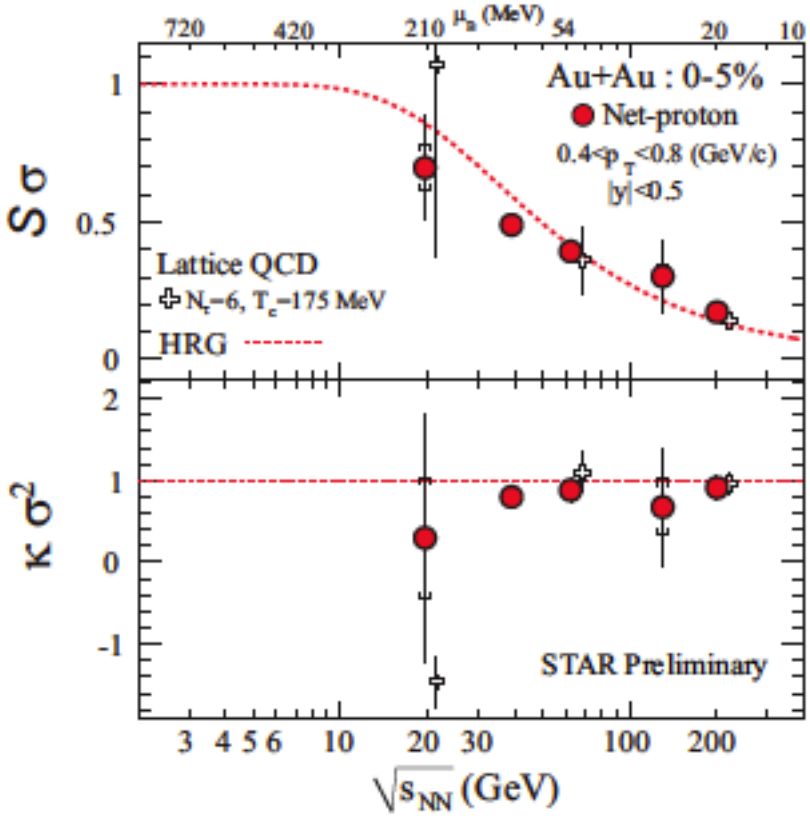

Figure 1.9: Energy dependence of moment products $\kappa\sigma^2$ and $S\sigma$ of net-proton distributions for (0-5%) central AuAu collisions a function of beam energy [30].

Azimuthally-Sensitive Femtoscopy

The probability of detecting two bosons at small relative momentum is affected by quantum mechanical interference between their wave functions. The interference effect depends on the space-time extent of the boson-emitting source. This effect is commonly known as the Hanbury-Brown Twiss (HBT) effect [31]. One of the main observables that is believed to be sensitive to the Equation of State is the freeze-out shape of the participant zone in non-central collisions. In heavy-ion collisions, HBT measurements of particles emitted from the colliding system yield the longitudinal and transverse radii as well as the lifetime of the emitting source at the moment of thermal freeze-out. Azimuthally-sensitive femtoscopy adds to the standard HBT observables by allowing the tilt angle of the ellipsoid-like particle source in coordinate space to be measured. These measurements hold promise for identifying a softest point, and they complement the momentum-space information revealed by flow measurements. HBT radii measured relative to the event plane are the coordinate space analogs of directed and elliptic flow, and are expected to be sensitive to a softening in the EOS related to a possible first-order phase transition. The spatial anisotropy probed by HBT is weighted in the time evolution and may retain sensitivity to the softest point.

1.5 Outline of Current Work

This dissertation is divided into nine chapters. Chapter 2 describes the theory and applications of anisotropic flow. This chapter also describes some recent experiments similar to the work reported in this dissertation. Chapter 3 gives a brief description of the STAR experiment. It describes the various detector subsystems. Chapter 4 describes the analysis method, with particular emphasis on estimation of the reaction plane based on signals in the

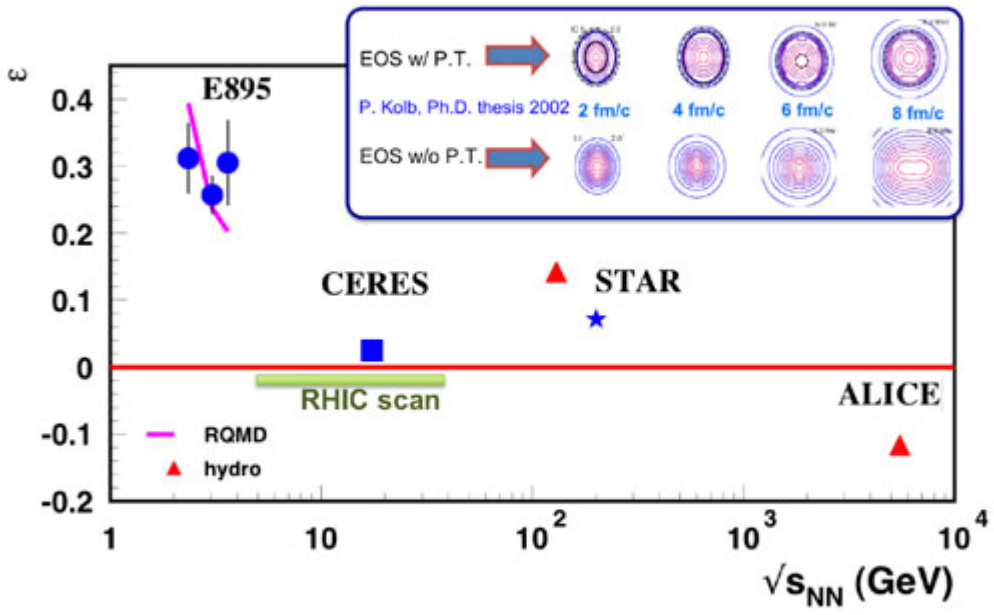

Figure 1.10: The transverse spatial freeze out anisotropy ε as a function of collision energy, for midcentral (10-30%) heavy ion collisions [32].

Beam Beam Counters (BBC) of the STAR experiment. Use of the BBC for anisotropic flow measurements is one of the main unique aspects of this PhD project. Chapter 5 presents the results of directed flow analysis. Chapter 6 presents the results of elliptic flow analysis. Chapter 7 presents the results of triangular flow analysis and chapter 8 presents the results of dipole asymmetry measurements. Chapter 9 is devoted to a summary and conclusions.

Chapter 2

ANISOTROPIC FLOW

2.1 Introduction

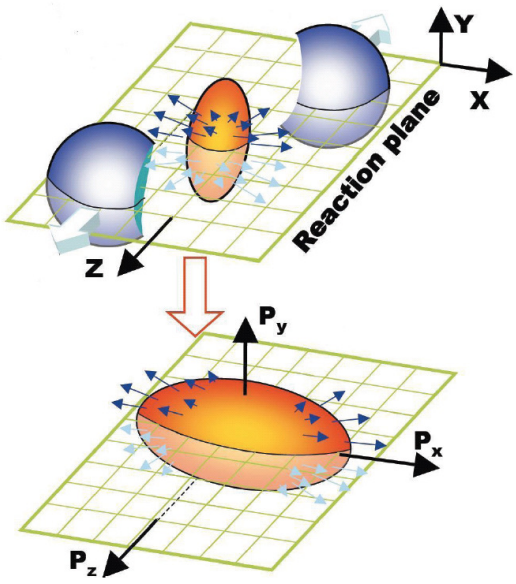

Figure 2.1: Event anisotropy in spatial and momentum space with respect to the reaction plane.

In a non-central relativistic heavy ion collision, the overlap region of the two nuclei in the transverse plane has a short axis, which is parallel to the vector connecting the center of two nuclei, and a long axis perpendicular to it. By convention, this long axis defines the y direction. The incident beam direction defines the z axis. The $x - z$ plane is called the reaction plane. The particles which are along the short axis are subject to more pressure gradient than the particles along the long axis. As a result, anisotropy is developed in the

final state in momentum space. Anisotropic flow measurements refer to this momentum anisotropy and they reflect the time-evolution of the pressure gradient generated in the system at very early times. Flow provides indirect access to the EOS of the hot and dense matter formed in the reaction zone, and helps us to understand processes such as thermalization, creation of QGP, phase transitions, etc. It is one of the important measurements in relativistic heavy-ion collisions and has attracted attention from both theoreticians and experimentalists [14].

Anisotropic flow is conveniently quantified by the Fourier coefficients of the particle distribution, written as

$$E\frac{d^3N}{d^3p} = \frac{1}{2\pi}\frac{d^2N}{p_T dp_T dy}(1 + \sum_{n=1}^{\infty} 2v_n \cos n\phi). \tag{2.1}$$

where p_T is the transverse momentum, y is rapidity and ϕ is the angle between each particle and the true reaction plane angle, ψ_R, defined by the $x - z$ plane. The sine terms in the Fourier expansion vanish due to reflection symmetry with respect to the reaction plane. It follows that $\langle \cos n\phi \rangle$ gives v_n, as shown below.

$$\langle \cos n\phi \rangle = \frac{\int_{-\pi}^{\pi} \cos n\phi \quad E\frac{d^3N}{d^3p} d\phi}{\int E\frac{d^3N}{d^3p} d\phi} \tag{2.2}$$

Substitution from Eq. (2.1) above,

$$\langle \cos n\phi \rangle = \frac{\int_{-\pi}^{\pi} \cos n\phi \; (1 + \sum_{n=1}^{\infty} 2v_n \cos n\phi) d\phi}{\int (1 + \sum_{n=1}^{\infty} 2v_n \cos n\phi) d\phi} \tag{2.3}$$

Now using the orthogonality relation between Fourier coefficients, $\int \cos n\phi \cos m\phi \, d\phi = \delta_{mn}$ we obtain

$$v_n = \langle \cos n\phi \rangle. \tag{2.4}$$

The first three flow components i. e, n = 1, 2 and 3 are called directed flow, elliptic flow and triangular flow respectively.

2.2 Flow Components

The term directed flow (also called sideward flow) comes from the fact that such a flow looks like a sideward bounce of the fragments away from each other in the reaction plane, and the term elliptic flow is inspired by the fact that the azimuthal distribution with a non-zero second harmonic deviates from isotropic emission in the same way that an ellipse deviates from a circle. Triangular flow gets its name from a triangular anisotropy in initial geometry due to fluctuations.

2.2.1 Directed Flow

Directed flow in heavy-ion collisions is quantified by the first harmonic (v_1) in the Fourier expansion of the azimuthal distribution of produced particles with respect to the reaction plane [14]. It describes collective sideward motion of produced particles and nuclear fragments and carries information on the very early stages of the collision. The shape of $v_1(y)$ in the central rapidity region is of special interest because it might reveal a signature of a possible Quark-Gluon Plasma (QGP) phase.

At AGS and lower beam energies, v_1 versus rapidity is an almost linear function of rapidity. Often, just the slope of $v_1(y)$ at midrapidity is used to define the strength of directed flow. The sign of v_1 is by convention defined as positive for nucleons in the projectile fragmentation region [33]. At AGS and lower beam energies, the slope of $v_1(y)$ at midrapidity is observed to be positive for protons, and significantly smaller in magnitude and negative

for pions. The opposite directed flow of pions is usually explained in terms of shadowing by nucleons [34]. At 62.4 and 200 GeV, directed flow is smaller near midrapidity, with a weaker dependence on rapidity. At these high energies, we observe that the slope of v_1 at midrapidity is negative for nucleons as predicted by models, but pions also have a negative slope [35]. In one-fluid hydrodynamical calculations, the wiggle structure, i.e., the negative slope for nucleons, appears only under the assumption of a QGP equation of state, thus becoming a signature of the QGP phase transition. Then the wiggle structure is interpreted to be a consequence of the expansion of the highly compressed, disk-shaped system, with the plane of the disk initially tilted with respect to the beam direction [36]. The subsequent system expansion leads to the so-called anti-flow or third flow component [38]. Such flow can reverse the normal pattern of sideward deflection as seen at lower energies, and hence can result in either a flatness of v_1, or a wiggle structure if the expansion is strong enough. A similar wiggle structure in nucleon $v_1(y)$ is predicted if one assumes strong but incomplete baryon stopping together with strong space-momentum correlations caused by transverse radial expansion [37].

At energies covered by the RHIC beam energy scan program, the beam rapidity region lies within STAR detector coverage, and Beam Beam Counters are utilized to reconstruct the first order event plane. The large pseudorapidity gap between east and west BBC and between BBC and TPC helps us to minimize the azimuthal correlations not related to reaction plane orientation, the so-called non-flow effects. Furthermore particle identification is greatly enhanced by the addition of the TOF detector [39], which began operation in 2010. Identified-particle directed flow, especially for protons and pions, provides new insights.

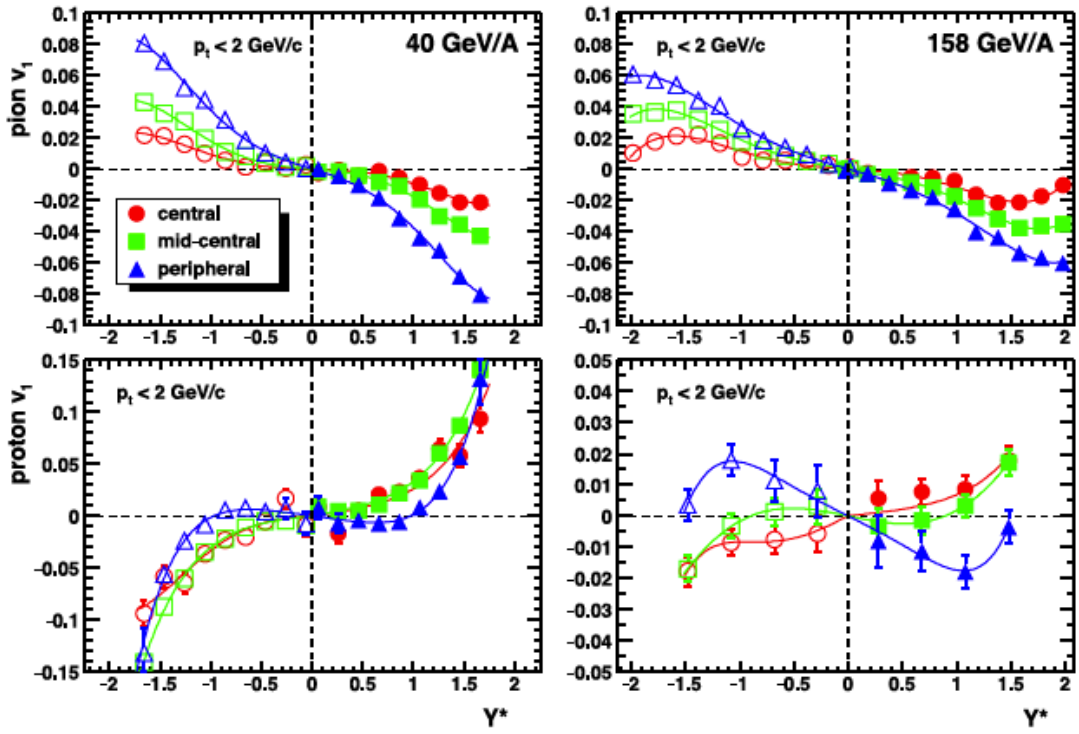

Figure 2.2: Directed flow of pions and protons as a function of rapidity at $40A$ GeV and $158A$ GeV, as reported by the NA49 Collaboration [40].

2.2.2 Elliptic Flow

Elliptic flow is caused by the initial geometric deformation of the reaction region in the transverse plane. At top RHIC energies, elliptic flow tends to preferentially enhance momenta along the direction of the smallest spatial extent of the source, and thus the in-plane (positive) component of elliptic flow dominates. In general, large values of elliptic flow are considered signatures of hydrodynamic behavior, while smaller signals can have alternative explanations. The centrality dependence of elliptic flow is of special interest. In the low density limit (LDL), the mean free path is comparable to, or larger than, the system size, and the colliding nuclei resemble dilute gases. The final anisotropy in momentum space depends not only on the initial spatial eccentricity ϵ (defined below in Eq. 2.6), but also on the particle density, which affects the number of rescatterings. In this limit, the final elliptic flow is as below; a more detailed formula in given in Ref. [41].

$$v_2 \propto \frac{\epsilon}{S}\frac{dN}{dy} \tag{2.5}$$

where dN/dy characterizes density in the longitudinal direction and $S = \pi R_x R_y$ is the initial transverse area of the overlapping zone, with $R_x^2 \equiv \langle x^2 \rangle$ and $R_x^2 \equiv \langle y^2 \rangle$ describing the initial geometry of the system in the x and y directions, respectively. Note that the $x - z$ axes determine the reaction plane. The averages above include a weighting with the number of collisions along the beam axis in a wounded nucleon [42] calculation. The spatial eccentricity, also called standard eccentricity, is defined as

$$\varepsilon = \frac{R_y^2 - R_x^2}{R_x^2 + R_y^2}, \tag{2.6}$$

and for hard spheres is proportional to the impact parameter over a wide range of that variable.

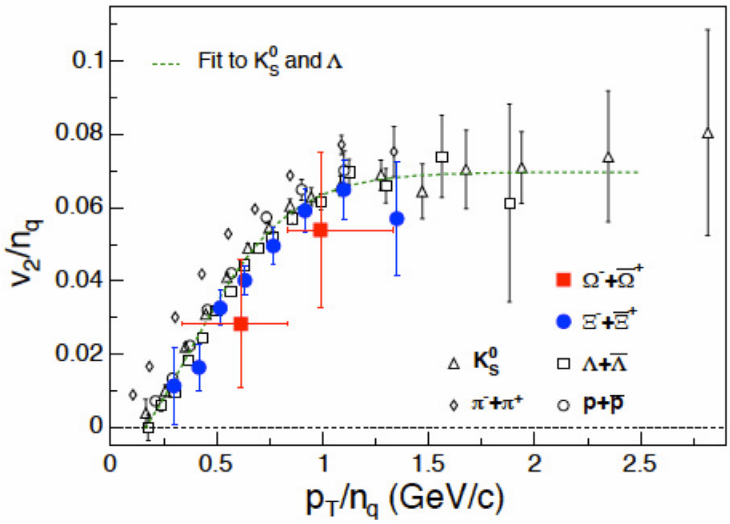

Figure 2.3: v_2 per number of constituent quarks n_q as a function of p_T/n_q for various particle species from 200 GeV Au+Au minimum bias collisions. The plot is from [15].

Because of the event-by-event fluctuations in the participant nucleon position, the eccentricity driving elliptic flow in a given event is that defined by the principal axes (x', y') of the distribution of participant nucleons. This participant eccentricity $\epsilon_{\rm part}$ can be written as

$$\varepsilon_{\rm part} = \frac{\sqrt{(\sigma_y^2 - \sigma_x^2)^2 + 4\sigma_{xy}^2}}{\sigma_x^2 + \sigma_y^2}, \tag{2.7}$$

where

$$\sigma_x^2 = \{x^2\} - \{x\}^2,\ \sigma_y^2 = \{y^2\} - \{y\}^2, \tag{2.8}$$

$$\sigma_{xy} = \{xy\} - \{x\}\{y\}, \tag{2.9}$$

As follows from the argument above, the elliptic flow increases with particle density. Eventually, it saturates at the hydro limit. In a hydrodynamic picture, where the mean free path is much less than the geometrical size of the system, the ratio of v_2 to ε is expected to be approximately constant. The differential momentum anisotropy $v_2(p_T)$ is also of interest, especially for different hadron species. Fig. 2.3 shows v_2 per number of constituent quarks (n_q) as a function of p_T/n_q for various particle species. All hadrons, except pions, lie on the same curve within statistics, and there are plausible reasons to expect the pions to deviate. This universal scaling behavior lends strong support to the finding that collectivity is developed in the partonic stage at RHIC [15].

2.2.3 Dipole Asymmetry and Triangular Flow

Recent developments in understanding the initial geometry in heavy-ion collisions points to a "lumpy" initial state. Event-by-event fluctuations in the initial geometry lead to dipole asymmetry and triangular anisotropy in azimuthal particle production through the collective expansion of the medium [20, 43].

The dipole asymmetry can be quantified as

$$\epsilon_1 e^{i\Phi_1} = -\frac{\langle r^3 e^{i\phi}\rangle}{\langle r^3\rangle} \tag{2.10}$$

where ϵ_1 is dipole anisotropy in the initial position, Φ_1 is the steepest direction in the density distribution, and (r, ϕ) represent the position and azimuthal angle in a polar coordinate system. Various models based on ideal as well as viscous hydrodynamics or nuclear transport theory have been used to explain and predict these new flow harmonics and their correlations with each other. On the experimental side, this area has been gaining interest, and efforts to measure these observables is in progress. Recently Luzum *et al.* [44] have proposed a modified event plane method to study this observable, which suppresses the conventional directed flow and corrects for the effect of momentum conservation.

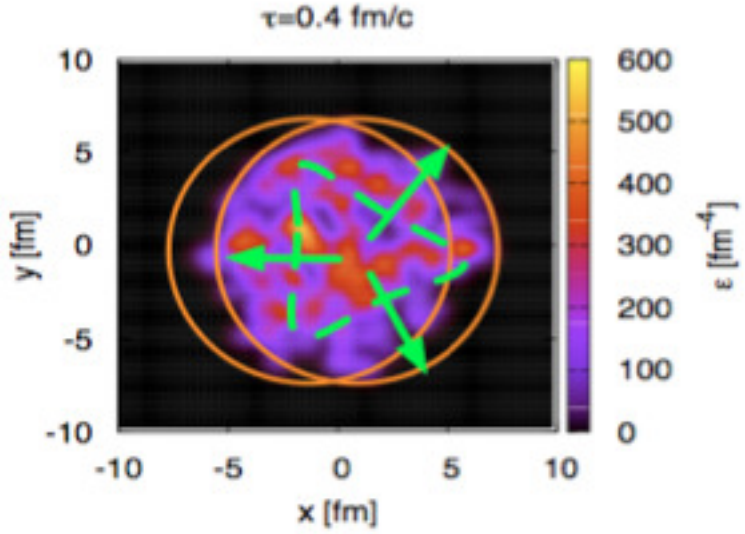

Figure 2.4: Energy density distribution in the transverse plane for one event, showing triangular anisotropy in the initial geometry. This plot is taken from Ref. [45].

Triangular anisotropy can be quantified as

$$\epsilon_{3,\mathrm{part}} = \frac{\sqrt{(\langle r^2 \cos 3\phi_{\mathrm{part}}\rangle^2 + \langle r^2 \sin 3\phi_{\mathrm{part}}\rangle^2)}}{\langle r^2 \rangle} \tag{2.11}$$

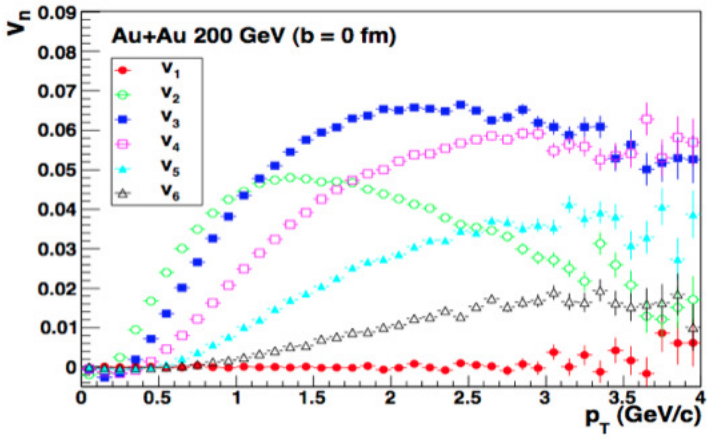

Figure 2.5: Flow harmonic coefficients for $n = 1, 2, 3, 4, 5$ as a function of p_T in 200 GeV AuAu collisions at zero impact parameter from a nuclear transport model. The plot is from Ref. [46].

The experimental measurement of these coefficients, i.e., dipole asymmetry and triangular flow, could provide some insight into the initial state geometry fluctuations.

2.3 Flow Fluctuations

Until recently, it was assumed that the event plane azimuth Ψ_n is completely uniform and symmetric with respect to the impact parameter for the third and higher-order odd flow harmonics. This assumption was based on the known symmetry when identical spherical nuclei collide. Now it is realized that event-by-event fluctuations break this symmetry [20,21,43] and these event-by-event fluctuations lead to dipole asymmetry, triangularity, and higher-order anisotropy arising from the initial geometry. Flow harmonics associated with these initial geometry fluctuations carry valuable information about the initial state

of the colliding systems and about the hydrodynamic evolution of the fireball created in the collision. In the Monte Carlo Glauber (MCG) model, the geometric fluctuations of the positions of nucleons lead to fluctuations of the participant plane from one event to another, which translates into flow fluctuations for the final-state particles [17]. It has been known for several years that flow fluctuations are important, but initially only the effect on elliptic flow v_2 was studied [47]. Measurement of flow fluctuations with odd harmonics provides important clues to understanding the expansion dynamics of the produced fireball and to quantify the medium properties. Simultaneous knowledge of multiple flow harmonics from the same system help to constrain the initial parameters [48] in various models describing heavy-ion collisions. This dissertation reports the first measurement of triangular flow and the flow harmonic associated with dipole asymmetry from the STAR experiment.

2.4 Non Flow Correlations

Two-particle azimuthal correlations not related to initial geometry or to the reaction plane are called non-flow [49]. These intrinsic correlations may come from short-range correlations like Bose-Einstein effects, resonance decays, and Coulomb interactions, or from jet or minijet correlations. In this study, we focus on discoveries related to initial geometry and the reaction plane, and therefore non-flow is an unwanted background effect that can obscure the desired signal. Non-flow effects are difficult to remove from the analysis, and can lead us astray from the true interpretation of anisotropic flow [49]. Non-flow limits the precise extraction of the viscosity to entropy density ratio η/s from data-model comparisons. Isolation of flow and non-flow is critical to the interpretation of the Fourier decomposition of fluid-like correlations.

Short-range non-flow correlations can be highly suppressed using an event plane reconstructed in a detector with a large pseudorapidity gap between the event plane and the

particles correlated with it. To reduce the sensitivity of our analysis to non-flow effects, we aim to reconstruct the reaction plane from the charged particles detected by the Beam Beam Counters (BBC). The large gap of more than two units in pseudorapidity between the TPC where flow is measured, and the BBC where the event plane is reconstructed, suppresses most of the non-flow correlations.

2.5 Model Calculations

2.5.1 RQMD

RQMD (Relativistic Quantum Molecular Dynamics) [50] is a semiclassical microscopic transport model, that combines classical propagation with stochastic interactions. In RQMD, strings and resonances are excited in elementary collisions of nucleons, and overlapping strings may fuse into "color ropes". Subsequently, the fragmentation products from ropes, strings, and resonance decays interact with each other and the original nucleons, mostly via binary collisions. These interactions drive the system towards equilibration and are responsible for the collective flow development, even in the pre-equilibrium stage. The RQMD code contains an option to vary the pressure in the high-density stage. In the medium, baryons may acquire effective masses, generated by introducing Lorentz-invariant quasipotentials into the mass-shell constraints, which simulate the effect of "mean fields". There are no potential-type interactions in the so-called cascade mode of RQMD, where the equilibrium pressure is simply that of an ideal gas of hadrons and resonances. Its equation of state is very similar to the one calculated in Ref. [51], because the spectrum of included resonance states is nearly the same.

While the predictions for baryon directed flow are unambiguous in both hydrodynamical and transport models, the situation for pion directed flow is less clear. RQMD model

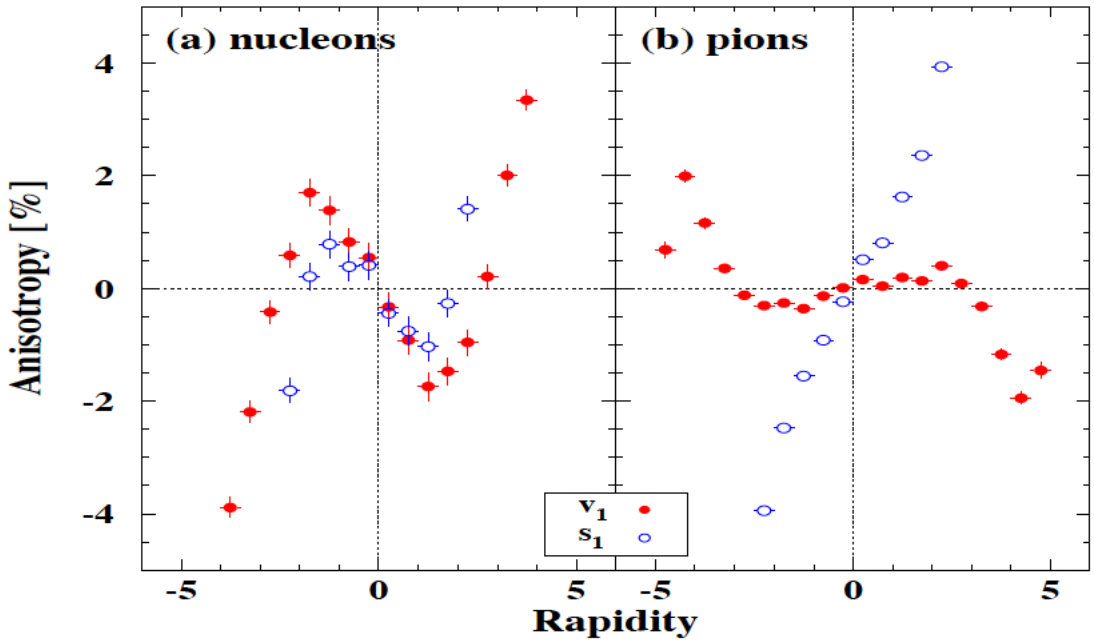

Figure 2.6: RQMD calculation of v_1 (filled circles) and s_1 which represents the initial coordinate-state anisotropy (open circles) for nucleons (left panel) and pions (right panel) in 200 GeV Au+Au collisions [37].

calculations for AuAu collisions at $\sqrt{s_{NN}}$ = 200 GeV indicate that shadowing by protons causes the pions to flow mostly with opposite sign to the protons, but somewhat diffused due to higher thermal velocities for pions.

RQMD is a microscopic nuclear transport model and does not assume formation of a QGP. In the simulation shown in Fig. 2.6, the "wiggle" is caused by a combination of space-momentum correlations characteristic of radial expansion, together with the correlation between the position of a nucleon in the nucleus and how much rapidity shift it experiences during the collision [37]. The wiggle predicted by this mechanism appears in peripheral or mid-peripheral collisions. An investigation of possible wiggle structures at RHIC is among the important goals of this dissertation.

2.5.2 UrQMD

UrQMD (Ultra-relativistic Quantum Molecular Dynamics) [52] is another relativistic hadronic transport model describing the phenomenology of nuclear collisions, and grew out of an effort to improve RQMD and adapt it for higher beam energies. The collision term is roughly the same as that of RQMD, though some implementation details are improved. For example, UrQMD handles more types of particles, and employs more detailed cross sections parametrized according to experimental data. In the early versions of UrQMD, hard processes are not included.

2.5.3 AMPT

The AMPT model (A Multi-Phase Transport model) [53] is a hybrid model. In the initial stage, it uses minijet partons from hard processes, and strings from soft processes, in the heavy ion jet interaction generator (HIJING). The time evolution of the resulting minijet partons is then described by Zhang's Parton Cascade (ZPC) model. After minijet

partons stop interacting, they are combined with their parent strings, as in the HIJING model with jet quenching, to fragment into hadrons using the Lund string fragmentation model as implemented in the PYTHIA program. The final-state hadronic scatterings are then modeled by ART (A Relativistic Transport model). The AMPT model has a "string melting" option to convert the initial excited strings into partons. Interactions among these partons are again described by the ZPC parton cascade model. Since there are no inelastic scatterings, only quarks and antiquarks from the melted strings are present in the partonic matter. The transition from partonic matter to hadronic matter is achieved using a simple coalescence model, where adjacent quark-antiquark pairs are combined into mesons and likewise, adjacent quark/antiquark triplets with appropriate invariant masses are combined into baryons/antibaryons.

Chapter 3

EXPERIMENTAL DETAILS

3.1 The Relativistic Heavy Ion Collider

The Relativistic Heavy Ion Collider (RHIC) at Brookhaven National Laboratory (BNL) is a world-class scientific research facility that began operation in 2000, following 10 years of development and construction. The Relativistic Heavy Ion Collider complex is actually composed of several accelerator facilities "chained" together to provide beams which are collided in detectors located around the RHIC ring.

Figure 3.1: Aerial view of the Relativistic Heavy Ion Collider (RHIC) complex at Brookhaven National Laboratory.

Heavy ions begin their travels in the Tandem Van de Graaff accelerator labeled 1 in Fig. 3.2. The ions then travel through a transfer line (2a) to the small, circular Booster (3)

where, with each pass, they are accelerated to higher energy. From the Booster, ions travel to the Alternating Gradient Synchrotron (4), where they are accelerated further. The AGS then injects the beams via another beamline (5) into the two rings of RHIC (6). In RHIC, the beams receive a final acceleration. Once they have reached their final energy, the ions can "orbit" inside the rings for hours.

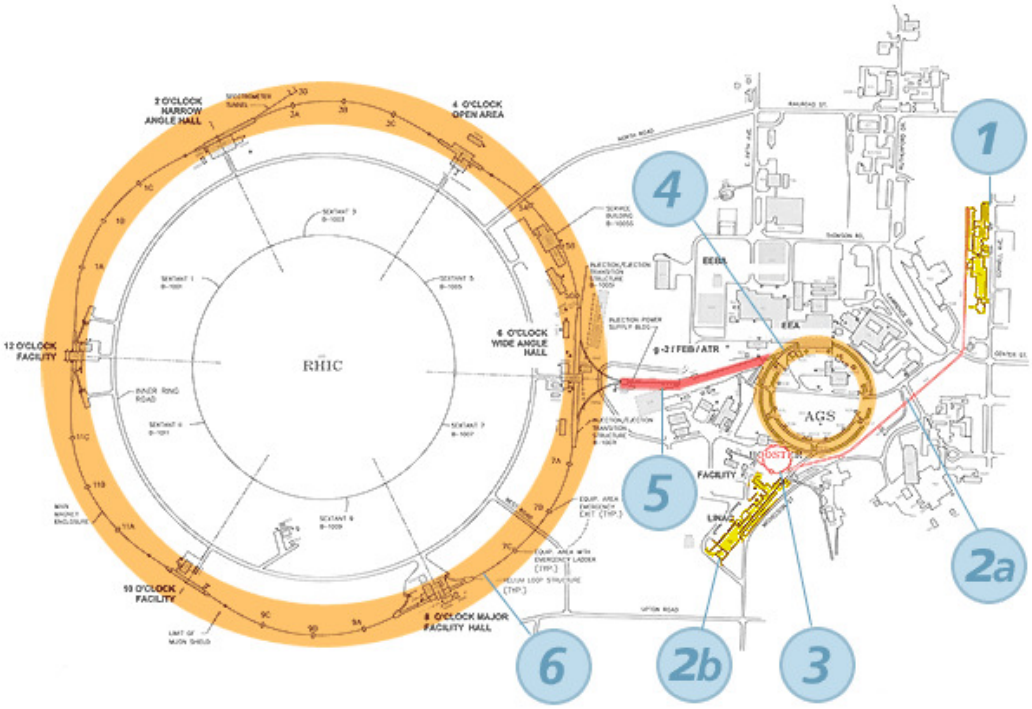

Figure 3.2: A diagram of the Relativistic Heavy Ion Collider (RHIC) complex at Brookhaven National Laboratory. The complex is composed of long chain of particle accelerators.

RHIC is built to accelerate and collide heavy ions and polarized protons with high luminosity. It is an intersecting storage ring particle accelerator with two independent rings, labeled "blue" and "yellow", sharing a common horizontal plane in the tunnel. The RHIC double storage ring has a rounded hexagonal shape with a circumference of 3834 m. The beam is steered via 1,740 superconducting magnets. Each point where the beams

cross is an interaction point. There are six such locations at RHIC, each described by a clock position as schematically shown in Fig. 3.2. STAR and PHENIX, the only two detectors in operation at the time of writing this dissertation, are located at intersection points corresponding to the 6 o'clock and 8 o'clock positions, respectively. PHOBOS and BRAHMS, located at the 10 o'clock and 2 o'clock positions respectively, are no longer in operation. The remaining two collisions points are for possible expansion.

Given below is a brief introduction to the main features of the STAR detector system at RHIC.

3.2 The STAR Detector

The layout of the STAR detector [54] is shown in Fig. 3.3. STAR was designed primarily for measurements of hadron production over a large solid angle, featuring detector systems for high precision tracking, momentum analysis, and particle identification optimized for the center of mass (c.m.) rapidity region. It consists of several types of detectors, each specializing in detecting certain types of particles or characterizing their motion. Data from these detectors are recorded by an advanced data acquisition (DAQ) system. The main detector subsystems are: Time Projection Chamber (TPC), Forward Time Projection Chamber (FTPC), Time of Flight (ToF), Beam-Beam Counters (BBC), Vertex Position Detector (VPD), Photon Multiplicity Detector (PMD), Forward Pion Detector (FPD), Barrel Electro-Magnetic Calorimeter (BEMC), Endcap Electro-Magnetic Calorimeter (EEMC) and Zero Degree Calorimeter (ZDC). Fig. 3.4 shows the cross-section of the STAR detectors used in the year 2010.

In the analysis for this dissertation, I only used the Time Projection Chamber (TPC), the Forward TPCs (FTPC), Beam Beam Counters (BBC), Vertex Position Detector (VPD), Time of flight detector (TOF) and Zero Degree Calorimeter (ZDC). The TPC was used for

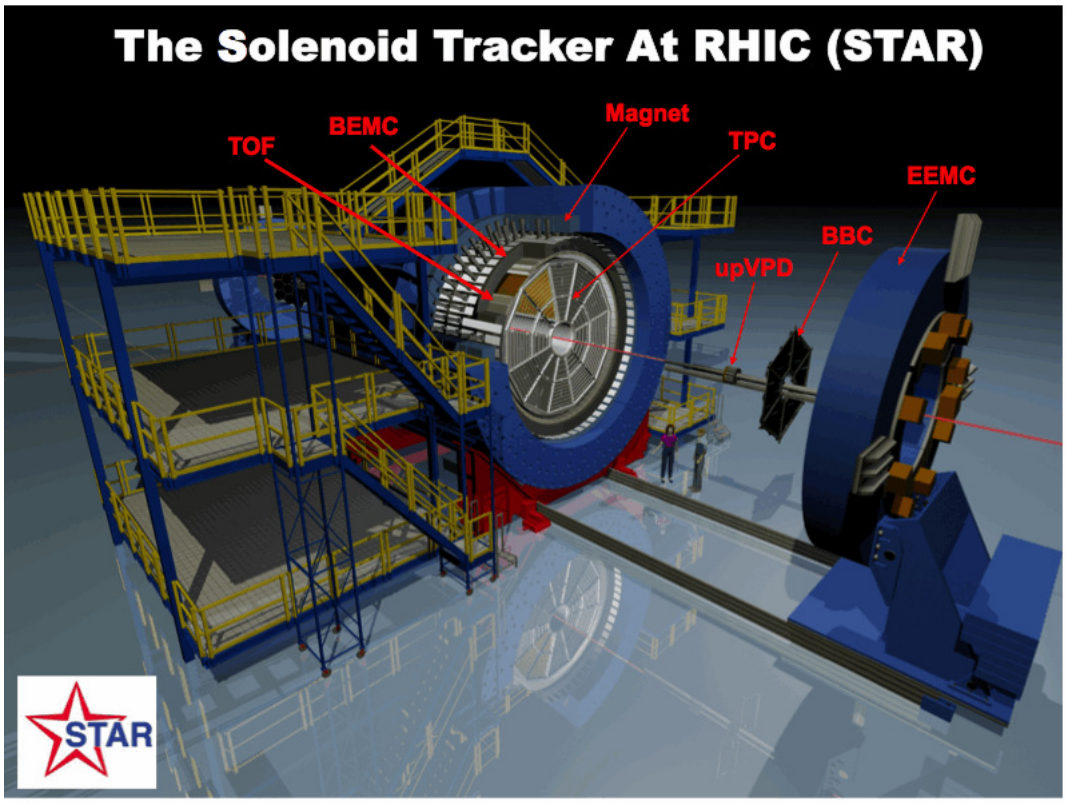

Figure 3.3: The STAR detector systems showing the location of the detector subsystems.

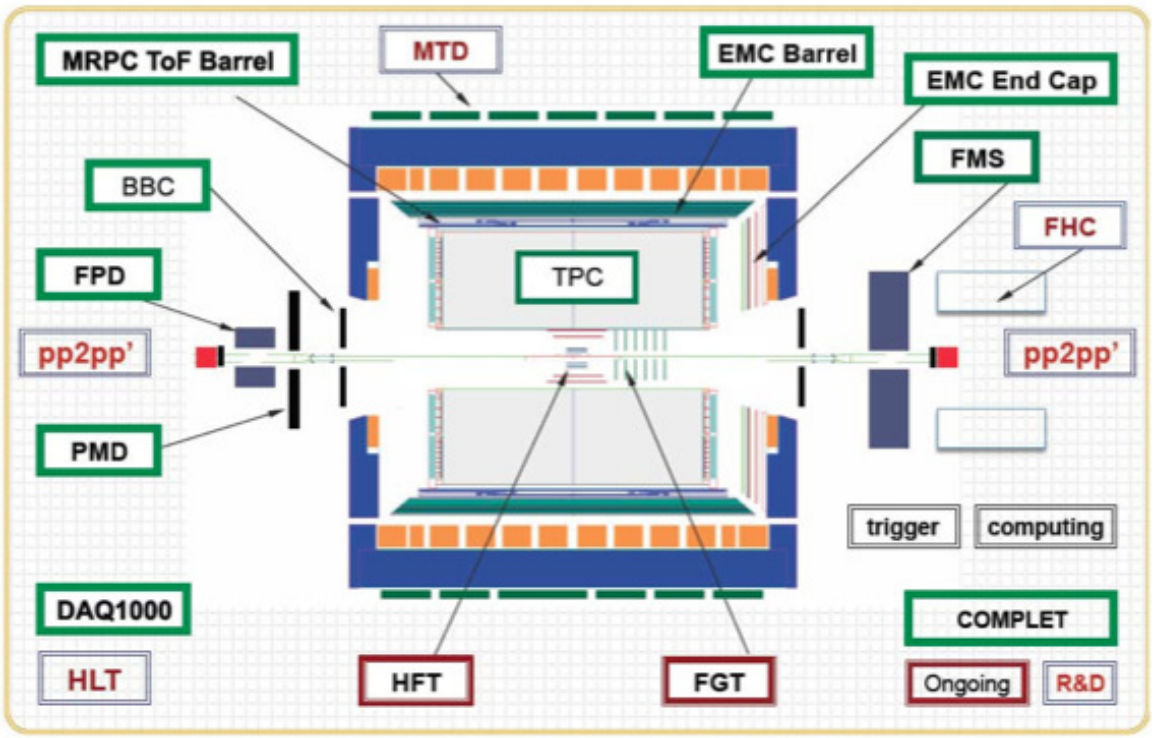

Figure 3.4: Cross-section of the STAR detectors used in year 2010 showing the location of the detector sub-systems.

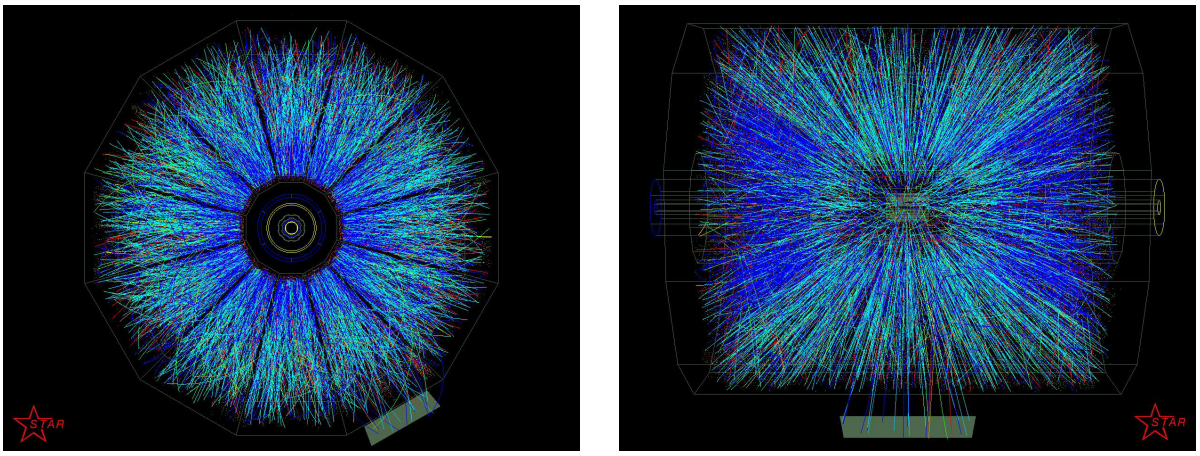

Figure 3.5: Beam's eye (left) and side (right) views of a central AuAu collision at 200 GeV.

tracking in the midrapidity region, and the FTPC was used in the forward rapidity region. A combination of information from TPC and TOF was used for particle identification, and BBC information was used to reconstruct the first-order event plane at beam energies of 39 GeV and below. At higher RHIC energies, the ZDC was used as a trigger detector. What follows is a brief introduction to these detector subsystems.

3.2.1 The Time Projection Chamber

The TPC is the primary tracking device of the STAR detector [55]. It records the tracks of particles, measures their momenta, and identifies the particles by measuring their ionization energy loss (dE/dx). Its acceptance covers ± 1.8 units of pseudorapidity through the full azimuthal angle and over the full range of multiplicities.

The STAR TPC is shown schematically in Fig. 3.6. It is located inside a large solenoidal magnet that operates at 0.5 T [56]. The TPC is 4.2 m long and 4.0 m in diameter. The cylinder is concentric with the beam pipe, and the inner and outer radii of the active volume are 0.5 m and 2.0 m, respectively.

The TPC is divided into two parts by the central membrane which is typically held

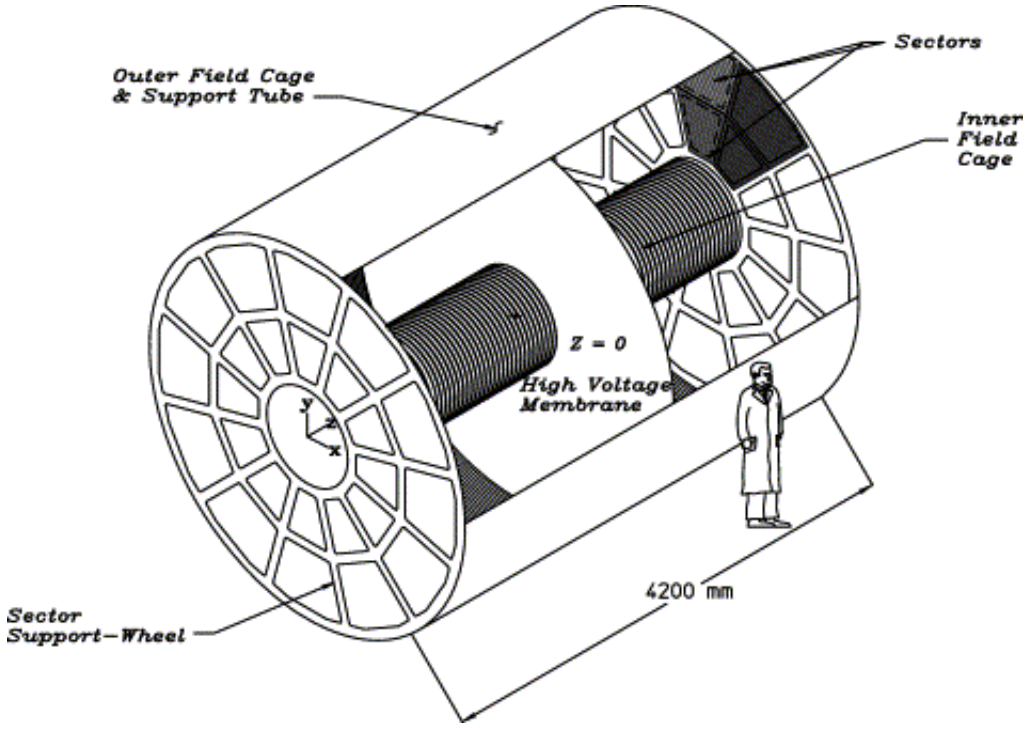

Figure 3.6: The STAR TPC is centered on the 6 o'clock intersection region at RHIC. This figure is taken from Ref. [55].

at 28 kV high voltage. A chain of resistors and equipotential rings along the inner and outer field cage create a uniform drift field $\sim$ 135 V/cm from the central membrane to the ground planes, where anode wires and pad planes are organized into 12 sectors for each sub-volume of the TPC. The volume of the TPC is filled with P10 gas (10% methane, 90% argon) regulated at 2 mbar above atmospheric pressure to minimize any air leakage inside (even a low level of oxygen contamination would disable the TPC). The electron drift velocity in P10 gas is relatively fast, 5.45 cm/μs at 130 V/cm drift field.

The charged particles traversing the TPC experience ionization energy loss (dE/dx) and liberate electrons from the TPC gas. These electrons drift through the gas towards the end-cap planes of the TPC. There, the signal induced on readout pads is amplified and integrated by a circuit containing a pre-amplifier and a shaper. It is digitized and then

transmitted through a set of optical fibers to the STAR DAQ.

Given the time of the collision, and the read-out time and location, it is possible to reconstruct the 3D spatial coordinates of any ionization event in the TPC. This allows the full 3D reconstruction of tracks in the TPC. The Time Projection Chamber Tracker (TPT) software is then used to reconstruct tracks by helical trajectory fits. The resulting track information from the TPC is combined with any other available position information and then refit by application of a Kalman filter routine — a complete and robust statistical treatment [57]. The primary collision vertex is reconstructed from these global tracks. A refit of these tracks is performed by a constrained Kalman fit that requires the distance of closest approach (DCA) to the primary vertex be less than 3 cm. The reconstruction efficiency, including the detector acceptance for primary tracks, depends on the particle type, track quality cuts, track momentum, event multiplicity, etc.

The mean energy loss per unit distance for a particle with charge z and speed $\beta = v/c$ passing through the TPC gas is given by the well-known Bethe-Bloch formula

$$-\frac{dE}{dx} = Kz^2\frac{Z}{A}\frac{1}{\beta^2}\left[\frac{1}{2}\ln\frac{2m_e c^2\beta^2\gamma^2 T_{\max}}{I^2} - \beta^2 - \frac{\delta}{2}\right] \tag{3.1}$$

where $T_{\max}$ is the maximum kinetic energy which can be imparted to a free electron in a single collision; the variables are defined in Table 3-1.

The mean energy deposited depends on the momentum of the particle, the charge it carries, its mass and the target material. This means that in some kinematic ranges, it is possible to determine the type of particle based on the mean energy deposited in the hits that make up the track. Fig. 3.7 represents a standard plot from STAR where dE/dx is plotted as function of reconstructed total momentum p for all tracks in a large number of events. The points cluster around the characteristic bands for the various particles whose ideal dE/dx curves have been superimposed.

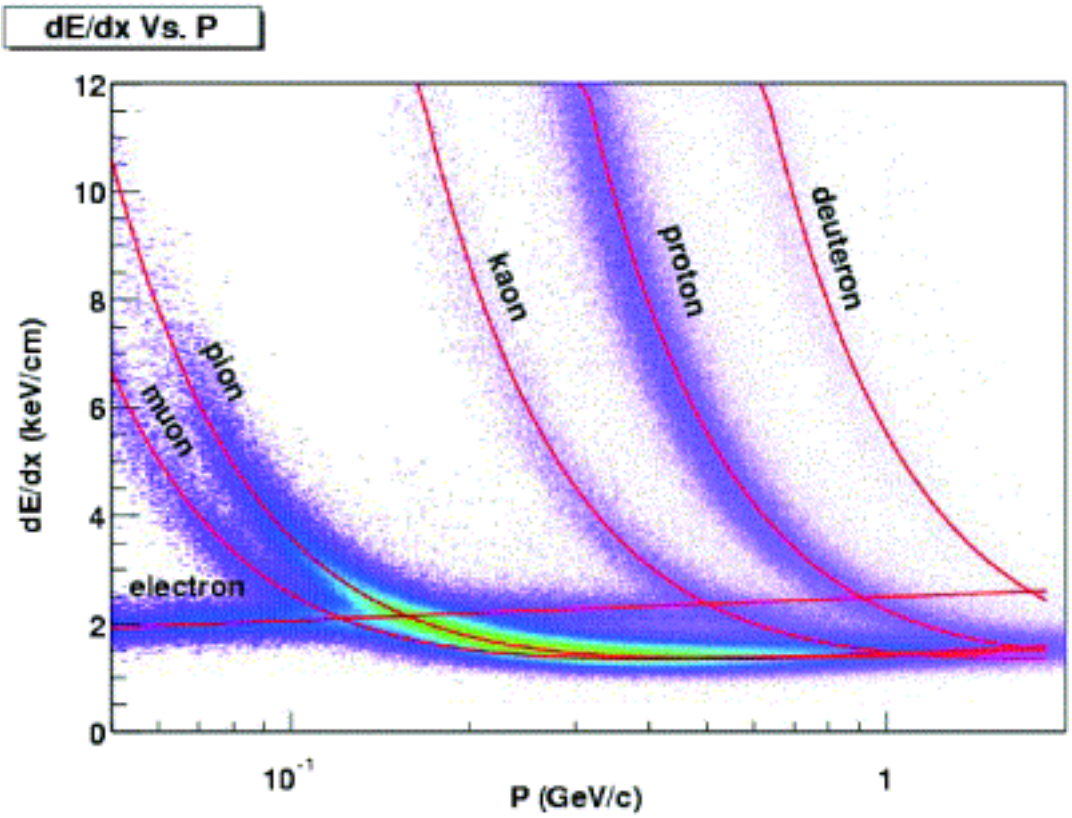

Figure 3.7: The energy loss (dE/dx) distribution for various particles as measured by the TPC as a function of total momentum (p) of the particles.

Quantities	Definitions	Value or Unit
dE/dx	Ionization energy loss per unit length	MeV g^{-1} cm^2
x	$x = \rho L$	g cm^{-2}
ρ	Density of the absorber	g cm^{-3}
L	Length	cm
$\beta = v/c$	Velocity of the particle	
$m_e c^2$	Electron mass $\times c^2$	0.510998918(44) MeV
T	Kinetic energy of the particle	MeV
r_e	Classical electron radius $r_e = \frac{e^2}{4\pi\epsilon_0 m_e c^2}$	2.817940325(28) fm
I	Mean excitation energy	eV
N_A	Avogadro's number	6.0221415(10)$\times 10^{23}$ /mol
Z	Atomic charge of absorber	
A	Atomic mass number of absorber	g/mol
z	Charge number of particle	
$\delta(\beta\gamma)$	Density effect correction to dE/dx	

Table 3-1: Definition of symbols in Bethe-Bloch formula.

3.2.2 Forward Time Projection Chamber

The Forward Time Projection Chamber (FTPC) [58] was constructed to extend the acceptance of the STAR experiment. It covers the pseudorapidity range $2.5 < |\eta| < 4.2$ on both sides of STAR (see Fig. 3.3 and Fig. 3.4). It has lower momentum resolution than the central TPC.

3.2.3 Beam Beam Counters

The Beam Beam Counters (BBC) [59] consist of two arrays of scintillating detectors for charge-particle detection. The BBC detectors are mounted on the outside of the east and west poletips of the STAR magnet. Each BBC is made up of two inner rings and two outer rings of scintillating tiles (see Fig. 3.9) with the inner rings covering pseudorapidity $3.3 < \eta < 5.2$ while the outer rings cover $2.2 < \eta < 3.4$. The BBC is a very fast detector and hence is capable of rapidly counting the total number of particles crossing its plane. Therefore it is used to trigger events where the use of ZDCs is impossible or impractical

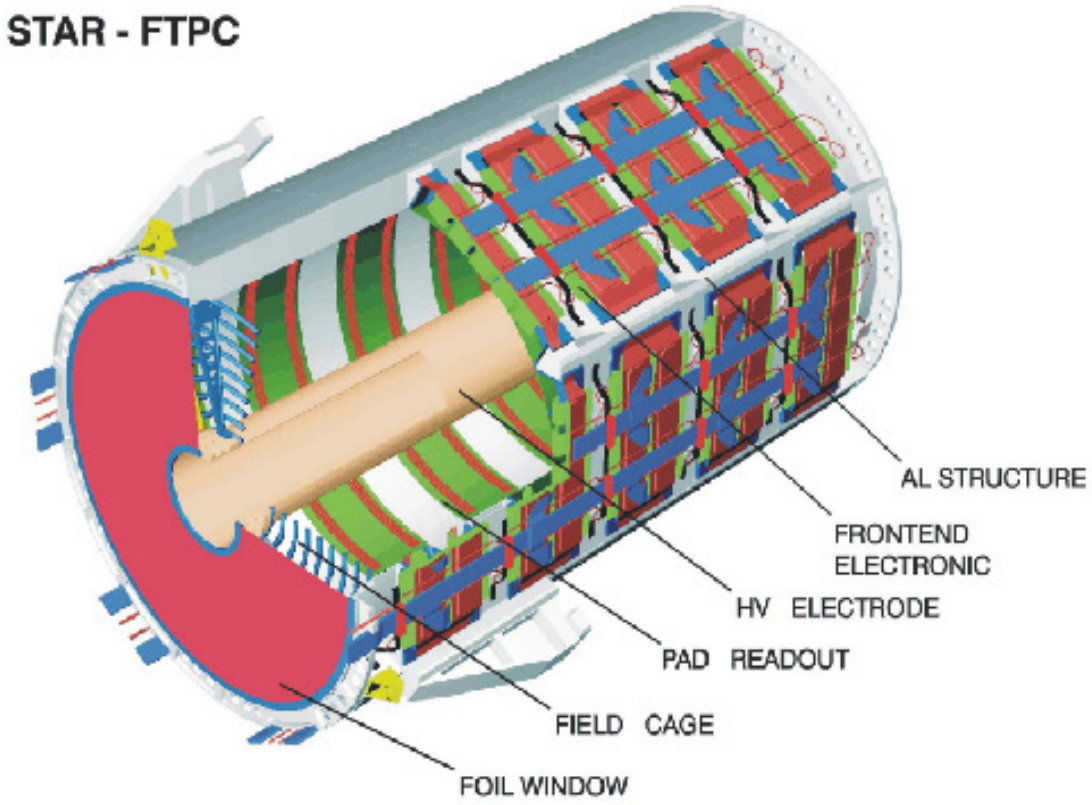

Figure 3.8: Forward Time Projection Chamber.

due to the low neutron content of the colliding nuclei, as is the case for pp collisions. The BBCs are quite helpful for triggering at low beam energies, where the ZDC acceptance is far too small for them to be used for this purpose. BBCs can also be used as vertexing detectors. The z position of the collision can be determined by comparing the arrival time of collision remnants at each of the BBC faces. For beam energies below 39 GeV, BBCs can be used as a reaction plane detector. In addition to the above, the BBCs are also used to monitor the beam quality during the experimental runs.

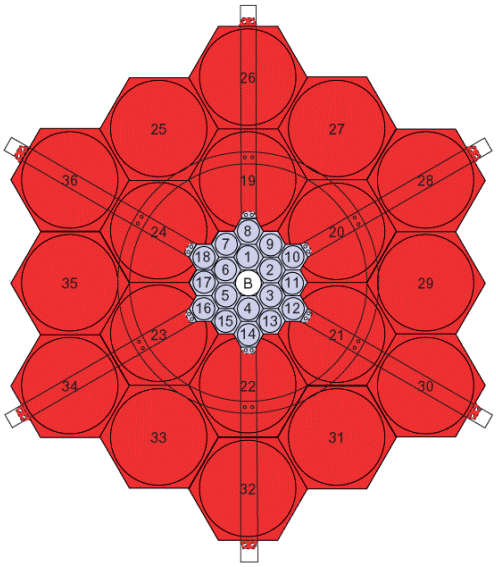

Figure 3.9: A diagram of the STAR Beam Beam Counters: a similar array is located on both the east and west sides of the STAR detector.

3.2.4 Time of Flight

A full barrel Time-of-flight (TOF) detector is positioned just outside the TPC, covering $\eta < 1$ in pseudorapidity and 2π in azimuth. It extends the direct particle identification (PID) capabilities of STAR to higher momenta. The TOF system doubles the probability of directly identifying charged particles compared with the TPC only, and allows more than 95% of all of the charged particles in an average event to be positively identified. The

TOF system extends kaon-pion separation up to 1.6 GeV/c and proton separation up to 2.8 GeV/c [60].

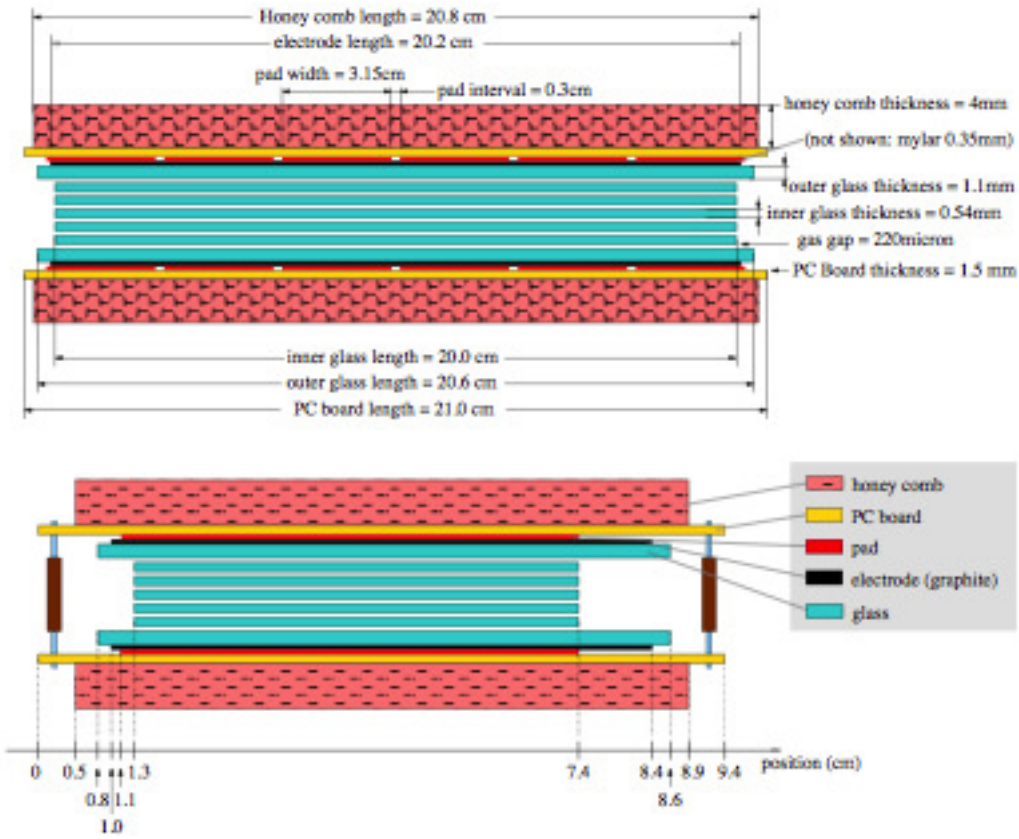

Figure 3.10: Two side views of a Multigap Resistive Plate Chamber (MRPC) module. The figure is taken from Ref. [60].

The active detector in the TOF system is a Multigap Resistive Plate Chamber (MRPC), of which there are 3840 in total. These MRPC modules are mounted inside trays. There are 120 trays positioned in two rings of 60 trays each, and each tray holds 32 MRPC modules. Each MRPC is a stack of glass plates with 220 μm-wide gaps in between each plate [60].

The detectors are bathed in a gas mixture of 95% freon R-134a and 5% isobutane. Graphite electrodes are located on the outside of the outermost plates, and a 14 kV potential difference is applied as $\pm$ 7 kV on each electrode. Outside these electrodes are printed circuit boards with copper pickup pads. There are six pickup pads in each MRPC, and each pad is 3.15 cm wide (x direction) and 6.1 cm long (in the z direction, along the beam axis). When a charged particle travels through an MRPC, primary ionization occurs in the gas gaps between the glass plates.

The primary ionization and the strong electric field in the gaps results in avalanches of millions of electrons. The signal in the pickup pads is the image charge formed from the sum of these avalanches in the different gaps. This signal is then amplified and digitized in electronics that are mounted on each tray. These electronics consist of the following circuit boards. First, a board called TINO amplifies and discriminates the MRPC signals. Then, a time-to-digital converter (TDC) card called TDIG receives the input signals from the TINO card and records the time information relative to an external 40 MHz clock using a high-performance TDC chip (HPTDC), which was developed at CERN. Then a buffer card (TCPU) collects and stores the time information from the eight TDIG boards on one tray of the TOF system. Another board then collects the information from 30 TCPU cards and sends it to the STAR Data Acquisition (DAQ) system.

3.2.5 VPD

Two identical pseudo-vertex position detectors (pVPD) provide a starting time for TOF detectors. These start detectors are located on each side of the STAR detector, very close to the beam pipe, at a distance of 5.6 m from the center of STAR. Each detector consists of 19 Hamamatsu fine-mesh dynode photomultiplier tubes [60]. The pVPDs are also used together with a minimum-bias trigger to constrain the V_z of collected events. Each pVPD

Figure 3.11: Pseudo-vertex position detector (pVPD), with one located on each side of the STAR detector

consists of detecting element tubes covering 19% of the total solid angle in $4.43 < |\eta| < 4.94$. The timing resolution of the start time depends on the multiplicity. For example, the effective timing resolution of the start time is 25 ps, 85 ps, and 140 ps for 200 GeV AuAu, dAu and pp collisions, respectively.

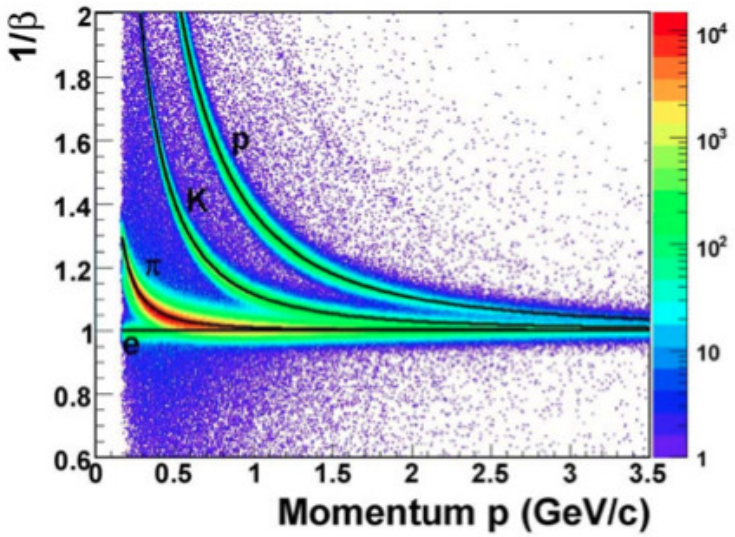

Figure 3.12: Particle identification using the STAR Time of Flight (TOF) detector. Proton, kaon, pion and electron bands are clearly separated.

3.2.6 ZDC

The Zero Degree Calorimeter (ZDC) is made up of small hadron calorimeters located downstream (east and west) of the interaction region. The ZDC is placed at ≈ 18 m from the center of STAR and subtends a solid angle of approximately 30μsr. Each ZDC consists of 3 modules containing a series of tungsten plates. The ZDCs measure the energy of neutrons associated with the spectator matter, and they are used for beam monitoring, triggering and locating interaction vertices [63, 64].

3.2.7 The STAR Trigger

The STAR trigger is a pipelined system in which digitized signals from the fast trigger detectors are examined at the RHIC crossing rate ($\sim$ 10 MHz). This information is used to decide whether to begin the amplification-digitization-acquisition cycle for slower, more finely grained detectors. The slow detectors like the TPC, FTPC, TOF, etc., provide momentum and particle identification on which physics conclusions are based, but they can only operate at rates of up to $\sim$ 1000 Hz (and much slower in the years prior to 2010). Interaction rates approach the RHIC crossing rates for the highest luminosity beams, so the fast detectors must provide a means to reduce the rate by up to 5 orders of magnitude. Interactions are, therefore, selected based on the distributions of particles and energy obtained from the fast trigger detectors, like the BBC, the ZDC, etc.

The trigger system is divided into 4 different levels. The first three levels, 0, 1, and 2, are based on fast detector information. The final trigger decision is made in level 3 based on simplified online tracking in the slow detectors. This trigger also provides an online visual display of the events almost in real time as shown in Fig. 3.5.

The ZDC serves as a main trigger detector at top RHIC energies. BBC and VPD also serve as trigger detectors, especially for low beam energies where the efficiency of the ZDC becomes poor.

Chapter 4

ANALYSIS DETAILS

In this chapter, I present the selection criteria for events and tracks, event plane determination, the analysis methods for directed flow (v_1), elliptic flow (v_2), triangular flow (v_3) and the first flow harmonic associated with dipole asymmetry in the initial geometry. I also discuss the estimation of systematic uncertainties on these measurements.

4.1 Data Sets

Directed flow analysis from the Beam Energy Scan (BES) data set is the main focus of this dissertation. These data were taken for center of mass energies at 7.7, 11.5 and 39 GeV in the year 2010 and at 19.6 and 27 GeV in the year 2011. This same data set is analyzed for elliptic flow measurement for charged particles. Data from low beam energy test runs for AuAu collisions at 9.2 GeV taken in the year 2008 and for CuCu collisions at 22.4 GeV taken in the year 2005 were also analyzed for directed and elliptic flow measurements.

The other important component of this dissertation is measurement of triangular flow and the first flow harmonic associated with dipole asymmetry in the initial geometry. These odd harmonic coefficients were overlooked until recently and the first measurement of these observables by the STAR collaboration are reported in this dissertation. For these measurements, we focused on the data from Au+Au collisions at 200 GeV from the year 2004. The data with production and trigger

System	Beam Energy	TriggerSetup Name	Production	Trigger ID
AuAu	7.7 GeV	AuAu7_Production	P10ih	28001,28002
	11.5 GeV	AuAu11_Production	P10ih	31004,310014
	19.6 GeV	AuAu19_Production	P11id	340001,11,21
	27 GeV	AuAu19_Production	P11id	360001,360002
	39 GeV	AuAu39_Production	P10ih	290001
	9.2 GeV	lowEnergy2008&bbcvpd	P08ic	all
CuCu	22.4 GeV	cu22ProductionMinBias	P05if	86011
AuAu	200 GeV	ProductionMinBias	P05ic	15007

Table 4-1: Data Sets and trigger selection used in the analysis.

information are summarized in Table 4-1. The optimal event and track quality cuts were decided based on a systematic study of data quality.

4.1.1 Event Selection

Events for analysis are selected based on the collision vertex positions v_x and v_y being within 2 cm of the beam axis to reduce contributions from beam-gas and beam-pipe (radius = 4 cm) interactions, and within a limited distance from the center of the detector along the beam direction, v_z. We require v_z to lie within ± 70 cm for the 7.7 GeV data set, within ± 50 cm for the 11.5 GeV data set, and within ± 40 cm for the 19.6, 27 and 39 GeV data sets. The selected events have BBCAdcSum (sum of total ADC counts from east and west BBC for small inner tiles) greater than 75 for 7.7 and 11.5 GeV and greater than 150 for 19.6, 27 and 39 GeV. This selection further removes the background events. These values are chosen to reduce systematic errors due to variance in detector performance over $|\eta| < 1.0$ while retaining sufficient statistics. The $0 - 80\%$ central events (centrality definition follows) divided in 9 narrow centrality bins are used for the analysis. The results from more peripheral collisions are not presented due to trigger inefficiencies at low multiplicity.

System	Beam Energy	$v_z(\mathrm{cm})$	v_r	BBCAdc Sum	No of Events
AuAu	7.7 GeV	70 cm	2 cm	75	3.9 M
AuAu	11.5 GeV	50 cm	2 cm	75	10.5 M
AuAu	19.6 GeV	40 cm	2 cm	150	19.2 M
AuAu	27 GeV	40 cm	2 cm	150	38.9 M
AuAu	39 GeV	40 cm	2 cm	150	36.7 M
AuAu	9.2 GeV	75 cm	2 cm	NA	0.3 M
CuCu	22.4 GeV	30 cm	2 cm	NA	2.0 M
AuAu	200 GeV	30 cm	2 cm	NA	10.0 M

Table 4-2: Event Selections

In 9.2 GeV AuAu collisions and 22.4 GeV CuCu collisions, 0-60% central minimum bias data is analyzed. Differential analysis in narrow centrality bins was not possible due to lack of statistics. Events useful for our analysis are listed in Table 4-2.

4.1.2 Centrality Determination

The centrality classes are defined based on the uncorrected charged particle multiplicity ($N_{\mathrm{ch}}^{\mathrm{raw}}$) distribution in the TPC for pseudorapidity $|\eta| < 0.5$ and full azimuth. Figure 4.1 shows the $N_{\mathrm{ch}}^{\mathrm{raw}}$ distribution for charged particles from the data at $\sqrt{s}_{NN}$ = 7.7, 11.5, 19.6, 27 and 39 GeV compared to those from Monte Carlo (MC) Glauber simulations. A two-component model [65] is used to calculate the simulated multiplicity distribution given by

$$\frac{dN_{\mathrm{ch}}}{d\eta} = n_{pp}\left[(1-x)\frac{N_{\mathrm{part}}}{2} + xN_{\mathrm{coll}}\right], \tag{4.1}$$

where N_{part} is the number of participant nucleons and N_{coll} is the number of binary nucleon-nucleon collisions in the simulations. The fitting parameter n_{pp} is the average multiplicity per unit of pseudorapidity in minimum-bias pp collisions and x is a parameter (determined experimentally) which reflects the extent to which heavy

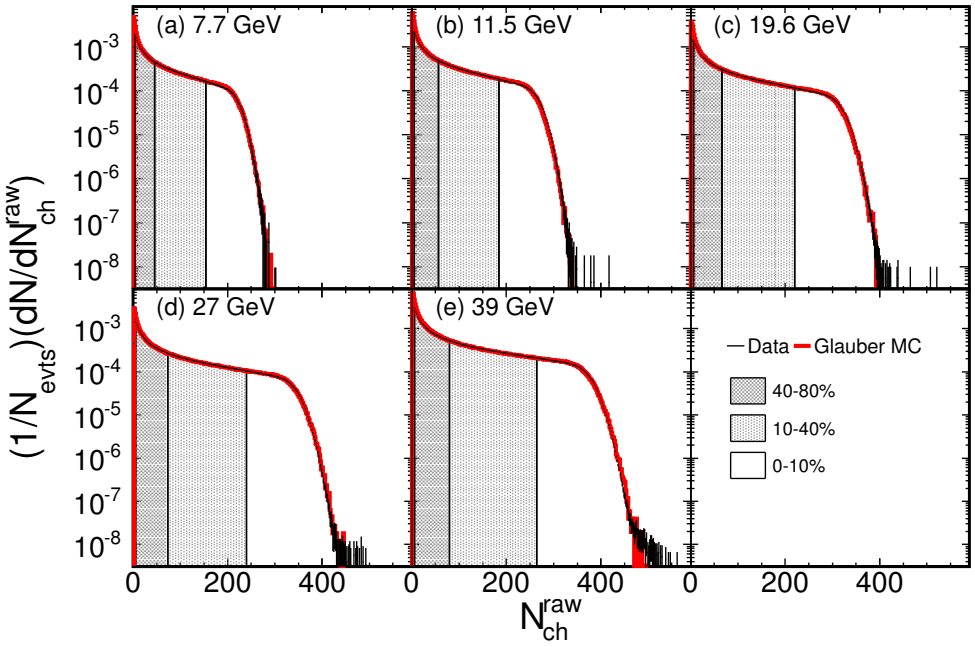

Figure 4.1: Uncorrected $dN/d\eta$ measured within $|\eta| < 0.5$ in the TPC from $\sqrt{s}_{NN}$ = 7.7 to 39 GeV in AuAu collisions shown as black points. The red curves show the multiplicity distributions at $\sqrt{s}_{NN}$ = 7.7 to 39 GeV from Monte Carlo Glauber simulations.

ion collisions deviate from a simple superposition of nucleon-nucleon collisions. The inelastic nucleon-nucleon cross section $\sigma_{NN}^{\rm inel}$ is extracted from fitting the results of available data for total and elastic pp cross sections from the Particle Data Group [66]. The x value is fixed at 0.12 $\pm$ 0.02 based on the linear interpolation of the PHOBOS results at $\sqrt{s}_{NN}$ = 19.6 and 200 GeV [67]. Systematic errors on n_{pp} are evaluated by varying both n_{pp} and x within the quoted x error to determine the minimum χ^2 to describe the data. Since n_{pp} and x are anti-correlated, lower (higher) n_{pp} is used for higher (lower) x for systematic error evaluations on $N_{\rm part}$. Table 4-3 summarizes the parameters in the two-component model and $\sigma_{NN}^{\rm inel}$ in the MC Glauber simulations. The event-by-event multiplicity fluctuations are included using negative binomial distributions [68]. The centrality classes are

defined by the fractions of geometrical cross section from the simulated multiplicity distributions. For each centrality bin, average quantities are calculated in the Monte Carlo Glauber simulations for $\langle N_{\rm part}\rangle$, $\langle N_{\rm coll}\rangle$, reaction plane eccentricity $\langle \varepsilon_{\rm RP}\rangle$, participant eccentricity $\langle \varepsilon_{\rm part}\rangle$, root mean square of participant eccentricity $\varepsilon_{\rm part}\{2\}$, and transverse area $\langle S_{\rm part}\rangle$. Eccentricity and transverse area are defined by

$$\varepsilon_{\rm RP} = \frac{\sigma_y^2 - \sigma_x^2}{\sigma_x^2 + \sigma_y^2}, \tag{4.2}$$

$$\varepsilon_{\rm part} = \frac{\sqrt{(\sigma_y^2 - \sigma_x^2)^2 + 4\sigma_{xy}^2}}{\sigma_x^2 + \sigma_y^2},\ \ \varepsilon_{\rm part}\{2\} = \sqrt{\langle \varepsilon_{\rm part}^2\rangle}, \tag{4.3}$$

$$S_{\rm part} = \pi\sqrt{\sigma_x^2\sigma_y^2 - \sigma_{xy}^2}, \tag{4.4}$$

$$\sigma_x^2 = \{x^2\} - \{x\}^2,\ \ \sigma_y^2 = \{y^2\} - \{y\}^2, \tag{4.5}$$

$$\sigma_{xy} = \{xy\} - \{x\}\{y\}, \tag{4.6}$$

where the curly brackets in Eqs. (4.5) and (4.6) denote the average over all participants per event, and x and y are the positions of participant nucleons. Systematic uncertainties on those quantities are evaluated by varying parameters for the two-component model and by varying the input parameters in the Monte Carlo Glauber model. The quoted errors are the sum in quadrature of the individual systematic uncertainties.

(GeV)	n_{pp}	$\sigma_{NN}^{\rm inel}$ (mb)
7.7	0.89 $\pm$ 0.04	30.8 $\pm$ 1.0
11.5	1.07 $\pm$ 0.05	31.2 $\pm$ 1.0
19.6	1.29 $\pm$ 0.05	32.0 $\pm$ 1.0
27	1.39 $\pm$ 0.06	33.0 $\pm$ 1.0
39	1.52 $\pm$ 0.08	34.0 $\pm$ 1.0

Table 4-3: Summary of n_{pp} and $\sigma_{NN}^{\rm inel}$ with systematic uncertainties at $\sqrt{s}_{NN}$ = 7.7, 11.5, 19.6, 27 and 39 GeV. x is set to 0.12 $\pm$ 0.02 for all collision energies.

4.1.3 Track Selections

Various track quality cuts are used to select good charged particle tracks reconstructed using information from the TPC or FTPCs. The distance of closest approach (DCA) of the track to the primary vertex is taken to be less than 3 cm. We require that in the TPC and FTPCs, the number of fit points used for reconstruction of the tracks must be greater than 15 and 5, respectively. For the TPC and FTPCs, the ratio of the number of fit points to the maximum possible number of points for that trajectory is required to be greater than 0.52. This requirement prevents a single track being analyzed as two separate tracks if it is split into two segments during reconstruction. An additional transverse momentum cut ($0.2 < p_T < 2$ GeV/c) is applied to the charged tracks for the event plane reconstruction in TPC and FTPC.

4.1.4 Particle Identification

Particles such as protons, pions and kaons can be identified by determining their mass or the way they interact or decay. The momentum and charge sign of the charged particles can be determined by measuring the curvature and direction of the tracks in the detector. To identify hadrons and leptons unambiguously, their charge and mass have to be determined by measuring the momentum and velocity simultaneously.

For the data taken in 2010 and later, I use STAR's new Time of Flight detector to identify particles in combination with TPC information. The TOF detector measures flight time of a particle from the primary vertex of the collisions to the point where the particle crosses the TOF barrel. Once the time of flight and

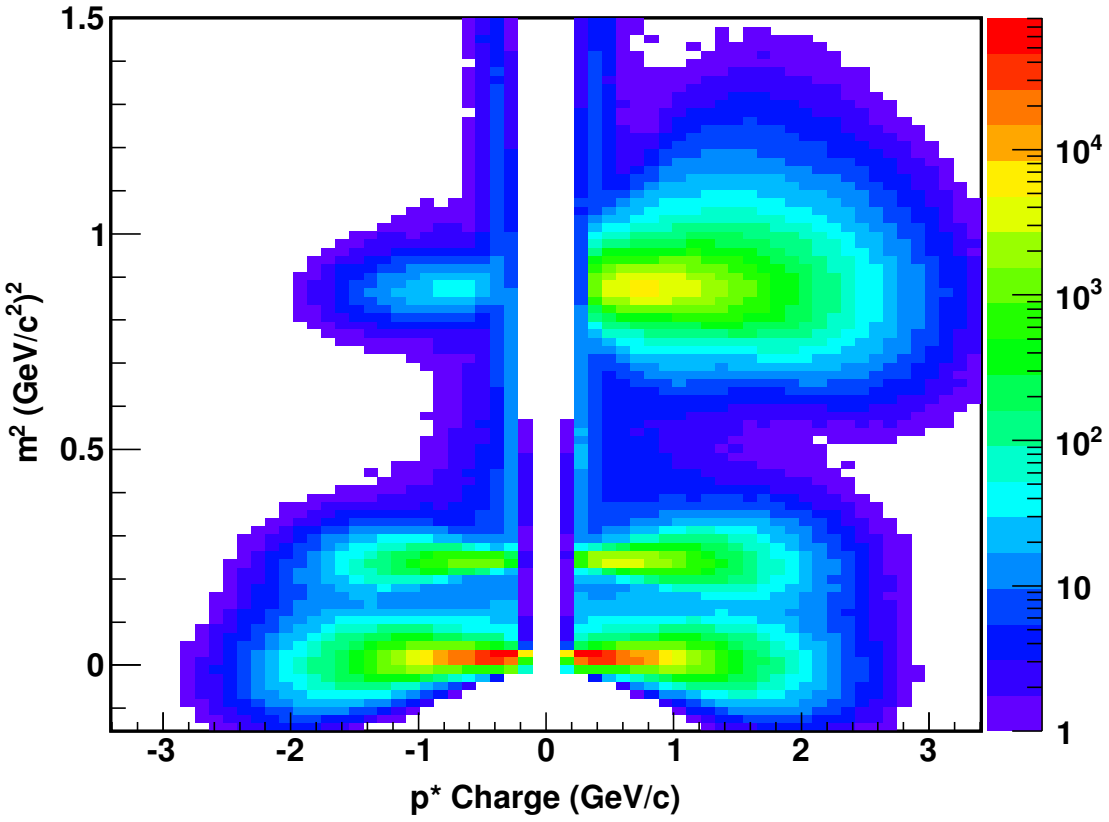

Figure 4.2: Mass squared versus magnetic rigidity (momentum per charge) for AuAu collisions at $\sqrt{s}_{NN}$ =7.7 GeV.

path length information are obtained, one can directly calculate the velocity of the particle. Mass squared versus rigidity for AuAu collisions at 7.7 GeV is shown in Fig 4.2, where protons, pions and kaon bands are clearly separated. In this analysis, I use a mass squared cut $0.8 < m^2 < 1.0$ GeV$^2/c^4$ to select proton and anti-proton, $-0.01 < m^2 < 0.10$ GeV$^2/c^4$ to select pions and $0.20 < m^2 < 0.35$ GeV$^2/c^4$ to select kaons. All particles were required to be within 2σ from the center of the appropriate dE/dx band in the TPC. We can identify protons up to 2.8 GeV/c in total momentum and charged pions and kaons up to a total momentum of 1.6 GeV/c.

4.2 Flow Analysis Methods

There are several methods available for the anisotropic flow analysis. Mainly these methods are based on two-particle correlations and multi-particle correlations. Multi-particle correlation methods are less sensitive to non-flow and flow fluctuations, but they are statistics-hungry, whereas two-particle methods are sensitive to non-flow correlations and flow fluctuations, but can offer an advantage when the sample size is small. Standard event plane methods are the best compromise between these two methods.

4.2.1 Event Plane method

One can evaluate flow components correlating particles with the reaction plane. The reaction plane is defined by the beam axis and the vector connecting the centers of the two colliding nuclei. For high energy collisions in the laboratory reference frame, the colliding nuclei are Lorentz-contracted along the beam axis. As such, the vector connecting the colliding nuclei is nearly perpendicular to the beam axis and the reaction plane can be characterized by its azimuthal angle. The real reaction plane is not known, but the event plane, an experimental estimator of the true reaction plane, can be calculated [14]. If the event plane is estimated from the m-th order of flow component, then we speak of the m-th order event plane. With the observed event plane instead of the true reaction plane, we have

$$v_n = \langle \cos n(\phi_i - \Psi_r) \rangle \quad = \frac{\langle \cos n(\phi_i - \Psi_m) \rangle}{\langle \cos n(\Psi_m - \Psi_r) \rangle} \tag{4.7}$$

where ϕ denotes a particle's azimuthal angle, Ψ_r represents the azimuthal angle of the reaction plane, and Ψ_m is the m-th order event plane. The numerator of Eq.

4.7 is considered to be the observed flow value, and the denominator characterizes the event plane resolution. In general, better accuracy for determination of v_n is obtained with the event plane of order n ($= km$) estimated from the same harmonic ($m = n,\ k = 1$). That is because the resolution deteriorates as k increases (see a detailed discussion on event plane resolution below).

In the STAR experiment, detectors can be classified into two categories: track-based detectors such as the TPC and FTPCs, and hit-based detectors like the ZDC-SMD and BBC. Correspondingly, the estimation of the reaction plane has different approaches, depending on which detector is involved.

4.2.2 Estimation of Event Plane from TPC/FTPC

In track-based detectors, i.e TPC/FTPC, the event plane vector Q_n and the event plane angle Ψ_n from the nth harmonic of the particle azimuthal distribution are defined by the equations,

$$Q_n \cos(n\Psi_n) \;=\; Q_{nx} \;=\; \sum_i w_i \cos(n\phi_i), \tag{4.8}$$

$$Q_n \sin(n\Psi_n) \;=\; Q_{ny} \;=\; \sum_i w_i \sin(n\phi_i), \tag{4.9}$$

$$\Psi_n \;=\; \left(\tan^{-1}\frac{Q_{ny}}{Q_{nx}}\right)/n, \tag{4.10}$$

where sums go over all particles i used in the event plane calculation, and ϕ_i and w_i are the laboratory azimuthal angle and the weight for the i-th particle, respectively. For second and higher order event plane calculations, the weight factor $w = p_T$ in units of GeV/c for $p_T < 2$ GeV/c, and $w = 2$ GeV/c for $p_T \geq 2$ GeV/c. This helps to minimize the effects of jets in event plane calculation. Tracks used

for the calculation of v_n are excluded from the calculation of the event plane to remove self-correlation effects.

4.2.3 Event Plane with BBC

The Beam-Beam Counter (BBC) geometry is described in Chapter 3 Section 2.4. Since the BBC tiles have a cylindrically symmetric distribution around the beam axis, the event plane vector Q_n and event plane angle Ψ_n can be formulated in the same way as TPC/FTPC method, expect that ϕ_i denotes the fixed azimuthal angle of the center of the ith BBC tile, and w_i is the energy deposition (the ADC signal, A_i) in the ith BBC tile.

$$Q_n \cos(n\Psi_n) = Q_x = \sum_i w_i \cos(n\phi_i), \tag{4.11}$$

$$Q_n \sin(n\Psi_n) = Q_y = \sum_i w_i \sin(n\phi_i), \tag{4.12}$$

$$\Psi_n = \left(\tan^{-1}\frac{Q_y}{Q_x}\right)/n, \tag{4.13}$$

with w_i calculated from the ADC signals A_i, where

$$w_i = \frac{A_i}{\sum A_i} \tag{4.14}$$

The ADC signals A_i are pedestal subtracted and gain corrected values.

4.2.4 Simulation Study of BBC Event Plane

We have performed a simulation study to test the performance of the BBC for first order reaction plane determination. All simulations here are based on the RQMD nuclear transport model [50]. We evaluate how well the BBC works in finding the 1st-order event plane by calculating the RMS value $\langle \cos \Delta\Phi \rangle$, where

$\Delta\Phi$ is the azimuthal difference between the RQMD true reaction plane and the reconstructed event plane based on the simulated BBC response.

In the present BBC configuration, where in a few cases, multiple scintillator tiles are connected to the same photomultiplier tube (PMT), the assigned hit location is the geometical center of the tile combination according to

$$x_{\text{cent}} = \frac{\sum x_i}{N} \tag{4.15}$$

$$y_{\text{cent}} = \frac{\sum y_i}{N} \tag{4.16}$$

where $(x_{\text{cent}}, y_{\text{cent}})$ is the center of the tile and N is the number of tiles connected to the same PMT. We consider the ideal (i.e. perfect) configuration which refers to a perfect hit detector with the same η coverage as the BBC. We assume that all tile efficiencies as well as all PMT efficiencies are 100%. We also assume that PMT signals are linear in the number of particles that are intercepted by the associated tile (or tiles).

The RQMD reaction plane is always along the x-axis in the output files from the RQMD code. We randomize the RQMD reaction planes, and the $\Delta\Psi$ is the difference between the latter angle and the reconstructed azimuth of the event plane based on the simulated BBC output as shown in Fig. 4.3.

4.2.5 BBC Event Plane from Real Data Production

Estimation of event plane using BBC signals involves the following steps.

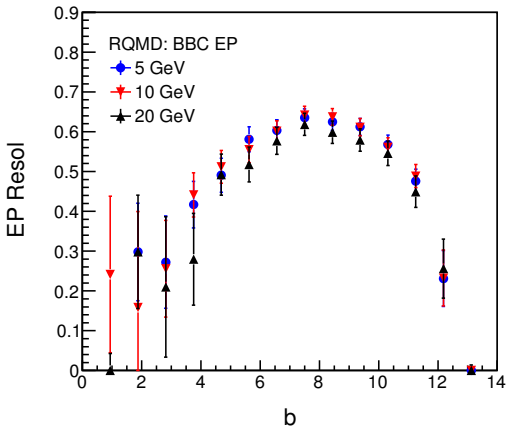

Figure 4.3: BBC first order event plane resolution for RQMD events. This plot is from Ref. [8].

Gain Adjustment for Saturation

The BBC was designed for pp collisions. We need to adjust the high voltage setting such that BBC tiles are not saturated during AuAu collisions, especially for the most central collisions. This adjustment is performed during the data-taking runs. During low-energy running in 2010, we regularly monitored the BBC signals and we adjusted the gain for minimum saturation.

Pedestal Subtraction

Each BBC has 24 ADC (analog-to-digital converter) channels. The pedestal is a normal feature of any design of ADC, and represents the digital output reading when zero analog signal is present at the input. It should not be dependent on the event type used for calibration, and is measured in the standard pedestal run in which all others STAR subsystem detectors are included. Pedestal-subtracted BBC ADC information is used for the event plane calculation.

BBC Channel-by-Chanel Gain Correction

The gain parameters between different BBC channels need to be adjusted so that the response of the detector becomes uniform. The following sections describe how this was accomplished.

BBC Monitoring During the Data Taking The BBC performance was monitored online during BES data taking [69]. We adjusted the high voltage to obtain a uniform detector response.

Gain Factor Calculation The channel-by-channel gain correction factors are calculated during online monitoring of the BBC performance [69]. These gain factors are again calculated from final production and are used to calculate the event plane using BBC. Only the inner small tiles of the BBC with pseudorapidity coverage 3.3 to 5.0 are used in first-order event plane calculation. For gain corrections, we assume that each channel with a similar geometrical configuration and at the same distance from the beam center, has the same mean ADC value averaged over many events.

4.2.6 Event Plane Distribution

The reaction plane in heavy-ion collisions should be randomly distributed. Geometry, granularity and uneven efficiency of the BBC tiles lead to an uneven distribution of the 1st-order event plane, as shown (in black) in Fig. 4.9. Such raw event planes can not be applied directly in a flow analysis, since they have some preference in the orientation, which will introduce systematic errors [70]. There are various methods to correct for these effects. Some of the event plane flattening methods are discussed below.

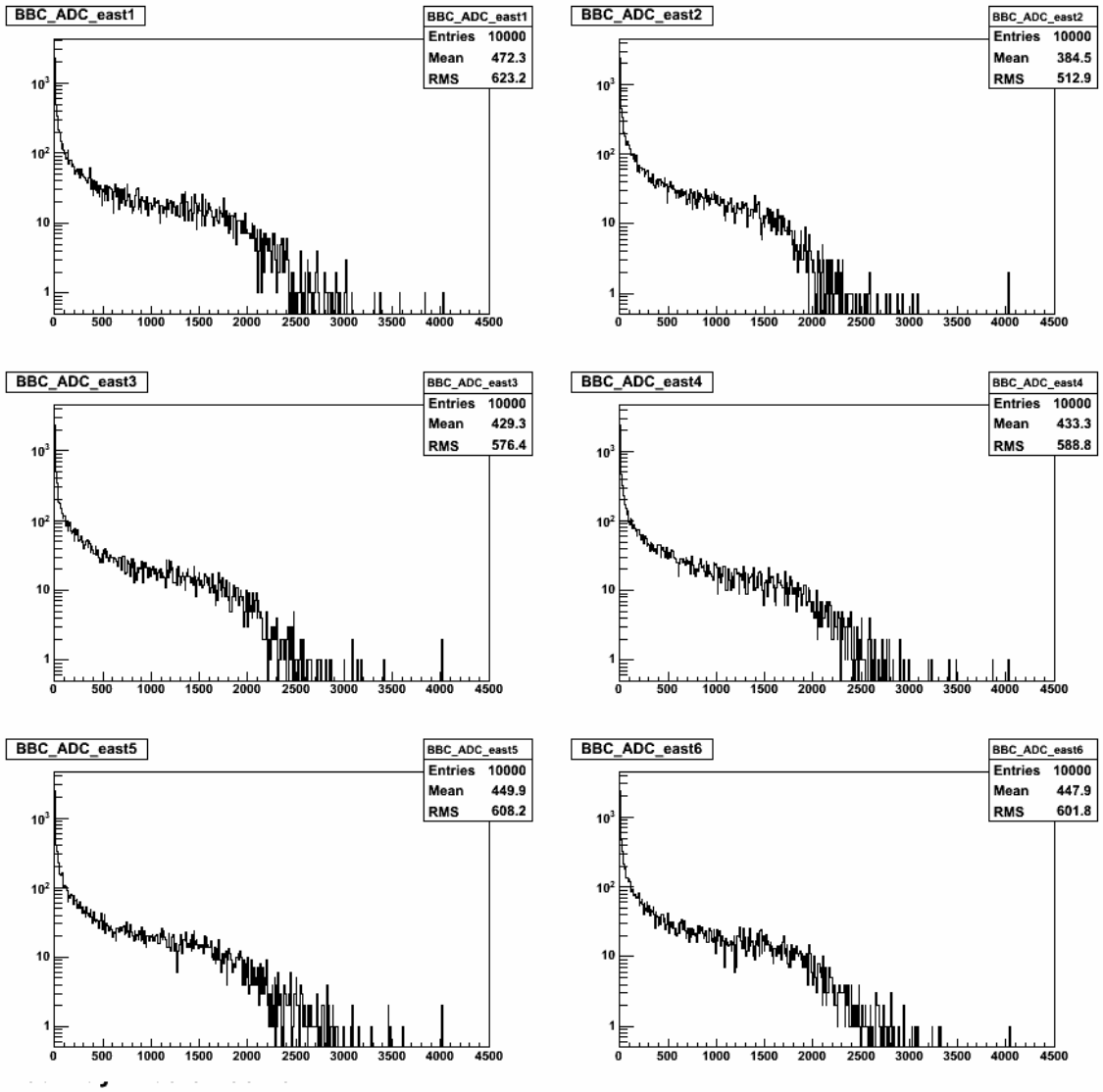

Figure 4.4: East ADC distribution for the first inner ring of BBC. These are online monitoring plots from 39 GeV AuAu collisions during data taking in 2010 and no trigger selection was made.

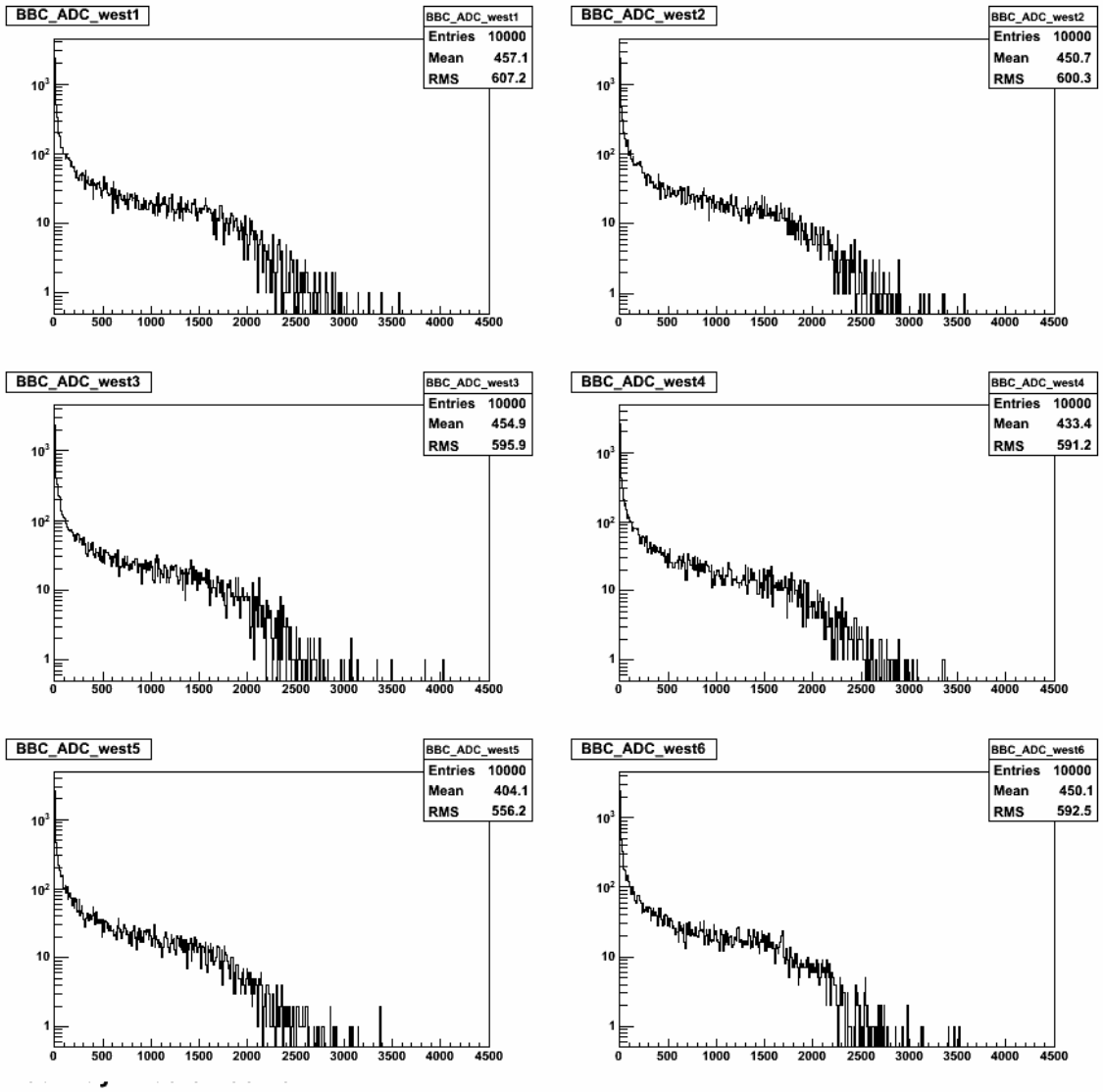

Figure 4.5: West ADC distribution for the first inner ring of BBC. These are online monitoring plots from 39 GeV AuAu collisions during data taking in 2010 and no trigger selection was made.

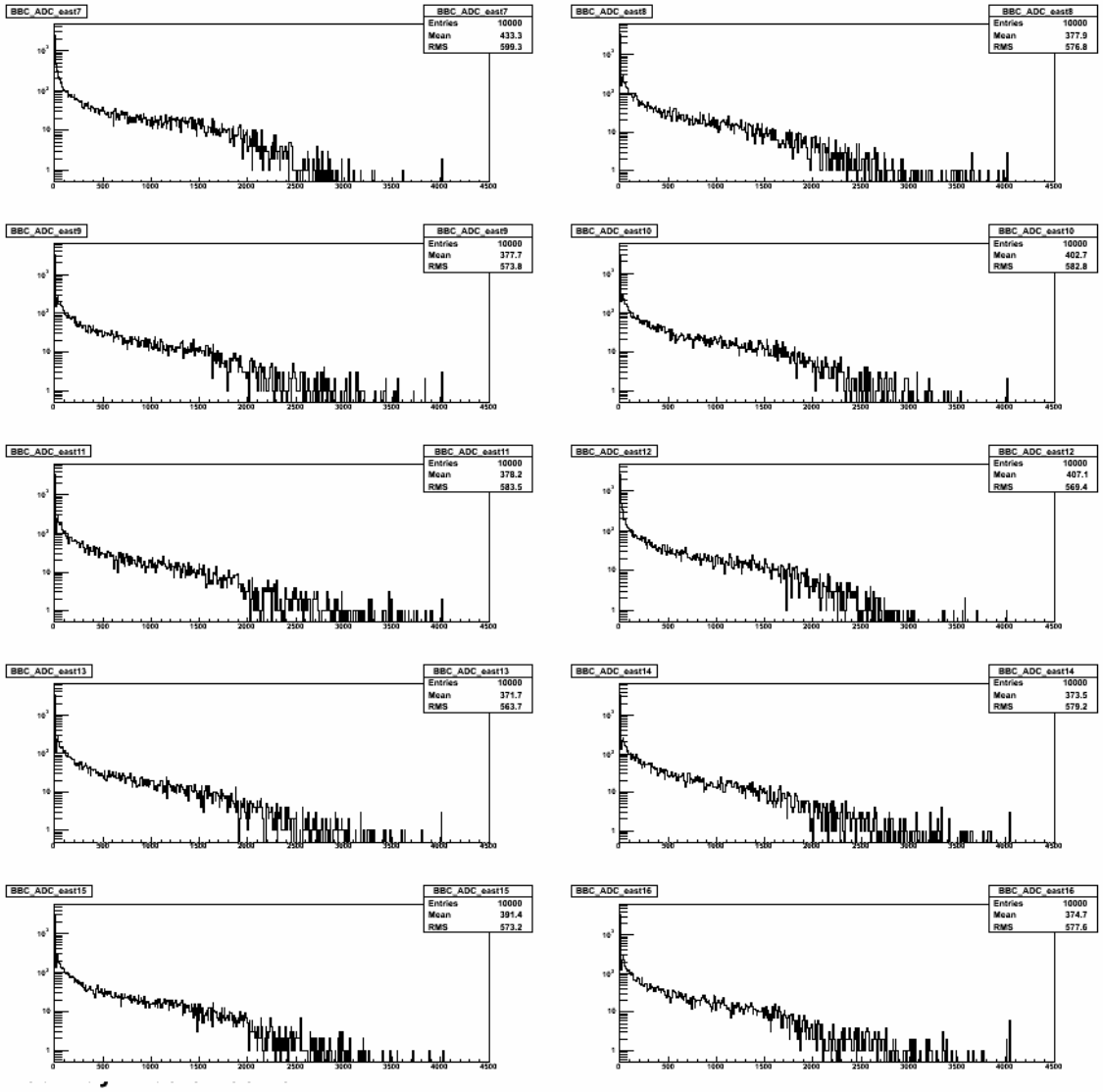

Figure 4.6: East ADC distribution for the second inner ring of BBC. These are online monitoring plots from 39 GeV AuAu collisions during data taking in 2010 and no trigger selection was made.

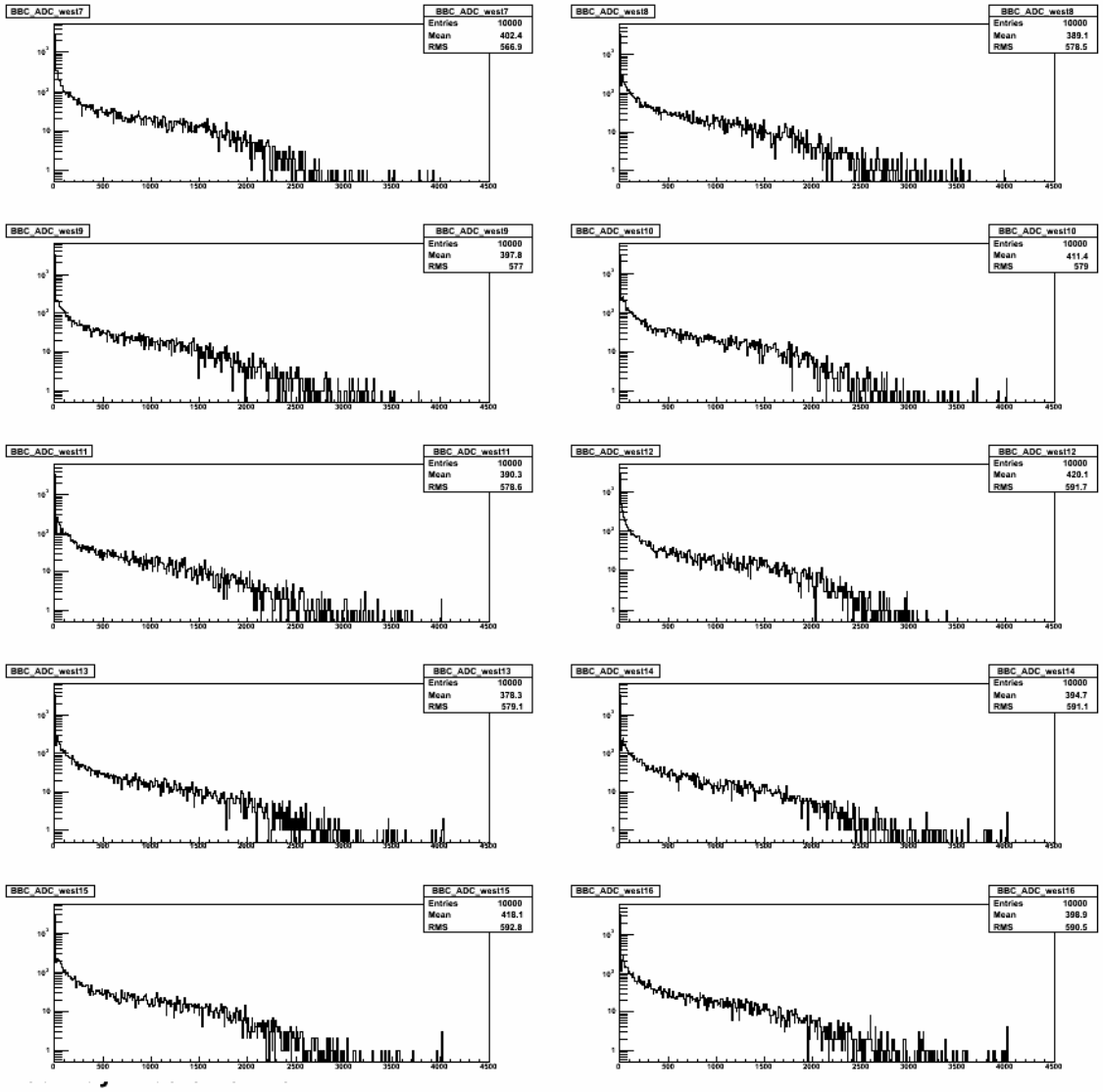

Figure 4.7: West ADC distribution for the second inner ring of BBC. These are online monitoring plots from 39 GeV AuAu collisions during data taking in 2010 and no trigger selection was made

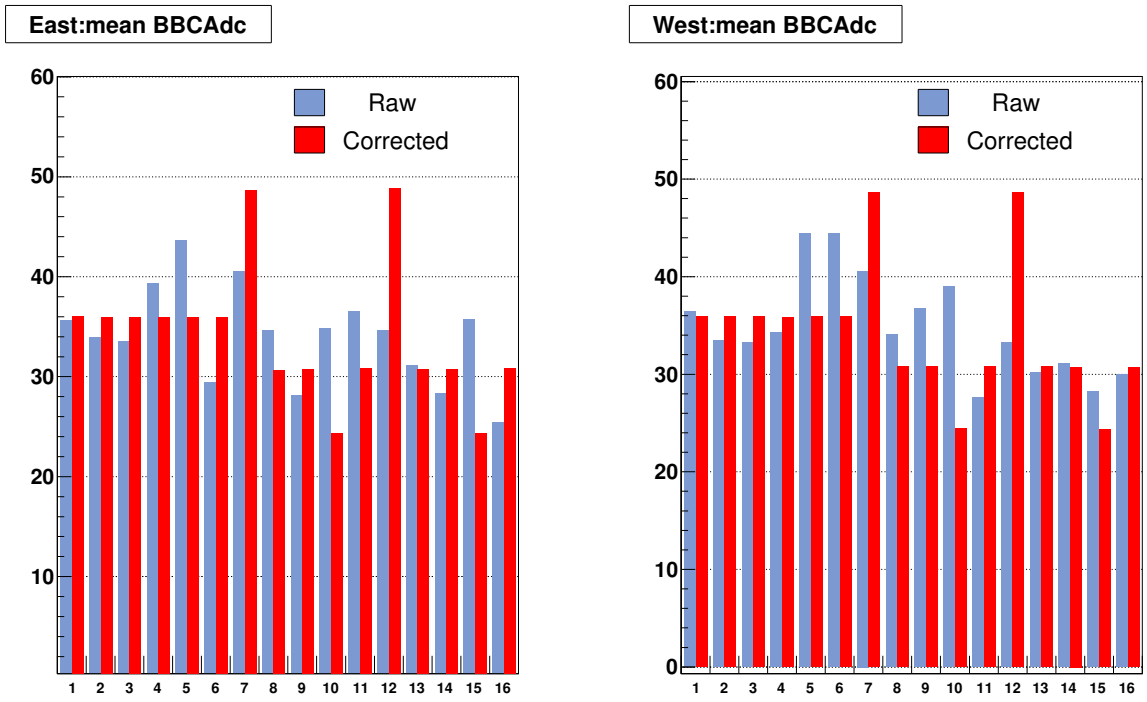

Figure 4.8: Mean channel-by-channel east and west ADC distributions before and after gain correction. This plot is from 22.4 GeV CuCu collisions for 20-30% central collisions.

Recentering Correction

The recentering correction [71] is one of the popular methods to make an event plane distribution flat. In this method, from each event's Q-vector one subtracts the Q-vector averaged over many events.

$$Q'_{nx} = Q_{nx} - \langle Q_{nx} \rangle$$
$$Q'_{ny} = Q_{ny} - \langle Q_{ny} \rangle \tag{4.17}$$

This method helps to correct for detector inefficiencies due to bad connections, or dead sectors, etc. In many cases, this method alone is not sufficient to produce a flat distribution. Most of the time, this method is combined with another method (see below).

Ψ Weight Method

One of the methods to make the event plane distribution flat is to apply weights to events with different event plane angles. The weight can be determined with the inverse of the bin content in the raw event plane distribution, so that the events with more probable event plane angles get less weight, and vice versa.

When the event plane is reconstructed in track-based detector e.g. TPC/FTPC, this method with ϕ weight can be used to make event plane distribution flat [72].

Shift Correction Method

Another method to make corrections to the event plane angle is the shift correction method [73] in which we apply a correction to the event plane angle itself, and flatten the event plane distribution. The raw event plane distribution $\frac{dN}{d\Psi}$

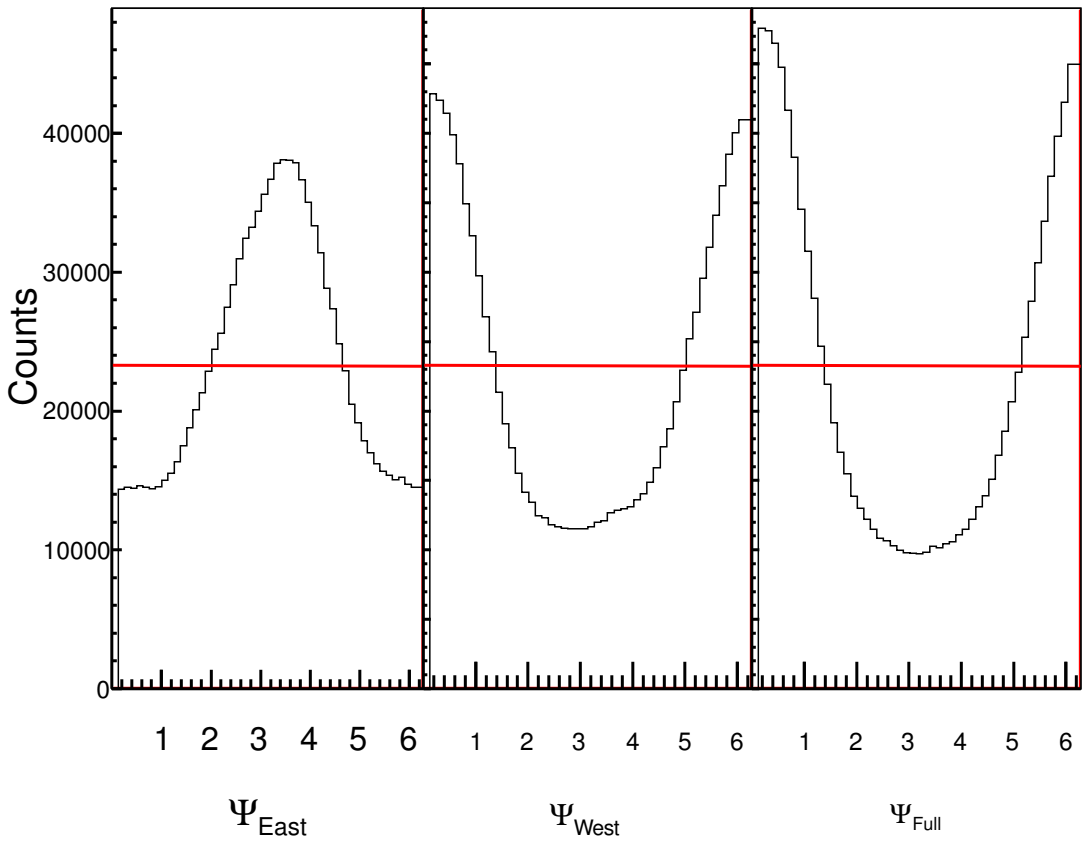

Figure 4.9: First-order event plane distribution for east, west and full event plane. The Ψ weight method is applied to force the event plane distribution to become flat, as represented by the horizontal red line.

can be expanded in a Fourier series

$$\frac{dN}{d\Psi} = \frac{a_0}{2} + \sum_n (a_n \cos n\Psi + b_n \sin n\Psi) \tag{4.18}$$

where

$$a_n = \frac{1}{\pi}\int_{-\pi}^{\pi} \frac{dN}{d\Psi} \cos n\Psi d\Psi \qquad n = 0, 1, 2, ... \tag{4.19}$$

$$b_n = \frac{1}{\pi}\int_{-\pi}^{\pi} \frac{dN}{d\Psi} \sin n\Psi d\Psi \qquad n = 1, 2, 3, ...$$

We make a new angle $\Psi^{'}$ after adding a correction term $\Delta\Psi$ to the raw event plane angle Ψ

$$\Psi^{'} = \Psi + \Delta\Psi = \Psi + \sum_{n}(A_n \cos n\Psi + B_n \sin n\Psi) \tag{4.20}$$

By requiring the new angle to be uniformly distributed, we have

$$\frac{dN}{d\Psi^{'}} = \frac{N}{2\pi} = \frac{a_0}{2} \tag{4.21}$$

Now, we can write the new raw distribution as

$$\frac{dN}{d\Psi} = \frac{dN}{d\Psi^{'}}\frac{d\Psi^{'}}{d\Psi} = \frac{a_0}{2}[1 + \sum(-nA_n \sin n\Psi + nB_n \cos n\Psi)] \tag{4.22}$$

Comparing equations 4.18 and 4.22, we can evaluate the coefficients from the raw distribution,

$$\begin{aligned} A_n &= -\tfrac{2}{n}\tfrac{b_n}{a_0} = -\tfrac{2}{n}\langle \sin n\Psi \rangle \\ B_n &= \tfrac{2}{n}\tfrac{a_n}{a_0} = \tfrac{2}{n}\langle \cos n\Psi \rangle \end{aligned} \tag{4.23}$$

Thus the corrected event plane angle is

$$\Psi^{'} = \Psi + \sum_{n}\frac{1}{n}[-\langle \sin 2n\Psi \rangle \cos 2n\Psi + \langle \cos 2n\Psi \rangle \sin 2n\Psi] \tag{4.24}$$

In practice, we flatten the event plane distribution up to the twentieth harmonic ($n = 20$) as shown in Fig. 4.10. It can also be shown that the same flattening procedure removes possible trigger biases (due to imperfect calibrations, dead channels, or any other asymmetry) at least up to the second order [70].

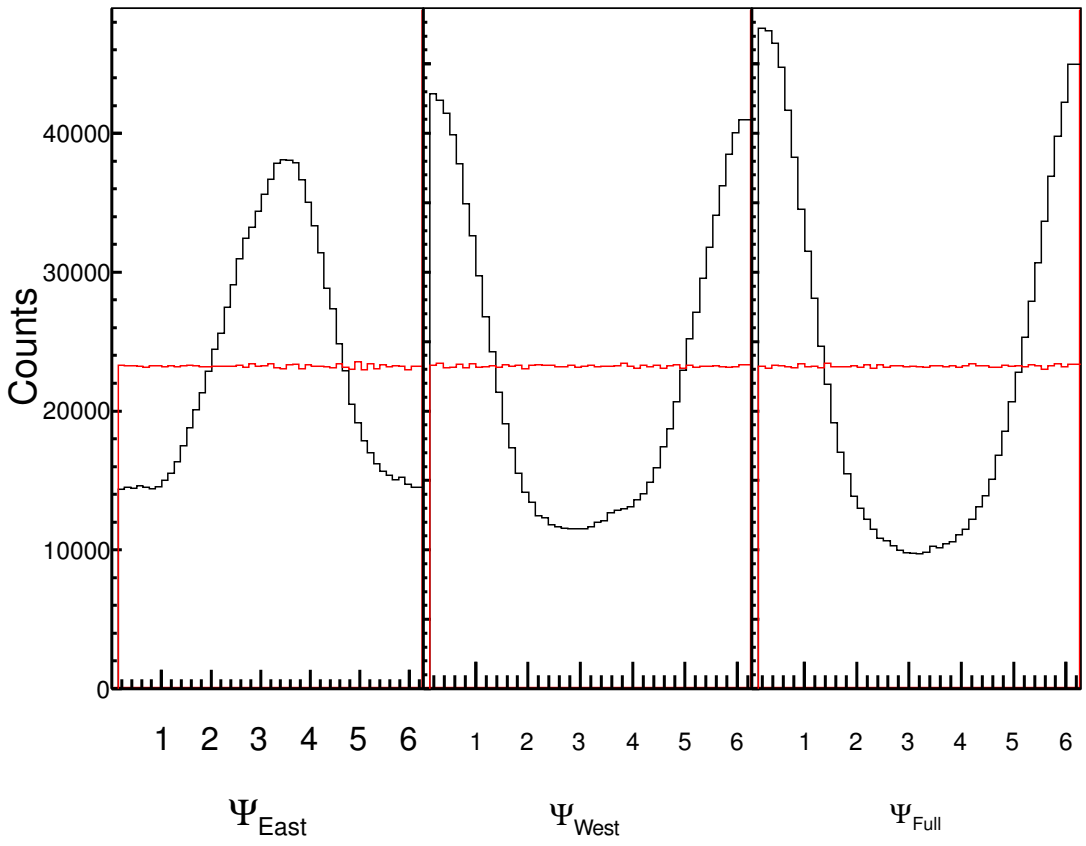

Figure 4.10: First-order event plane distribution for east, west and full event plane. The shift correction forces the event plane distribution to became flat.

4.2.7 Event Plane Resolution

Since finite multiplicity limits the angular resolution of the reaction plane reconstruction, the $v_n^{\rm obs}$ has to be corrected for the event plane resolution to obtain the real v_n,

$$v_n = \frac{v_n^{\rm obs}}{\langle \cos n(\Psi_n - \Psi_r) \rangle} \tag{4.25}$$

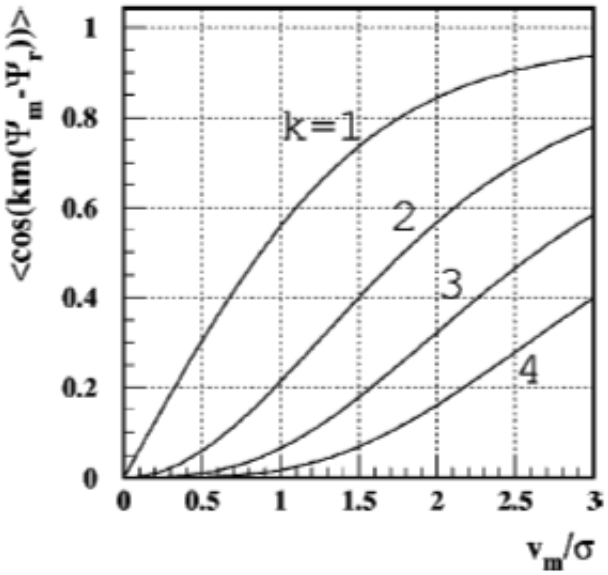

Figure 4.11: The event plane resolution for the nth $(n = km)$ harmonic of a particle distribution with respect to the mth harmonic plane, as a function of $\chi_m = v_m/\sigma$. This plot is from Ref. [14].

where angle brackets denote an average over a large event sample. The event plane resolution is the denominator of the above equation. For the case of the 1st-order event plane from the BBC, $m = 1$ and the event plane resolution for the k-th harmonic calculation reduces to $\langle \cos k(\Psi_1 - \Psi_r) \rangle$. The BBC event plane obtained from the detector on one side of the collision (east or west) is called a sub-event plane. We have two independent sub-event planes from the two BBCs. The correlation between these two event plane angles can be expressed as

$$\langle \cos k(\Psi_{\text{east}} - \Psi_{\text{west}}) \rangle \;\; = \langle \cos k(\Psi_{\text{east}} - \Psi_r) \rangle \;\; \langle \cos k(\Psi_{\text{west}} - \Psi_r) \rangle \tag{4.26}$$

If we assume that the two sub-event planes have the same resolution, then the

sub-event plane resolution is

$$\begin{aligned} \langle \cos k(\Psi_{\rm sub} - \Psi_r) \rangle &= \langle \cos k(\Psi_{\rm east} - \Psi_r) \rangle \\ &= \langle \cos k(\Psi_{\rm west} - \Psi_r) \rangle \\ &= \sqrt{\langle \cos k(\Psi_{\rm east} - \Psi_{\rm west}) \rangle} \end{aligned} \tag{4.27}$$

The term inside the square-root should always be positive, if the sub-events are correlated. However, for small amounts of flow, fluctuations and/or nonflow correlations can cause this term to be negative. A combination of the east and west sub-event plane vectors provides the full event plane. When the sub-event plane resolution is low, we can approximate the full event plane resolution as

$$\langle \cos k(\Psi_{\rm full} - \Psi_r) \rangle \approx \sqrt{2} \langle \cos k(\Psi_{\rm sub} - \Psi_r) \rangle \tag{4.28}$$

which can be obtained from the sub-event plane resolution. A more detailed and accurate estimation of the event plane resolution from Ref. [14] is given by

$$\langle \cos km(\Psi_m - \Psi_r) \rangle = \frac{\sqrt{\pi}}{2\sqrt{2}} \chi_m \exp(-\chi_m^2/4)[I_{(k-1)/2}(\chi_m^2/4) + I_{(k+1)/2}(\chi_m^2/4)] \tag{4.29}$$

where $\chi_m = v_m/\sigma$ and I_ν is the modified Bessel function of order ν. This resolution function is plotted in 4.11. In the event plane resolution calculation used in this dissertation, Eq. 4.29 has been used.

Figure 4.12 (left panel) shows the resolution of the 1st-order full event plane (R_{11}) provided by the BBCs, as determined from the sub-event correlation between east and west BBCs. The right panel shows the resolution correction (R_{12}) for elliptic flow measurement using the first-order BBC event plane.

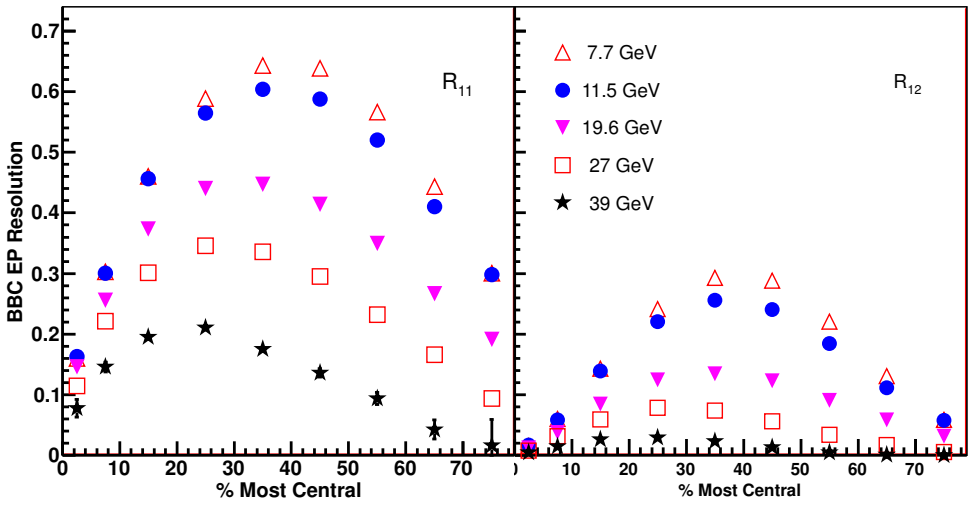

Figure 4.12: The left panel shows the first-order BBC resolution from the sub-event correlation between east and west BBCs. The right panel shows the resolution correction for elliptic flow measurement using the first-order BBC event plane. The BBC EP resolution is plotted as a function of centrality and for different beam energies.

4.3 Directed Flow Measurement

We utilized the first-order event plane reconstructed using BBC signals to measure directed flow for all beam energies presented here. We also used the FTPC event plane method for this measurement in 9.2 GeV AuAu collisions. At $\sqrt{s}_{NN}$ =7.7, 11.5, 19.6, 27 and 39 GeV, only a small fraction of data sets have FTPC information, and therefore the FTPC event plane method is used only for systematic error estimation.

4.3.1 BBC Event Plane Method

The full BBC event plane is used to measure directed flow (v_1) for TPC tracks ($|\eta| < 1.0$)

$$v_1\{\mathrm{BBC}\} = \frac{\langle\cos(\phi - \Psi_{\mathrm{BBC}})\rangle}{\mathrm{C}\sqrt{\langle\cos(\Psi_{\mathrm{BBC}_{\eta_-}} - \Psi_{\mathrm{BBC}_{\eta_+}})\rangle}} \tag{4.30}$$

The denominator in Eq. (4.30) represents the full BBC event plane resolution. We use subevents reconstructed in opposite pseudorapidity regions for FTPC tracks $(2.5 < |\eta| < 4.2)$,

$$v_1\{\mathrm{BBC}_{\eta_-}\} = \frac{\langle\cos(\phi - \Psi_{\mathrm{BBC}_{\eta_+}})\rangle}{\sqrt{\langle\cos(\Psi_{\mathrm{BBC}_{\eta_-}} - \Psi_{\mathrm{BBC}_{\eta_+}})\rangle}} \tag{4.31}$$

$$v_1\{\mathrm{BBC}_{\eta_+}\} = \frac{\langle\cos(\phi - \Psi_{\mathrm{BBC}_{\eta_-}})\rangle}{\sqrt{\langle\cos(\Psi_{\mathrm{BBC}_{\eta_-}} - \Psi_{\mathrm{BBC}_{\eta_+}})\rangle}} \tag{4.32}$$

This method effectively avoids self-correlation because of partial overlap between FTPC and BBC coverage.

4.3.2 FTPC Event Plane Method

For the TPC coverage $(|\eta| < 1)$ we use the full FTPC event plane,

$$v_1\{\mathrm{FTPC}\} = \frac{\langle\cos(\phi - \Psi_{\mathrm{FTPC}})\rangle}{\mathrm{C}\sqrt{\langle\cos(\Psi_{\mathrm{FTPC}_{\eta_-}} - \Psi_{\mathrm{FTPC}_{\eta_+}})\rangle}} \tag{4.33}$$

The denominator in Eq. (4.50) represents the full FTPC event plane resolution. We use subevents reconstructed in opposite pseudorapidity regions for FTPC tracks $(2.5 < |\eta| < 4.2)$,

$$v_1\{\mathrm{FTPC}_{\eta_-}\} = \frac{\langle\cos(\phi - \Psi_{\mathrm{FTPC}_{\eta_+}})\rangle}{\sqrt{\langle\cos(\Psi_{\mathrm{FTPC}_{\eta_-}} - \Psi_{\mathrm{FTPC}_{\eta_+}})\rangle}} \tag{4.34}$$

$$v_1\{\mathrm{FTPC}_{\eta_+}\} = \frac{\langle\cos(\phi - \Psi_{\mathrm{FTPC}_{\eta_-}})\rangle}{\sqrt{\langle\cos(\Psi_{\mathrm{FTPC}_{\eta_-}} - \Psi_{\mathrm{FTPC}_{\eta_+}})\rangle}} \tag{4.35}$$

This method avoids self-correlation.

4.4 Elliptic Flow Measurement

The first order event plane reconstructed using BBC signals is used to measure elliptic flow for AuAu collisions at $\sqrt{s}_{NN}$ = 7.7, 11.5, 19.6, 27 and 39 GeV. The BBC event plane resolution for v_2 measurement for CuCu collision at 22.4 GeV data set is very poor [74]. Therefore, the second-order event plane reconstructed from the TPC is used to measure v_2 for this data set.

4.4.1 BBC Event Plane Method

In this method, the elliptic flow v_2 is obtained correlating the particles with the first order BBC event plane.

$$v_2\{\mathrm{BBC}\} = \frac{\langle \cos 2(\phi - \Psi_{\mathrm{BBC}}) \rangle}{\mathrm{R}_{12}} \tag{4.36}$$

where R_{12} is the event plane resolution for $n = 2$ $(m = 1,\ k = 2)$, when v_2 is measured with respect to the first-order event plane.

4.4.2 TPC Event Plane Method

In this method, v_2 is measured with respect to the second-order event plane reconstructed using the TPC tracks. In event plane calculations, tracks have a weighting factor $w = p_T$ in units of GeV/c for $p_T < 2$ GeV/c, and $w = 2$ GeV/c for $p_T \geq$ GeV/c. The η sub-event method is used where one defines the flow vector for each particle based on particles measured in the opposite hemisphere in pseudorapidity:

$$v_2\{\mathrm{EtaSubs}\} = \frac{\langle \cos 2(\phi_{\pm} - \Psi_{2,\eta_{\mp}}) \rangle}{\sqrt{\langle \cos 2(\Psi_{2,\eta_+} - \Psi_{2,\eta_-}) \rangle}} \tag{4.37}$$

Here $v_2\{\mathrm{EtaSubs}\}$ denotes the results of the η sub-event method, and $\Psi_{2,\eta_+}(\Psi_{2,\eta_+})$

is the second harmonic event plane angle determined by particles with positive/negative pseudorapidity. A small additional η gap is used between negative/positive η sub-events to suppress non-flow effects.

4.4.3 The Cumulant Method

The Q-cumulants method [75], also sometimes called the direct cumulant method, calculates cumulants without using nested loops over tracks. The cumulants are expressed in terms of the moments of the magnitude of the corresponding flow vector,

$$Q_n \equiv \sum_{i=1}^{M} e^{in\phi_i} \tag{4.38}$$

The single-event average two- and four-particle azimuthal correlations can be then formulated as [75]:

$$\langle 2 \rangle = \frac{|Q_n|^2 - M}{M(M-1)} \tag{4.39}$$

$$\begin{aligned} \langle 4 \rangle =& \frac{|Q_n|^4 + |Q_{2n}|^2 - 2\Re\left[Q_{2n}Q_n^* Q_n^*\right]}{M(M-1)(M-2)(M-3)} \\ & - 2\frac{2(M-2)|Q_n|^2 - M(M-3)}{M(M-1)(M-2)(M-3)} \end{aligned} \tag{4.40}$$

The average over all events can be performed as:

$$\begin{aligned} \langle\langle 2 \rangle\rangle &\equiv \langle e^{in(\phi_1 - \phi_2)} \rangle \\ &= \frac{\sum_{\text{event}} \left(W_{\langle 2 \rangle}\right)_i \langle 2 \rangle_i}{\sum_{\text{event}} \left(W_{\langle 2 \rangle}\right)_i} \end{aligned} \tag{4.41}$$

$$\begin{aligned} \langle\langle 4 \rangle\rangle &\equiv \langle e^{in(\phi_1 + \phi_2 - \phi_3 - \phi_4)} \rangle \\ &= \frac{\sum_{\text{events}} \left(W_{\langle 4 \rangle}\right)_i \langle 4 \rangle_i}{\sum_{\text{events}} \left(W_{\langle 4 \rangle}\right)_i} \end{aligned} \tag{4.42}$$

while the weights are the number of two- and four-particle combinations:

$$W_{\langle 2 \rangle} \equiv M(M-1), \tag{4.43}$$

$$W_{\langle 4\rangle} \equiv M(M-1)(M-2)(M-3). \tag{4.44}$$

Choosing the multiplicity weights above can make the final multi-particle azimuthal correlations free of multiplicity fluctuations [76]. However, one can also use unit weights treating events with different multiplicity equally. The two- and four-particle cumulants without detector bias can be formulated as:

$$c_n\{2\} = \langle\langle 2\rangle\rangle \tag{4.45}$$

$$c_n\{4\} = \langle\langle 4\rangle\rangle - 2\langle\langle 2\rangle\rangle^2 \tag{4.46}$$

The integrated flow (e.g. integrated over p_T and η) can be estimated both from two- and four-particle cumulants:

$$v_n\{2\} = \sqrt{c_n\{2\}} \tag{4.47}$$

$$v_n\{4\} = \sqrt[4]{-c_n\{4\}} \tag{4.48}$$

In this method, the higher order multi-particle correlation formalism removes the contribution of non-flow correlations from lower order correlations [75, 76].

4.5 Triangular Flow Measurement

There are various methods to obtain triangular flow results. Two-particle correlations which are sensitive to non-flow correlations and multiparticle correlations which are less sensitive to the non-flow correlations along with event plane methods have been extensively used in elliptic flow measurements for past couple of decades. These methods used in elliptic flow analysis can be extended to measure triangular flow. The event plane method, and the two-particle cumulant method, which are used in v_3 analysis for this dissertation, are discussed below.

4.5.1 Event Plane Methods

In the standard event plane method [14] for v_3, we reconstruct a third-harmonic event plane from TPC tracks and also from FTPC tracks. In event plane calculations, tracks have a weighting factor $w = p_T$ in units of GeV/c for $p_T < 2$ GeV/c, and $w = 2$ GeV/c for $p_T \geq 2$ GeV/c. Although the STAR detector has good azimuthal symmetry, small acceptance effects in the calculation of the event plane azimuth were removed by the method of shifting [73]. When using the TPC event plane, we used the η sub-event method with an additional η gap of $\pm$ 0.05.

$$v_3\{\mathrm{EtaSubs}\} = \frac{\langle \cos 3(\phi_\pm - \Psi_{3,\eta_\mp})\rangle}{\sqrt{\langle \cos 3(\Psi_{3,\eta_+} - \Psi_{3,\eta_-})\rangle}} \tag{4.49}$$

This avoids self-correlations because the particles and the event plane are in opposite hemispheres. When using the FTPCs, we used the full event plane from both FTPCs [14].

$$v_3\{\mathrm{FTPC}\} = \frac{\langle \cos 3(\phi - \Psi_{3\mathrm{FTPC}})\rangle}{\mathrm{C}\sqrt{\langle \cos 3(\Psi_{3,\mathrm{FTPC}\eta_+} - \Psi_{3,\mathrm{FTPC}\eta_-})\rangle}} \tag{4.50}$$

This introduced a large η gap between the particles and the event plane. Since there is no overlap between the coverage of the TPC and FTPCs, there is no possibility of self-correlation when using the FTPC event plane.

4.5.2 Two-Particle Correlation Method

I study $\langle \cos 3(\phi_j - \phi_i)\rangle_{i\neq j}$ vs $\Delta\eta$ between two particles with indices i and j to understand the $\Delta\eta$ dependence of the triangular flow signal and to distinguish among different sources of non-flow correlations. This distribution of $\langle \cos 3(\phi_j - \phi_i)\rangle_{i\neq j}$ vs. $\Delta\eta$ can be well described by wide and narrow Gaussian peaks as shown in Fig. 4.13 for two centrality intervals. The narrow Gaussian is identified with

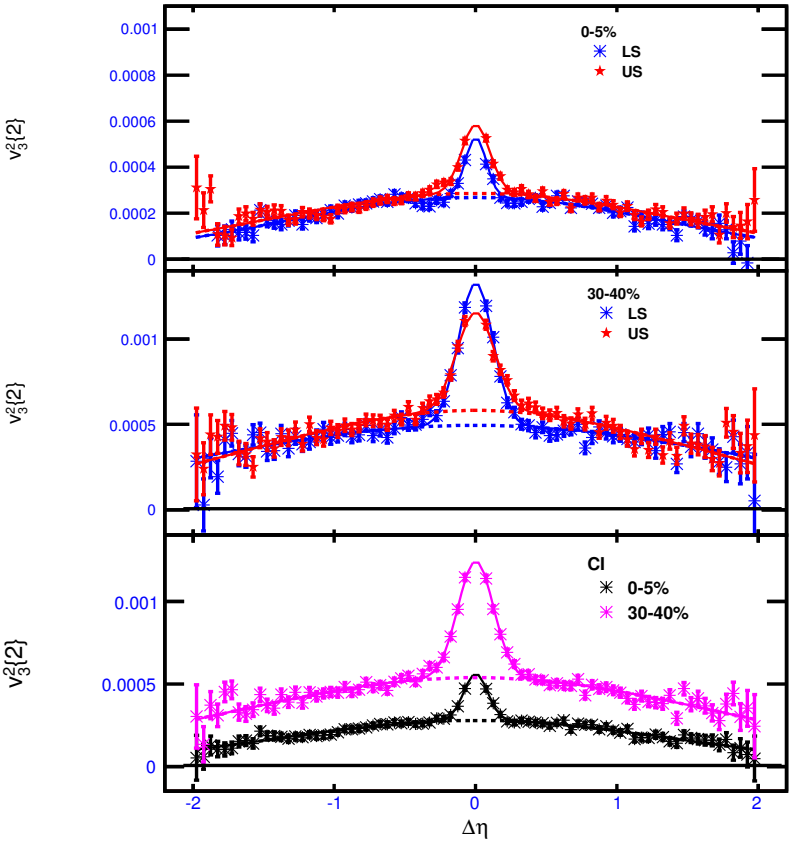

Figure 4.13: $v_3^2\{2, \Delta\eta\}$ vs. $\Delta\eta$ for charged hadrons within two centrality intervals in 200 GeV Au+Au collisions. Data are fit with narrow and wide Gaussians. Like Sign, Unlike Sign, and Charge Independent cases are shown.

short range non-flow correlations like Bose-Einstein correlations, resonance decay, Coulomb interactions, and effects from track merging. The narrow peak disappears above $p_T \geq 0.8$ GeV/c so it is unlikely to be from jet correlations. The wide Gaussian represented by $v_3^2\{2, \Delta\eta\}$ is the signal of interest and its fit parameters are used to calculate $v_3^2\{2\}$ as a function of centrality and transverse momentum. For v_3 integrated over p_T and η we have

$$v_3^2\{2\} = \frac{\int_a^b v_3^2\{2, \Delta\eta\} W d(\Delta\eta)}{\int_a^b W d(\Delta\eta)}, \tag{4.51}$$

where W equals $dN/d(\Delta\eta)$ when weighted with the number of particle pairs or 1 for unit weight. The quantity $v_3\{2\}(p_T)$ can be obtained from the scalar product [77] relation

$$v_3\{2\}(p_T) = \frac{\langle \cos 3(\phi_j - \phi_i) \rangle_{i \neq j}}{\sqrt{\langle v_3^2\{2\} \rangle}}, \tag{4.52}$$

where the j^{th} particle is selected from the p_T bin of interest.

4.6 Flow Harmonic Associated with Dipole Asymmetry

We used the analysis method proposed by Luzum and Ollitrault [44]. This method proposes measurement of the signal with a modified event vector in such a way that it automatically corrects for the effect of momentum conservation [78] and also cancels out the conventional directed flow which is an odd function of rapidity. The event plane vector is reconstructed from tracks within $|\eta| < 1.0$. We use η subevents which are reconstructed from $-1.0 < \eta < -0.05$ and $0.05 < \eta < 1.0$. This introduces a small gap of 0.1 units between the two subevents and at least a gap of 0.05 units with correlating particles, which helps to suppress very short range correlations.

Centrality	$\langle p_T \rangle$	$\langle p_T^2 \rangle$
0-5%	0.580164	0.46723
5-10%	0.577256	0.463626
10-20%	0.573615	0.458983
20-30%	0.567932	0.451075
30-40%	0.560834	0.440691
40-50%	0.552273	0.42794
50-60%	0.542049	0.412661
60-70%	0.530669	0.395693
70-80%	0.518538	0.377593

Table 4-4: Mean p_T and mean p_T^2 for various centralities in 200 GeV Au+Au collisions. This is for $0.15 < p_T < 2.0$ GeV/c and $|\eta| < 1.0$.

$$Q_x = \sum_i w_i \cos n\phi_i, \tag{4.53}$$

$$Q_y = \sum_i w_i \sin n\phi_i \tag{4.54}$$

where weight is taken as

$$w_i = p_T - \frac{\langle p_T^2 \rangle}{\langle p_T \rangle}. \tag{4.55}$$

The choice of this weight removes the correlation due to momentum conservation and also it cancels the conventional directed flow. We evaluated the values of $\langle p_T \rangle$ and $\langle p_T^2 \rangle$ from the full data set for each centrality bin, as shown in Table 4-4. In order to remove acceptance effects, we applied a re-centering correction to the flow vectors.

Two variations of the event plane method are used, i.e., the scalar-product method [77] and the standard event plane method with η subevents.

4.6.1 Scalar Product Method

In this method, the signal of interest is v_1, and is evaluated using

$$v_1(\eta > 0) \;\; = \frac{\langle Q_a(\eta < 0).u_i)\rangle}{\sqrt{\langle Q_a.Q_b\rangle}} \tag{4.56}$$

$$v_1(\eta < 0) \;\; = \frac{\langle Q_b(\eta > 0).u_i)\rangle}{\sqrt{\langle Q_a.Q_b\rangle}} \tag{4.57}$$

where $u_i = e^{i\phi}$ is the unit vector of a particle. The vectors Q_a and Q_b are constructed from the subevents $a(\eta < 0)$ and $b(\eta > 0)$.

This subevent method effectively removes the self-correlation.

4.6.2 Event Plane method

In the event plane method, we first evaluate the event plane azimuth Ψ_1 from the event plane vector:

$$\Psi_n = \left(\tan^{-1}\frac{Q_y}{Q_x}\right) \tag{4.58}$$

Then

$$v_1\{\eta > 0\} \;\; = \frac{\langle \cos \mathrm{n}[\phi - \Psi_\mathrm{a}(\eta < 0)]\rangle}{\sqrt{\langle \cos[\Psi_\mathrm{a}(\eta < 0) - \Psi_\mathrm{b}(\eta > 0)]\rangle}}. \tag{4.59}$$

$$v_1\{\eta < 0\} \;\; = \frac{\langle \cos \mathrm{n}[\phi - \Psi_\mathrm{b}(\eta > 0)]\rangle}{\sqrt{\langle \cos[\Psi_\mathrm{a}(\eta < 0) - \Psi_\mathrm{b}(\eta > 0)]\rangle}}. \tag{4.60}$$

Use of the subevent plane method removes the effect from self correlation.

4.7 Systematic Uncertainties

In this section, various possible sources of systematic uncertainties and their estimation are discussed.

4.7.1 Event Plane Determination

The event plane resolution depends on the number of tracks used to reconstruct the event plane. Therefore changing event and track cuts obviously changes the event plane resolution. Therefore we can not use these techniques to estimate the systematic uncertainty. Instead we changed the flattening technique to estimate the systematic errors in these studies. We used the shifting method to make the event plane flat as the default method. The difference in event plane resolution between the shift method and ψ weight method is our estimate of the systematic error coming from event plane determination. The systematic errors from the flattening process are less than 1% for all event plane methods.

4.7.2 Detector Acceptance and Efficiency

We estimate systematic errors in measurements coming from detector effects by changing event and track quality cuts. We vary the v_z cut, $N_{\rm fit}$ points, DCA, lower and the upper transverse momentum cut. These are the main tests used to estimate the systematic errors. We also changed PID cuts to estimate the error due to particle misidentification.

4.7.3 East-West Symmetry

The STAR detector has east-west symmetry. We compared our results for positive and negative pseudorapidity, positive and negative v_z and the absolute difference is considered to a measure of systematic uncertainty.

4.7.4 Non-Flow Effect

Non-flow [14, 49] refers to the azimuthal correlation which is not related to initial geometry or the reaction plane orientation. There are various sources of non-flow i.e., correlation due to resonances, jets, strings, quantum statistics effects, final-state interactions (particularly Coulomb effects), and momentum conservation. Different methods used to measure anisotropic flow are affected by non-flow in different ways, and are used in this analysis to guide our estimates of contributions to the systematic uncertainty.

A possible systematic error on v_1 can arise from momentum conservation [78] in instances where the event plane is determined from a detector that is not symmetrically deployed on both sides of the beam intersection point. The desired symmetry is present for our v_1 analysis in the region of the central TPC, but is a source of possible concern for the FTPC region. The overlap in acceptance between the BBC and FTPC is only partial in the η region $2.5 < \eta < 3.3$, and therefore it is feasible to compare v_1 using the full BBC event plane with that from one side of the BBC, either east or west. We found that the difference is under 10%, and an extrapolated average correction has been applied to v_1 in the region $\eta > 3.3$.

Momentum conservation effects are suppressed in even harmonics. In our dipole asymmetry measurement, our method of reconstructing the event plane suppresses this correlation. We further estimate it for dipole asymmetry and triangular flow measurement using the full event plane reconstructed from $0.5 < |\eta| < 1.0$ and compare it with η subevent results. The difference is found to be smaller than 2%, within statistical uncertainty.

Chapter 5

RESULTS – I: DIRECTED FLOW

In this chapter, directed flow is presented for all charged particles and for identified charged particles as a function of rapidity and as a function of transverse momentum at different centrality bins for AuAu collisions at $\sqrt{s_{NN}}$ = 7.7, 11.5, 19.6, 27 and 39 GeV. Directed flow is also presented for charged particles as a function of pseudorapidity in 22.4 GeV CuCu collisions and 9.2 GeV AuAu collisions.

5.1 Directed Flow in 7.7, 11.5, 19.6, 27 and 39 GeV AuAu Collisions

Directed flow is presented for all charged particles and identified charged particles as a function of rapidity and as a function of transverse momentum in different centrality bins for the five beam energies studied.

5.1.1 Charged Particles

Figure 5.1 shows the charged hadron v_1 as a function of η at mid rapidity ($|\eta| < 1.0$) and at forward rapidity ($2.5 < |\eta| < 4.2$) for central $(0 - 10\%)$, mid-central $(10 - 40\%)$ and peripheral $(40 - 80\%)$ collisions for Au+Au at $\sqrt{s_{NN}}$ = 7.7, 11.5, 19.6, 27 and 39 GeV. The upper panels of Fig 5.4 also highlight the same result at mid rapidity. The p_T range for this study is $0.2 < p_T < 2.0$ GeV/c. We observe strong centrality dependence of the directed flow as a function of pseudorapidity [80]. A similar observation was reported previously by the STAR

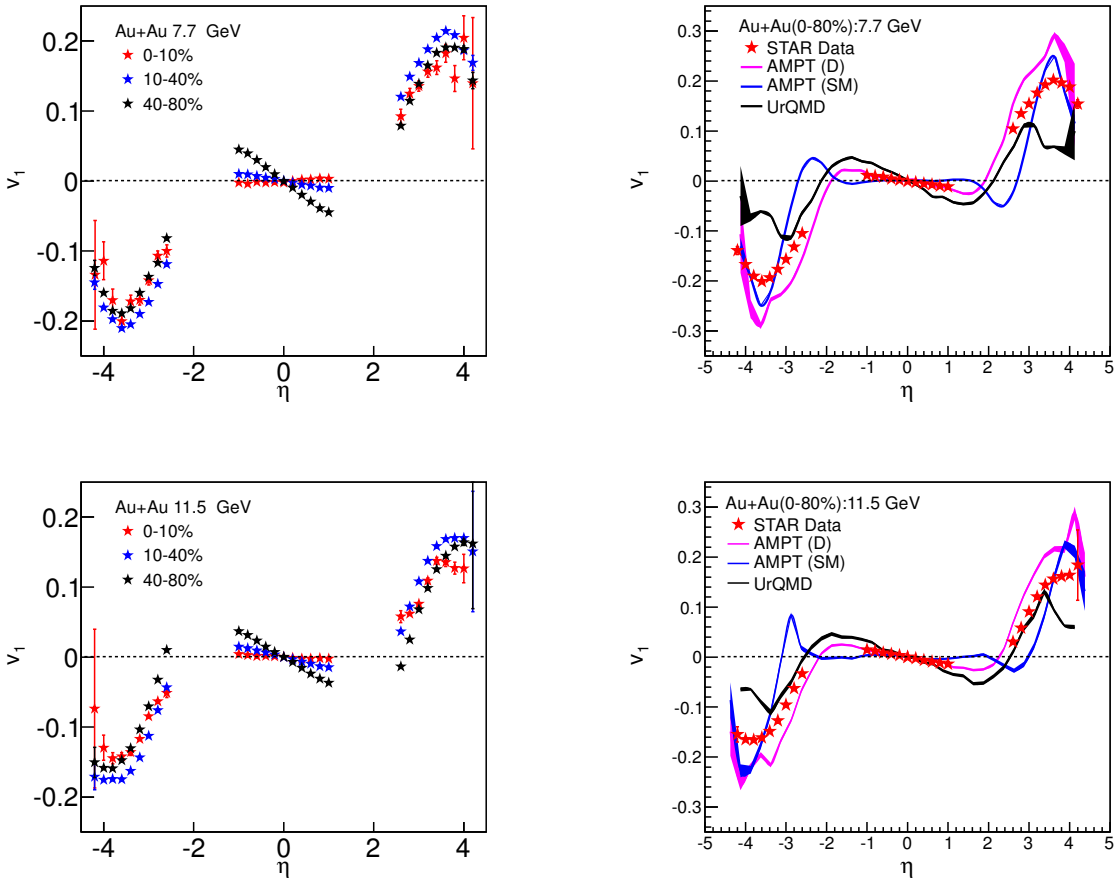

Figure 5.1: Charged hadron v_1 in AuAu collisions at 7.7 and 11.5 GeV as a function of η for central $(0-10\%)$, mid-central $(10-40\%)$ and peripheral $(40-80\%)$ collisions on the left. The panels on the right show the same measurement but for a minimum-bias trigger selection $(0-80\%$ centrality), along with a transport model calculations.

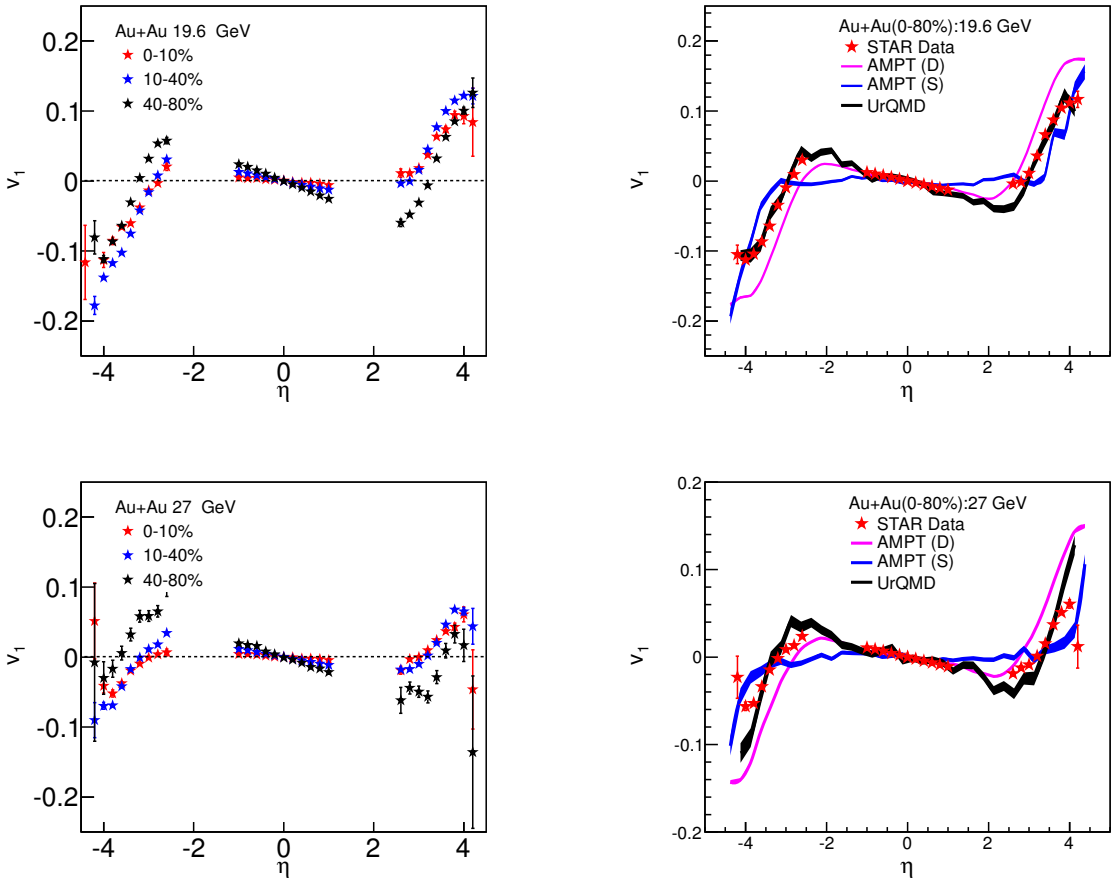

Figure 5.2: Charged hadron v_1 in AuAu collisions at 19.6 and 27 GeV as a function of η for central $(0-10\%)$, mid-central $(10-40\%)$ and peripheral $(40-80\%)$ collisions on the left. The panels on the right show the same measurement but for a minimum-bias trigger selection $(0-80\%$ centrality), along with a transport model calculations.

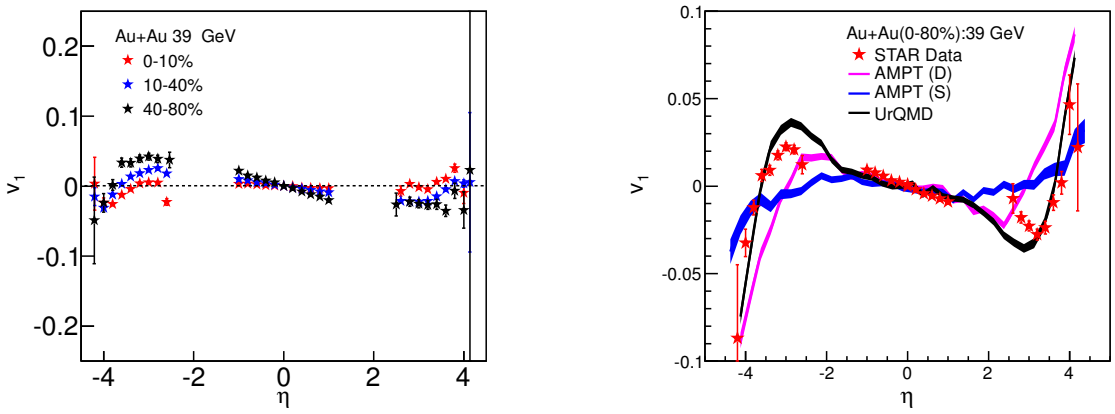

Figure 5.3: Charged hadron v_1 in AuAu collisions at 39 GeV as a function of η for central $(0-10\%)$, mid-central $(10-40\%)$ and peripheral $(40-80\%)$ collisions on the left. The panels on the right show the same measurement but for a minimum-bias trigger selection $(0-80\%$ centrality), along with a transport model calculations.

collaboration at top RHIC energy [35] and by the NA49 Collaboration at SPS energy [40].

In the forward pseudorapidity region, an increasing positive directed flow is observed which saturates at some point and then is observed to drop again whenever there is sufficient pseudorapidity acceptance close to the spectator region, as predicted by many models [81, 82]. The directed flow of spectators is sometimes referred to as the "bounce off" effect [83]. The observed pattern of v_1 near the spectator region is an unremarkable effect predicted by all models, and can readily be explained by a change in the relative abundances of protons and pions at forward pseudorapidities, where proton v_1 and pion v_1 likely have opposite signs, but neither might have a wiggle shape.

The right-hand panels of Fig. 5.1 through Fig. 5.3 show directed flow as a function of η for a minimum-bias trigger selection (0-80% central), along with

transport model calculations. The AMPT calculations were run with both default (D) and "string melting" (S) switch settings [53]. The tested models predict some trends in the data, but they fail to predict the magnitude of the directed flow.

In the bottom panel of Fig 5.4, charged hadron v_1 as a function of p_T for central $(0-10\%)$, mid-central $(10-40\%)$ and peripheral $(40-80\%)$ AuAu collisions at $\sqrt{s_{NN}}$ = 7.7, 11.5, 19.6, 27 and 39 GeV is shown. The pseudorapidity range for this study is $|\eta| < 1.0$. We observe centrality dependence with increased directed flow magnitude from central to peripheral collisions.

Figure 5.5 shows charged hadron v_1 integrated in η and p_T as a function of beam energy in the left panel. The results are for 0–5%, 5-10%, 10-20% central Au+Au collisions. The results at 62.4 and 200 GeV were previously reported by STAR [35]. We observe a local minimum of integrated ($0.2 < p_T < 2.0$ GeV/c and $\eta < 1.0$) directed flow above 11.5 GeV. This type of observation has been argued to be of interest in searching for the softest point in the Nuclear Equation of State [81, 84]. However, the mean transverse momentum as a function of beam energy as shown in the right panel of Fig. 5.5 also shows a minimum at the same energy. This minimum in mean transverse momentum is a result of a larger contribution from protons at lower energy and a larger contribution from pions at higher energy. The minimum in directed flow survives when scaled with mean transverse momentum, but this alone cannot exclude the possibility of a connection between them. This is a very interesting observation and identified-particle v_1 with larger statistics may offer the best hope to resolve this puzzle.

Figure 5.6, left panel, shows charged hadron v_1 as a function of η scaled by the respective $y_{\rm beam}$ values for beam energies of 7.7, 11.5, 19.6, 27, 39,

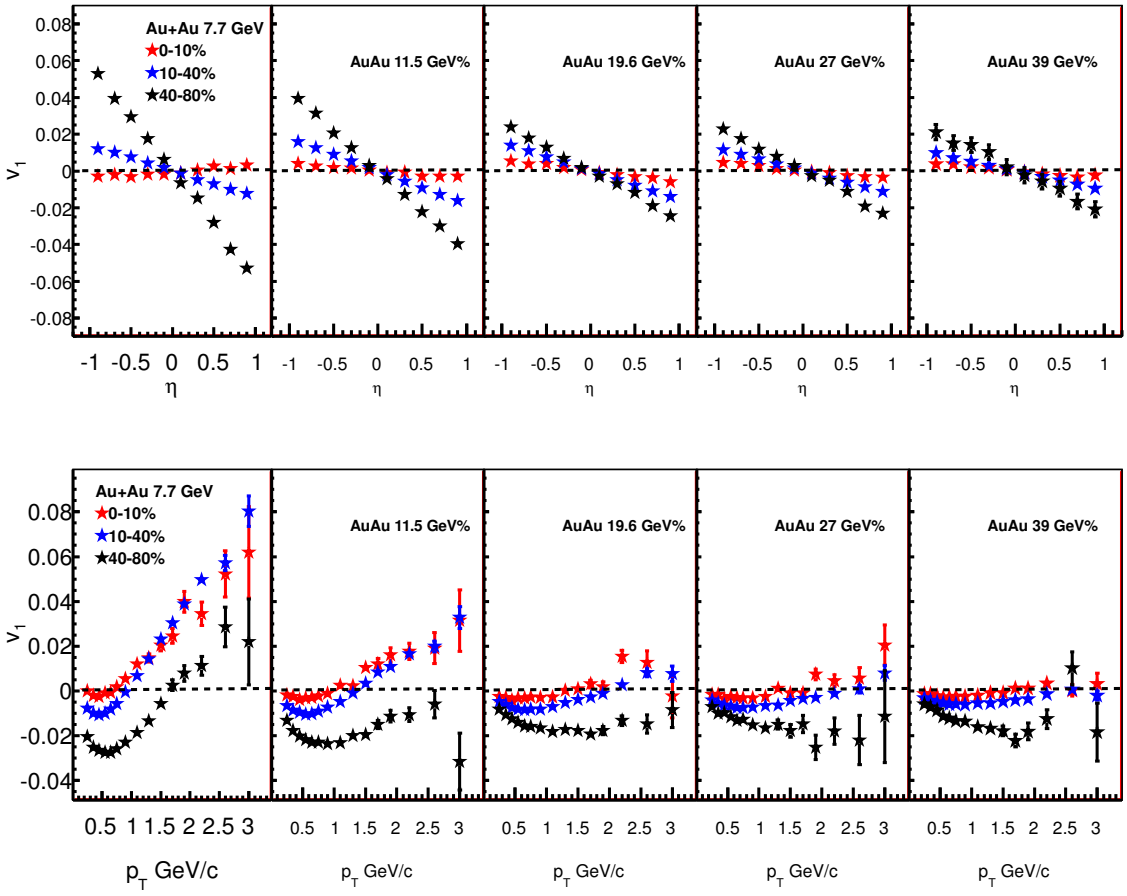

Figure 5.4: Charged hadron v_1 at mid rapidity as a function of η in the top panel for central $(0-10\%)$, mid-central $(10-40\%)$ and peripheral $(40-80\%)$ collisions for Au+Au at $\sqrt{s_{NN}}$ = 7.7, 11.5, 19.6, 27 and 39 GeV. The p_T range for this study is $0.2 < p_T < 2.0$ GeV/c. In the bottom panel, we show charged hadron v_1 as a function of p_T for central $(0-10\%)$, mid-central $(10-40\%)$ and peripheral $(40-80\%)$ collisions for Au+Au at $\sqrt{s_{NN}}$ = 7.7, 11.5, 19.6, 27 and 39 GeV. The pseudorapidity range for this study is $|\eta| < 1.0$.

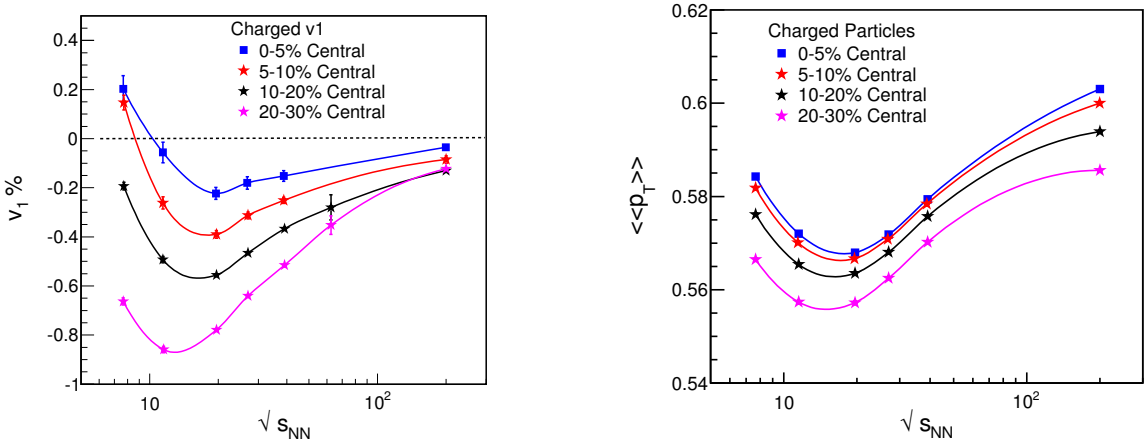

Figure 5.5: Charged hadron v_1 integrated in $|\eta| < 1$ and $0.2 < p_T < 2.0$ GeV/c as a function of beam energy in the left panel, and mean transverse momentum $\langle\langle p_T \rangle\rangle$ as a function of beam energy in the right panel. The results are for 0–5%, 5–10%, 10–20% and 20–30% central Au+Au collisions. The results at 62.4 and 200 GeV were previously reported by STAR [35].

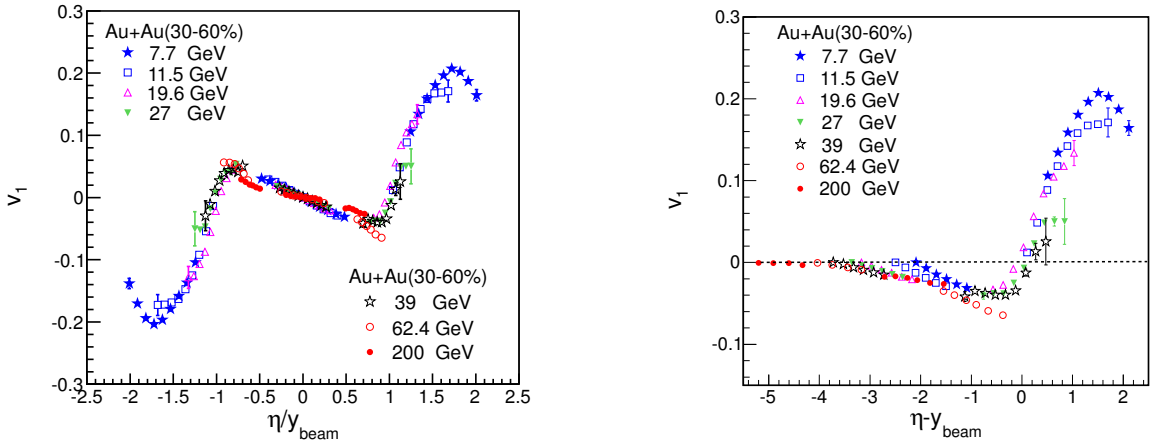

Figure 5.6: Charged hadron v_1 as a function of η scaled by the respective $y_{\rm beam}$ values on the left, and as a function of $\eta - y_{\rm beam}$ on the right, for beam energies of 7.7, 11.5, 19.6, 27, 39, 62.4 and 200 GeV. The results are for 30–60% central Au+Au collisions.

62.4 and 200 GeV. The results are for 30–60% central Au+Au collisions. An approximate scaling behavior is observed, similar to that previously reported by the STAR collaboration [74] and the NA49 Collaboration [40]. Fig 5.6, right panel, shows charged hadron $v_1\{\mathrm{BBC}\}$ as a function of $\eta - y_{\mathrm{beam}}$ in AuAu collisions for 30–60% centrality at $\sqrt{s_{NN}}$ = 7.7, 11.5, 19.6, 27, 39 GeV. The results at 62.4 and 200 GeV are $v_1\{\mathrm{ZDC\text{-}SMD}\}$ previously published by the STAR collaboration. Approximate scaling is observed as previously reported by PHOBOS [91] and STAR [35, 74, 80]. This approximate scaling extends the validity of the limiting fragmentation hypothesis [92] over a wider beam energy range than previously reported.

5.1.2 Identified Charged Particles

At lower beam energies, directed flow of protons was found to be positive and that of pions was reported to be negative. This was explained on the basis of different model calculations. The negative flow of pions was an outcome of shadowing by nucleons. At top SPS energy, some hints of negative flow of protons were observed using the standard event plane method, but the error bars were too large to make any conclusive statement in a multi-particle cumulant method with suppressed non-flow effects [40]. Hydro models suggest that this type of observation could be a signature of a change in equation of state from a hadronic to a QGP phase. Recently at 200 GeV, the STAR collaboration has reported results of directed flow of identified particles [85]. At higher beam energies, especially at 200 GeV, all the particle species studied show negative slope at mid rapidity. It has been argued that directed flow may exhibit flatness or negative slope at midrapidity due to a strong, tilted expansion of the source due to a possible QGP phase transition [**?**, 85].

Such a tilted expansion gives rise to antiflow or a 3rd flow component [87]. Another explanation for the negative flow of protons comes from positive space-momentum correlations coupled with baryon stopping [37].

Figure 5.7 shows directed flow in 7.7 through 39 GeV AuAu collisions for π^+ and π^- as a function of rapidity in the panels on the left, and as a function of transverse momentum in the panels on the right [86]. We observe a very small difference between the directed flow of π^+ and π^- at 7.7 GeV and this difference becomes smaller as beam energy increases. At 19.6 GeV and above, the difference between π^+ and π^- disappears.

Figure 5.8 shows directed flow in 7.7 through 39 GeV AuAu collisions for K^+ and K^- as a function of rapidity in the panels on the left, and as a function of transverse momentum in the panels on the right. We observe a very small difference between the directed flow of K^+ and K^-.

Figure 5.9 shows directed flow in 7.7 through 39 GeV AuAu collisions for protons and antiprotons as a function of rapidity in the panels on the left, and as a function of transverse momentum in the panels on the right. We observe a difference between the directed flow of protons and antiprotons [86]. This difference becomes smaller as the beam energy increases. The v_1 slope of antiproton is always negative from 7.7 GeV to 200 GeV whereas the proton v_1 slope changes from positive to negative between 7.7 and 11.5 GeV. Above 11.5 GeV, protons and antiprotons flow in the same direction but their magnitude is different. The proton slope is flatter that that of antiprotons.

In Fig. 5.10, $v_1(y)$ for protons (p) and for negative pions (π^-) is presented for central (0-10%), mid-central (10-40%) and peripheral (40-80%) collisions at the

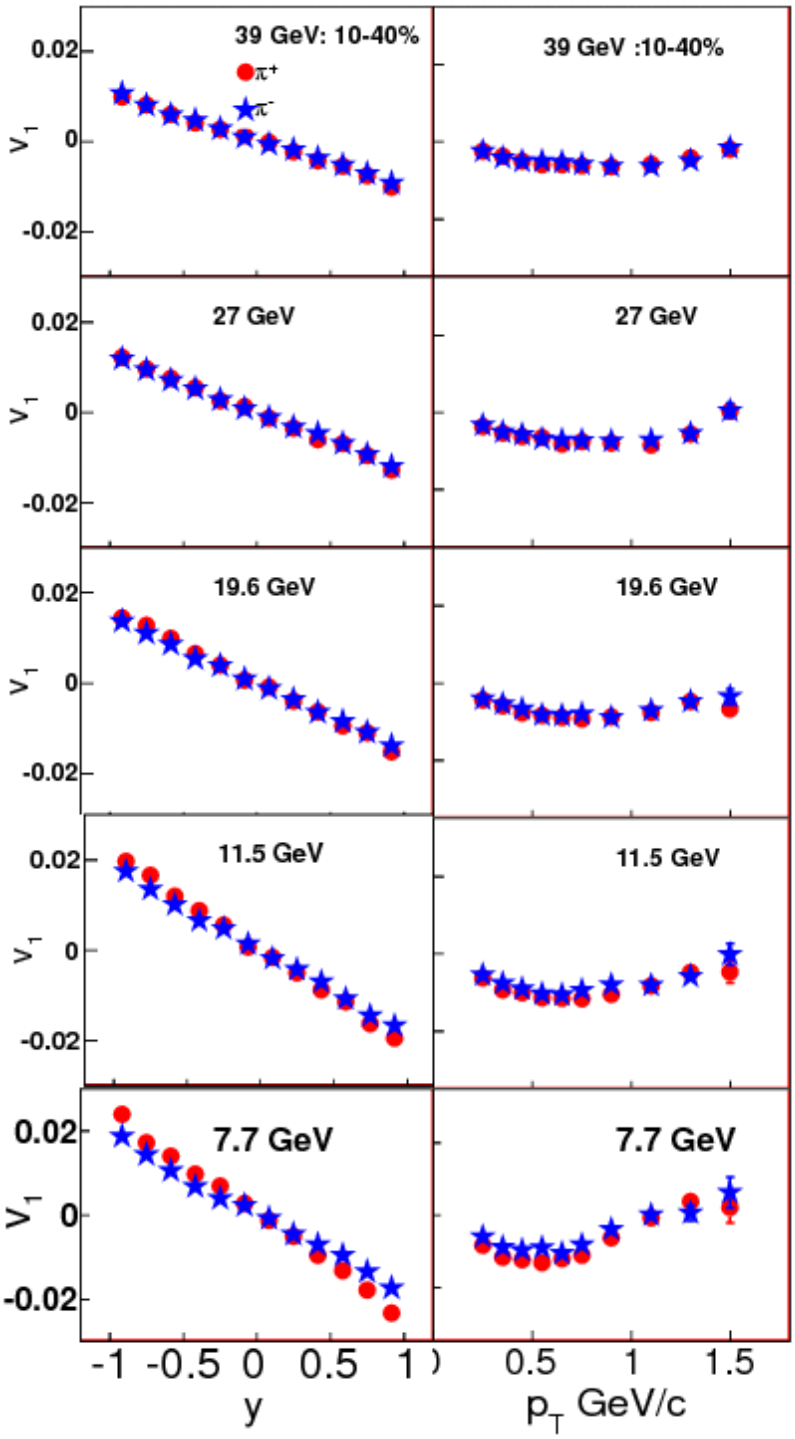

Figure 5.7: Directed flow in 7.7 through 39 GeV AuAu collisions for π^+ and π^- as a function of rapidity in the panels on the left, and as a function of transverse momentum in the panels on the right.

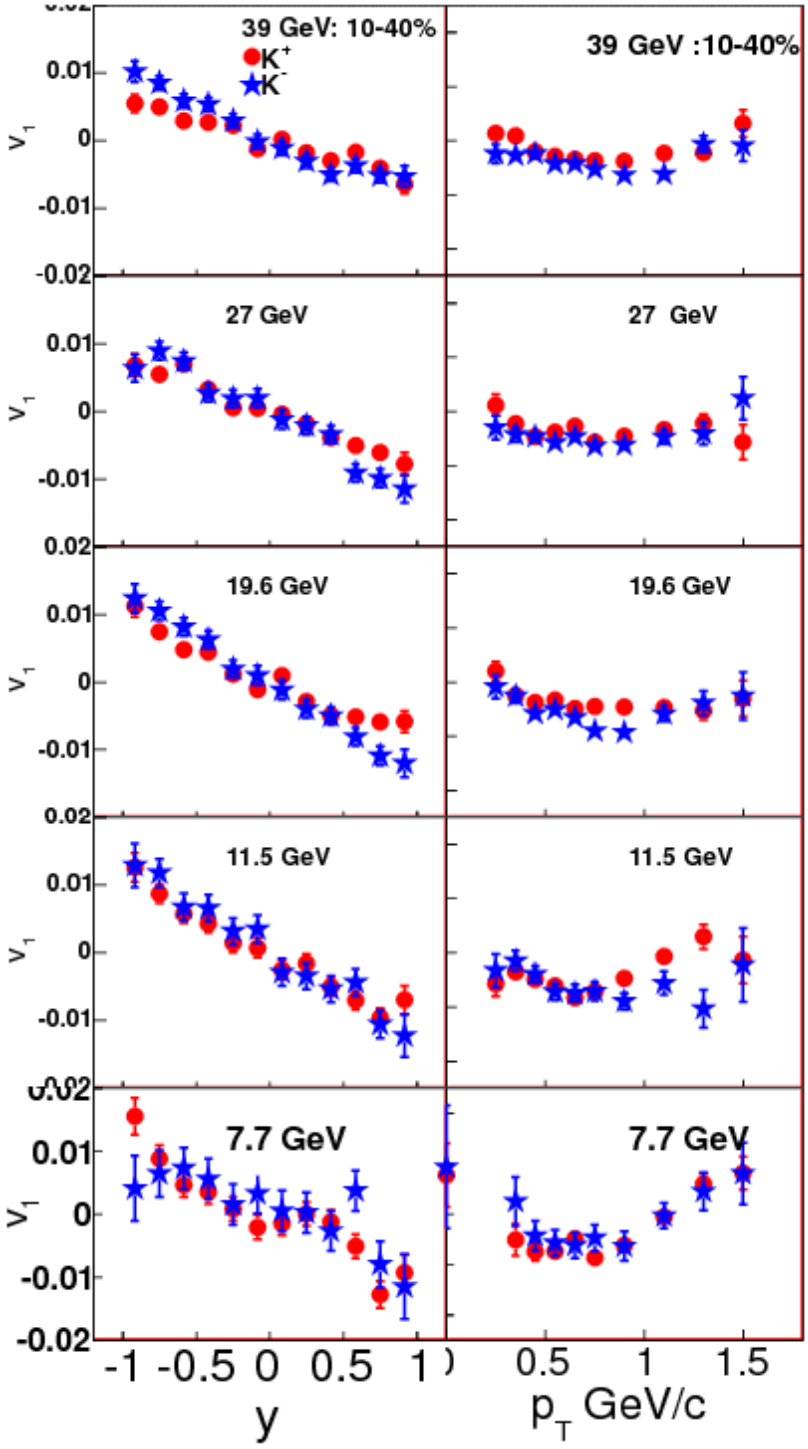

Figure 5.8: Directed flow Directed flow in 7.7 through 39 GeV AuAu collisions for K^+ and K^- as a function of rapidity in the panels on the left, and as a function of transverse momentum in the panels on the right.

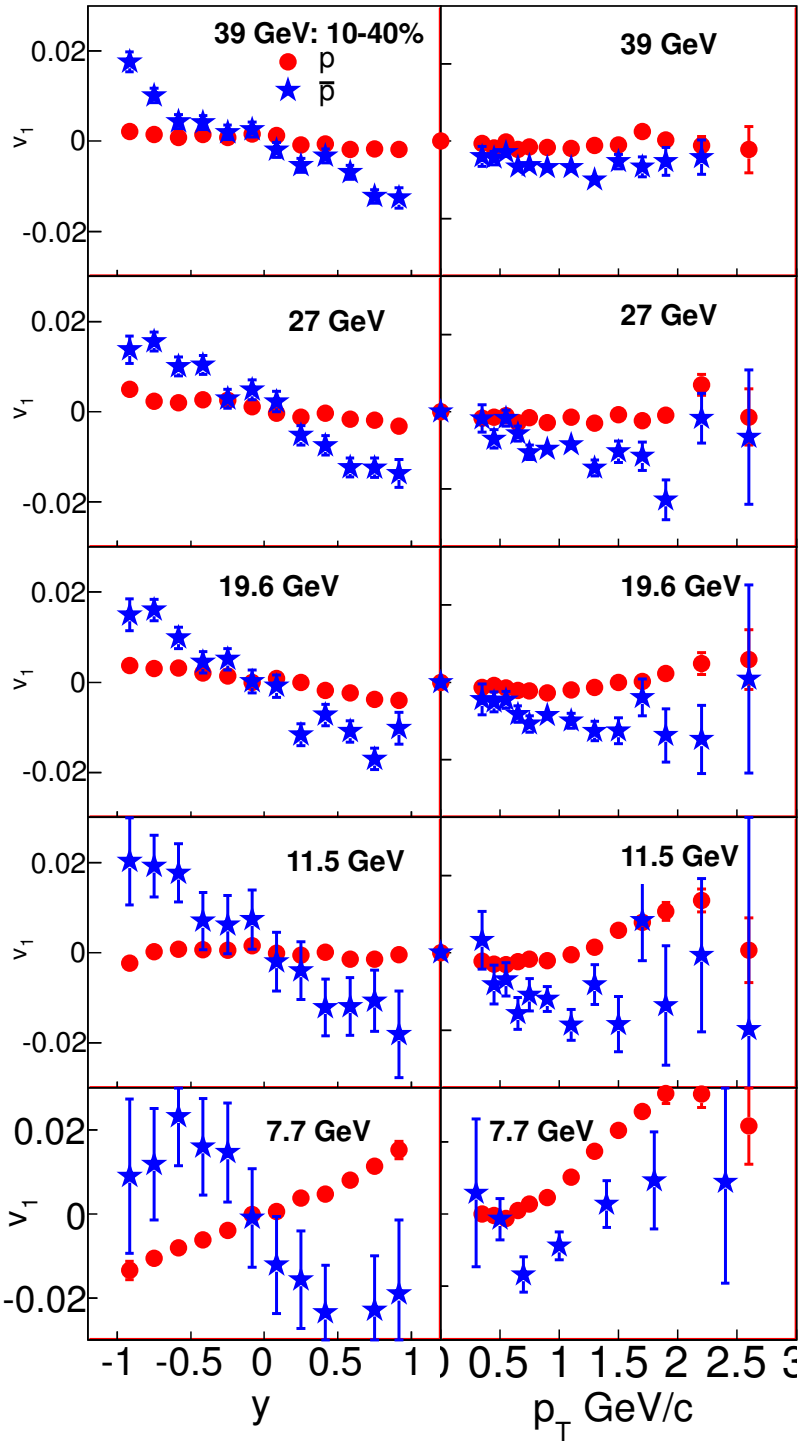

Figure 5.9: Directed flow in 7.7 through 39 GeV AuAu collisions for p and $\bar{p}$ as a function of rapidity in the panels on the left, and as a function of transverse momentum in the panels on the right.

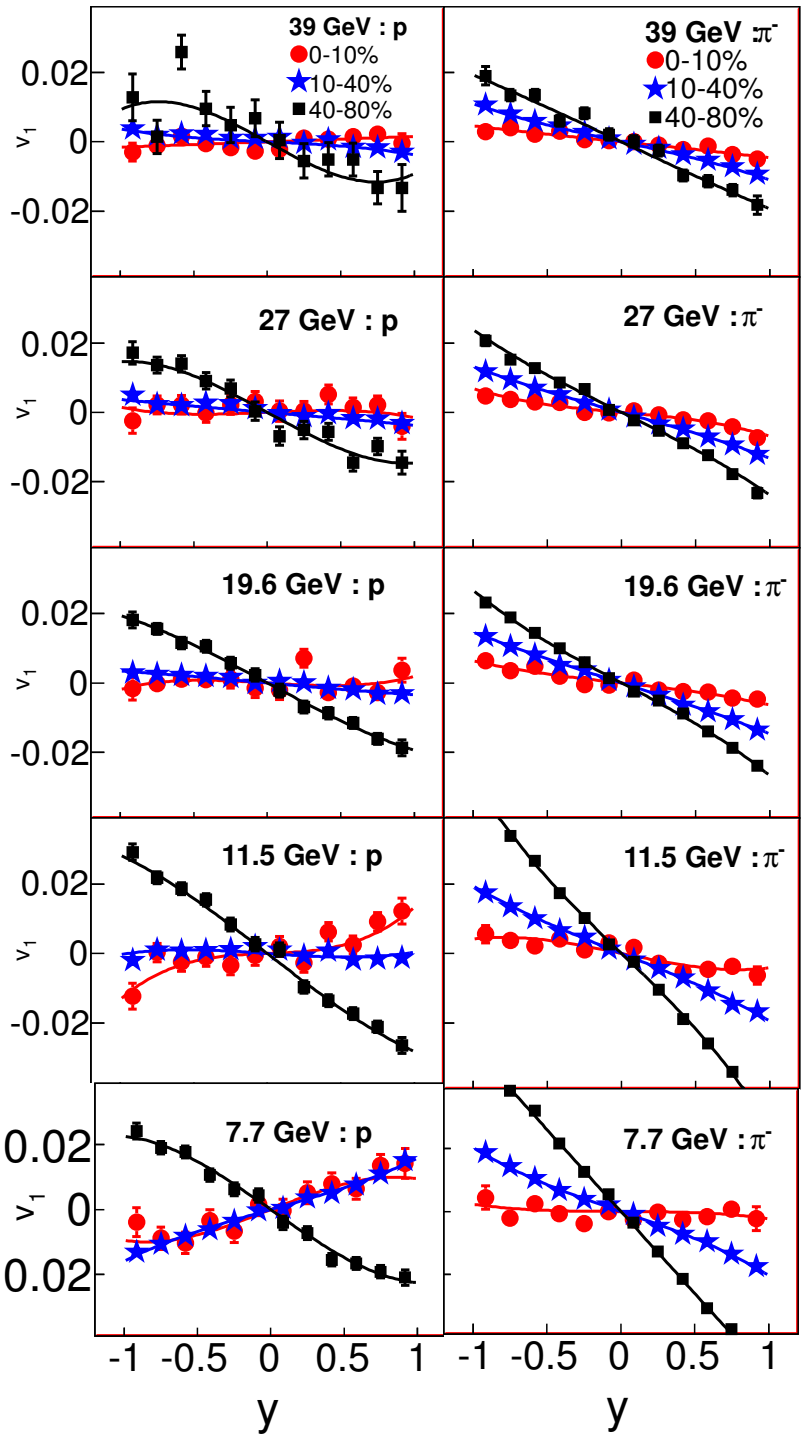

Figure 5.10: Directed flow of protons and π^- as a function of rapidity in the left and right panels, respectively, for central (0-10%), mid central (10-40%) and peripheral (40-80%) collisions at beam energies of 7.7-39 GeV.

five studied energies. The slopes of $v_1(y)$ in the vicinity of mid-rapidity for pions and protons are mostly negative for all energies and centralities, with an almost-flat proton flow in central collisions, apart from at 7.7 GeV. Figure 5.9 and 5.10 present the first observation of anti-flow of protons in mid-central collisions, and is evident well above statistical and systematic uncertainties at 19.6, 27 and 39 GeV. At 11.5 GeV, there is a very small negative flow. In contrast, NA49 has reported anti-flow in very peripheral collisions [40]. The present observation of anti-flow in mid-central collisions, where flow effects in general are at a maximum, suggests that anti-flow is associated with matter at high density and high excitation. Protons and pions at and above 11.5 GeV flow in same direction near mid-rapidity, which is argued to be consistent with emission from a tilted source [36, 89]. These results certainly cannot be explained by the baryon stopping picture [37], since we observe a large pion flow that is not opposite to proton flow except at 7.7 GeV. In peripheral collisions, a negative slope for directed flow of protons and pions at all energies may have a different origin that is unrelated to a phase transition [88].

In Fig. 5.11, $v_1(y)$ for protons and pions is presented for mid-central (10-40%) AuAu collisions at the five studied beam energies, and is compared to predictions from transport models. The model calculations shown are AMPT [53], both in default and string melting modes, and UrQMD [52]. These models qualitatively account for the pion flow but deviate, even at a qualitative level, from the observed proton flow.

The excitation function of proton $v_1(y')$ slope F (= dv_1/dy' at midrapidity) is presented in Fig 5.12 in the left panel. Values for F are extracted via a polynomial fit of the form $Fy' + Cy'^3$, where $y' = y/y_{\rm beam}$.

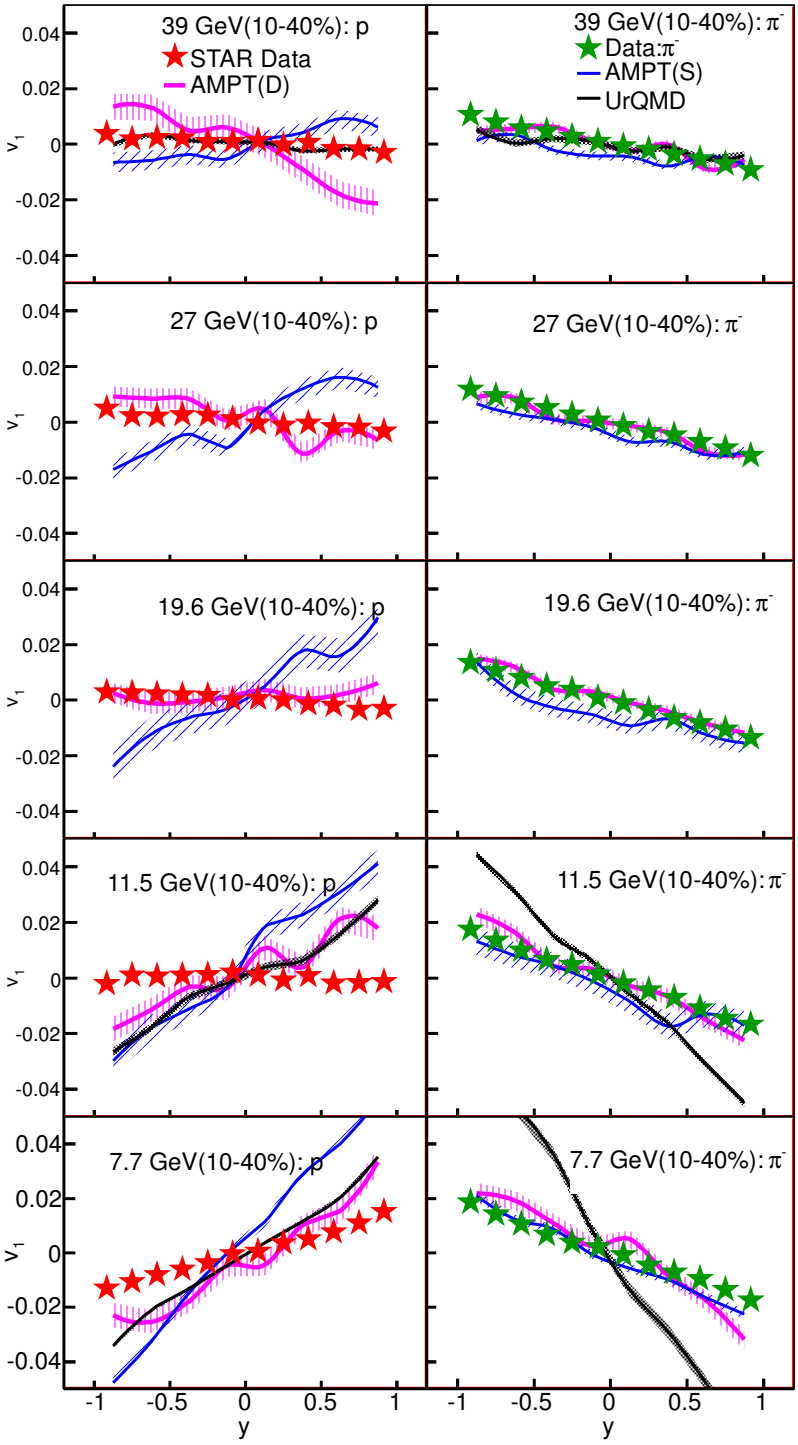

Figure 5.11: Directed flow of protons and π^- as a function of rapidity for mid-central collisions compared with transport model calculations for 7.7-39 GeV.

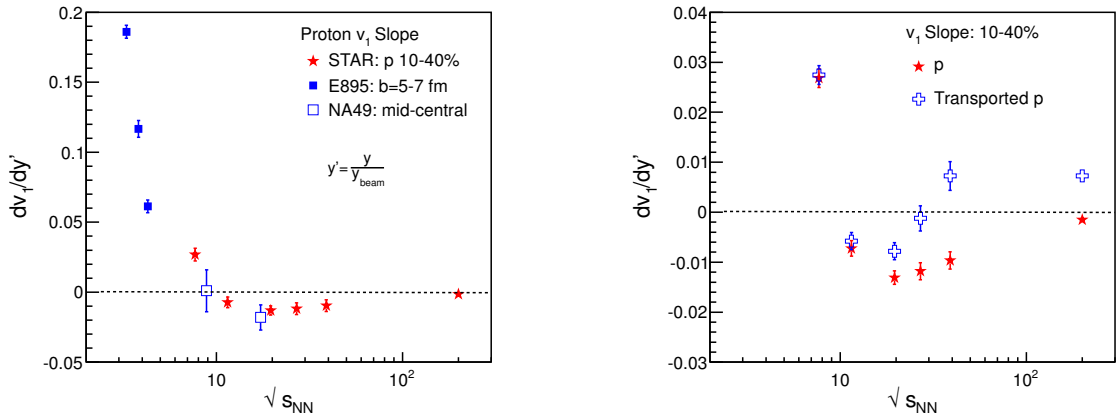

Figure 5.12: Directed flow slope (dv_1/dy') near mid-rapidity as a function of beam energy for mid-central Au+Au collisions, where the primed quantity y' refers to normalized rapidity $y/y_{\rm beam}$. The left panel shows proton measurements at higher resolution and compares all protons with estimated transported protons (see text).

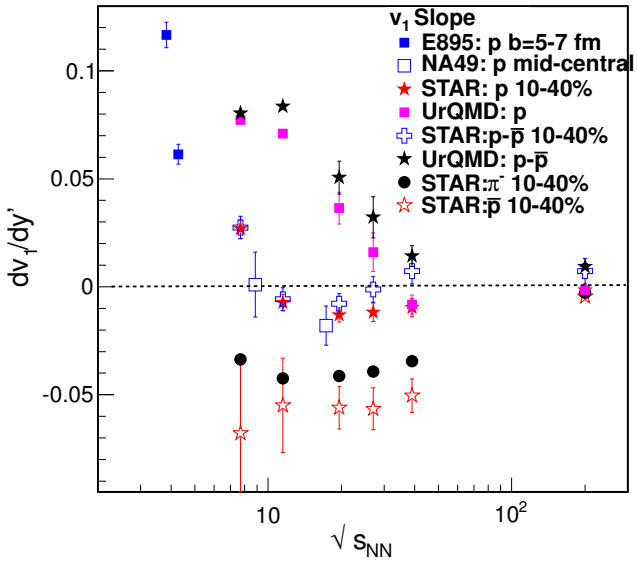

Figure 5.13: Directed flow slope (dv_1/dy') near mid-rapidity as a function of beam energy for mid-central Au+Au collisions, where the primed quantity y' refers to normalized rapidity $y/y_{\rm beam}$. The plot reports slopes for protons, antiprotons and pions, and also shows prior measurements and models.

Fig. 5.12, right panel, reveals that the inferred v_1 slope for transported baryon number becomes negative with a high level of significance at 11.5 and 19.6 GeV, while it is positive at all other energies. In contrast, the UrQMD model shows a positive slope at all energies for this observable as shown in Fig. 5.13. Thus there is no hint of this remarkable non-monotonic behavior in a hadronic model that has a good record of reproducing observed trends at least at a qualitative level. This new observation certainly requires more theoretical study.

The directed flow excitation function for protons near mid-rapidity is presented in Fig. 5.12 and for protons, antiprotons and pions in Fig. 5.13. At E895 energies, a related quantity $d\langle p^x\rangle/dy'$ was reported for protons only. For mid-central collisions, the proton slope decreases with energy and changes sign from positive to negative between 7.7 and 11.5 GeV, and remains small but negative up to 200 GeV, while pion and antiproton slope remains always negative. The energy dependence of proton dv_1/dy' involves an interplay between the flow of baryon number transported from the initial state to the vicinity of mid-rapidity, and the flow of protons from $p\bar{p}$ pairs produced near mid-rapidity. Obviously, the second mechanism increases strongly with beam energy, and it is helpful in interpretation to distinguish between the two as far as possible. $F_{\rm transp}$, the v_1 slope for transported baryon number (labelled $p-\bar{p}$ in the right panel of Fig. 5.12) is defined based on an equation in which the measured slope for protons is written $F = rF_{\bar{p}} + (1-r)F_{\rm transp}$, where r is the observed ratio of antiprotons to protons among the analyzed tracks at each beam energy. While this equation defines $F_{\rm transp}$, a simplified interpretation of this observable is suggested by the observation in the present analysis that $v_1(y)$ is almost the same for π^+ and π^- and for K^+ and K^- (in fact, they are

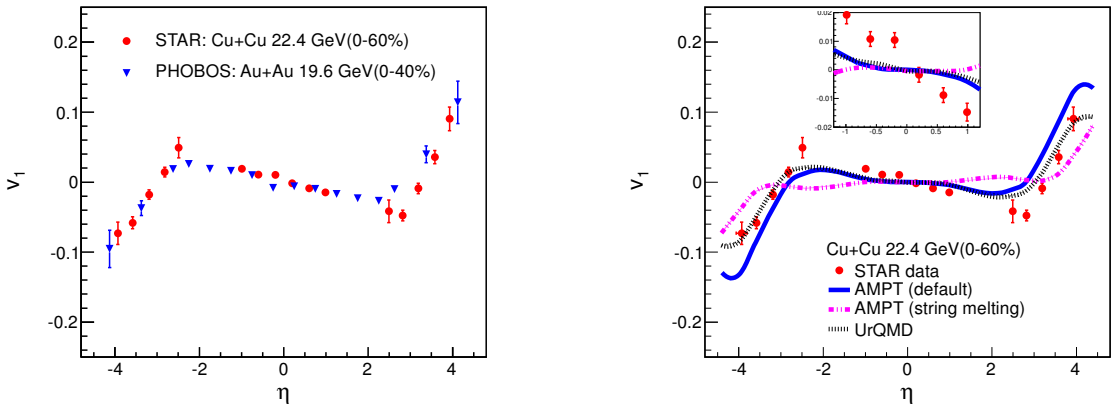

Figure 5.14: Charged hadron $v_1\{\text{BBC}\}$ vs. η for 0–60% centrality CuCu collisions at $\sqrt{s_{NN}} = 22.4$ GeV. Results are compared to v_1 from 0–40% centrality Au+Au collisions at $\sqrt{s_{NN}} = 19.6$ GeV from the PHOBOS collaboration [91] on the left, and with model predictions on the right. The inset shows the central η region in more detail.

indistinguishable within errors at the higher energies, and are only slightly different at 11.5 and 7.7 GeV). Specifically, the suggested interpretation is that $F_{\bar{p}}$ serves as a rough proxy or baseline for the directed flow from produced protons, and this guides our interpretation that F_{transp} isolates as far as possible the contribution of the initial-state baryonic matter. The recent study of Xu *et al.* addresses issues of hadronic potentials that might arise in interpretation of F_{transp} [90].

5.2 Directed Flow in 22.4 GeV CuCu Collisions

Figure 5.14 on the left shows charged hadron $v_1\{\text{BBC}\}$ in CuCu collisions for 0–60% centrality at $\sqrt{s_{NN}} = 22.4$ GeV as a function of η, compared to the same for 0-40% central AuAu collisions at $\sqrt{s_{NN}} = 19.6$ GeV measured by the PHOBOS experiment [91]. The PHOBOS results are quite similar, notwithstanding the difference in system size, and the fact that the centrality range and beam

energy are not the same. At 200 GeV and 62.4 GeV, it was previously reported that directed flow is not different within errors for AuAu and CuCu [35]. The present work demonstrates that this behavior extends to lower energies. Directed flow provides information about the collision process that complements the more widely-studied elliptic flow. Elliptic flow is imparted after a number of momentum exchanges among particles, and the number of such exchanges depends on the dimensions of the participant system and on its density. Consequently, for a given collision centrality, elliptic flow varies with the mass of the colliding nuclei. In contrast, the observation that directed flow does not vary with the mass of the colliding nuclei is a reflection of the different mechanism that generates v_1: here, the relevant feature is the rapidity shift undergone by particles that are initially located at different distances from the center of the participant volume [74] — a fundamental characteristic of the relativistic heavy-ion interaction process.

On the right of Fig. 5.14, we compare our measurements to the results of the A Multi Phase Transport (AMPT) [53] and Ultra Relativistic Quantum Molecular Dynamics (UrQMD) [52] models. Around midrapidity, the models predict substantially smaller slope of $v_1(\eta)$ than observed in the data, whereas at forward rapidities, the models differ among themselves and bracket the data. The fact that the tested models do not reproduce the observed pattern of v_1 as a function of pseudorapidity implies the need for further evolution in the model descriptions.

The left side of Fig. 5.15 shows charged hadron v_1 as a function of pseudorapidity scaled by the respective beam rapidity ($y_{\rm beam}$) values for the three beam energies 22.4, 62.4 and 200 GeV in CuCu collisions [35]. The results reported here for 22.4 GeV exhibit the same scaling behavior observed at top RHIC energies [35, 91] and

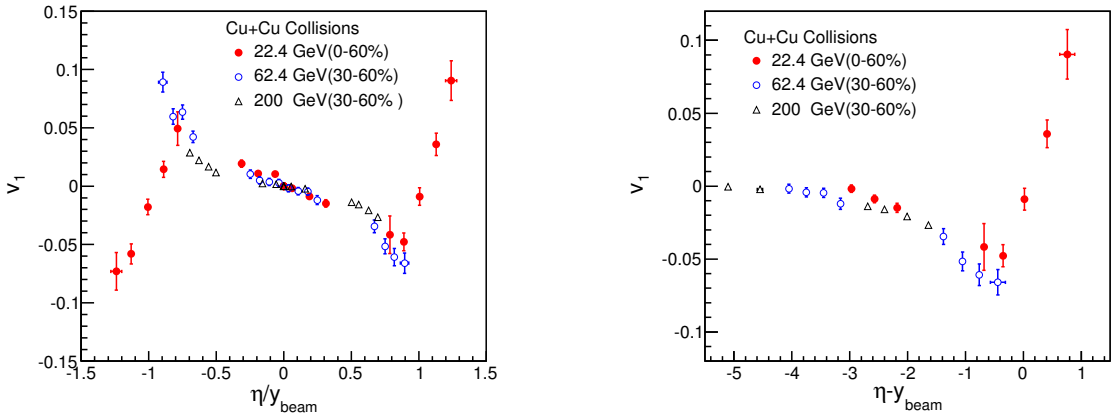

Figure 5.15: Charged hadron v_1 as a function of η scaled by the respective $y_{\rm beam}$ on the left, and as a function of η - $y_{\rm beam}$ values on the right, for the three beam energies 22.4, 62.4 and 200 GeV. The results for 62.4 and 200 GeV are for 30–60% centrality CuCu collisions previously reported by STAR [35], while at 22.4 GeV, they are for 0-60% centrality.

previously reported at SPS energies [40].

On the right, Fig. 5.15 shows charged hadron v_1 as a function of $\eta - y_{\rm beam}$, i.e. $v_1(\eta)$ in the projectile frame for three beam energies: 22.4, 62.4 and 200 GeV [35]. The data support the limiting fragmentation hypothesis [92] in the region $-2.6 < \eta - y_{\rm beam} < 0$.

5.3 Directed Flow in 9.2 GeV AuAu Collisions

Figure 5.16 shows charged hadron v_1 results in AuAu collisions for the 0–60% centrality interval at $\sqrt{s}_{NN}$ = 9.2 GeV, compared to corresponding results for 30–60% central Au+Au collisions at $\sqrt{s}_{NN}$ = 62.4 and 200 GeV [35]. The p_T range of this study is $0.15 - 2.00$ GeV/c. The v_1 results from Au+Au collisions at $\sqrt{s}_{NN}$ = 9.2 GeV are shown for three different methods: the BBC event plane method, the FTPC event plane method, and the mixed harmonic method. Results from the

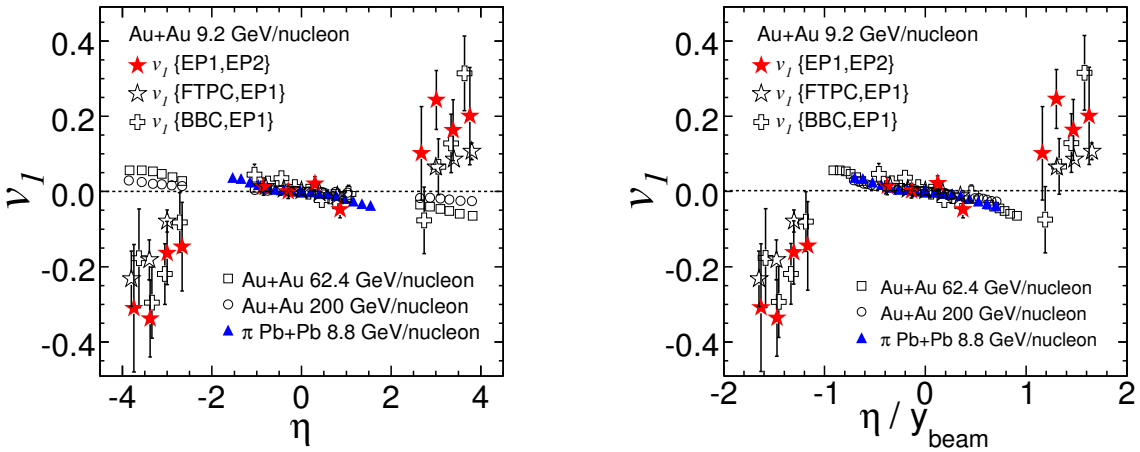

Figure 5.16: Charged hadron v_1 vs. η from the 0–60% collision centrality AuAu collisions at $\sqrt{s_{NN}}$ = 9.2 GeV [13]. The solid star symbols are the results obtained from the mixed harmonic method, while the open star and open plus symbols represent results from the standard methods (see text for details). The results are compared to v_1 from 30–60% centrality AuAu collisions at $\sqrt{s_{NN}}$ = 62.4 and 200 GeV [35]. For comparison, v_1 for charged pions at 0–60% centrality in PbPb collisions at $\sqrt{s_{NN}}$ = 8.8 GeV are also shown [40]. On the right, the same measurements are plotted as a function of η scaled by the respective $y_{\rm beam}$.

three methods are consistent within the error bars. These results are also compared with v_1 for charged pions in Pb+Pb collisions at $\sqrt{s_{NN}}$ = 8.8 GeV measured by NA49 [40]. At midrapidity, all results are comparable. At forward rapidity ($|\eta| > 2$), the trend of v_1 for higher $\sqrt{s_{NN}}$ (62.4 and 200 GeV) appears to be different from that for $\sqrt{s_{NN}}$ = 9.2 GeV. This can be explained by contributions from spectator protons to the directed flow signal at large $|\eta|$. The beam rapidities ($y_{\rm beam}$) for $\sqrt{s_{NN}}$ = 9.2, 62.4, and 200 GeV are 2.3, 4.2, and 5.4, respectively. With η divided by the respective $y_{\rm beam}$ values, all the v_1 measurements follow a common trend for the measured pseudorapidity range.

5.4 Systematic Uncertainties

When the event plane for a directed flow measurement is determined from a detector that is not symmetric around $\eta = 0$, we need to account for correlations due to momentum conservation [78]. The desired BBC η symmetry is present for our v_1 analysis in the η region of the central TPC, but is a source of possible concern for the FTPC η region. The overlap in η acceptance between the BBC and FTPC is only partial, and therefore it is feasible to compare $v_1\{\text{BBC}\}_{\rm full}$, using the combined full event plane based on both BBCs, with $v_1\{\text{BBC}\}_{\rm sub}$, using a single BBC sub-event plane for $2.5 < |\eta| < 3.3$. We find that the difference is less than 10%, and an extrapolated average correction has been applied to $v_1\{\text{BBC}\}$ for $|\eta| > 3.3$.

The measured v_1 has to be anti-symmetric about mid-pseudorapidity within statistical errors. Any difference is due to systematic uncertainties. Previous detailed studies point to the maximum forward-backward difference as a viable estimate of the overall systematic uncertainty when the pseudorapidity gap is large [35].

The difference in measured value with respect to the event planes reconstructed in different detectors also gives an estimate of the systematic error. We estimate the difference between $v_1\{\mathrm{BBC}\}$ and $v_1\{\mathrm{FTPC}\}$, and this difference is less than 2% in TPC region and 5% in FTPC region. We estimate the systematic uncertainty on event plane flattening methods by the variance between them and find it to be negligible (below 1%).

Results for pions and protons are not corrected for feed-down from weak decays. The systematic uncertainties arising from particle misidentification and detector inefficiency are estimated by varying the event and track cuts, and are concluded to be at the level of about 5%. Because of the large pseudorapidity gap between the BBC and TPC, the non-flow contribution in $v_1\{\mathrm{BBC}\}$ is negligible. We conclude that the overall systematic uncertainty in our determination of v_1 is approximately 15% in the FTPC region, and 10% in the central TPC region.

5.5 Summary

I presented measurements of directed flow of charged particles and of charged pions, kaons, protons and antiprotons for AuAu collisions at 7.7, 11.5, 19.6, 27 and 39 GeV. I also present directed flow of charged particles for 22.4 GeV CuCu collisions and 9.2 GeV AuAu collisions. The centrality dependence of the charged hadron directed flow as a function of pseudorapidity and transverse momentum observed at these energies is similar to results observed at the top RHIC energy. We observe that $v_1(\eta/y_{beam})$ for 30-60% central collisions lies close to a single common curve for all beam energies as previously reported by NA49 [40] and STAR [74]. Beam energy scaling of charged hadron v_1 as a function of $(\eta - y_{beam})$ for 30-60% central collisions resembles the pattern previously reported

by PHOBOS [91]. These approximate scaling behaviors are equally observed in AuAu collisions as well as CuCu collisions. These observations support the limiting fragmentation hypothesis [92].

At 200 GeV and 62.4 GeV, it was previously reported that directed flow is not different within errors for AuAu and CuCu [35]. We find that this behavior extends to lower energies, as evident from comparison between CuCu 22 GeV and AuAu 19.6 GeV collisions [74].

For charged particles in 0-30% central collisions, we observe a local minimum of integrated $(0.2 < p_T < 2.0$ GeV/c and $|\eta| < 1.0)$ directed flow above 11.5 GeV. This type of observation has been argued to be of interest in studying the softest point in the Nuclear Equation of State [81, 84]. The mean transverse momentum also shows a similar behavior. The minimum in directed flow survives when scaled with mean transverse momentum, but this alone cannot exclude the possibility of a connection between them. This is a very interesting observation and further investigation is necessary to fully understand it.

We report directed flow of identified particles. Differences in directed flow between positive and negative hadrons, especially for protons and antiprotons, is observed and this difference becomes smaller for higher beam energies. For mid-central collisions, the proton v_1 slope in the mid-rapidity region changes sign from positive to negative between 7.7 and 11.5 GeV and remains small but negative up to 200 GeV, while the slope for pions, kaons and antiprotons remains always negative. Based on transport model comparisons, the observed trends in these data above 11.5 GeV can qualitatively be understood in terms of anisotropic emission of produced particles from a tilted disk. A striking observation is that the v_1 slope

for net protons, which is an estimate of the directed flow contribution from baryon number transported to the midrapidity region, changes sign twice within the energy range studied here [8]. This result is qualitatively different from transport model calculations, which exhibit a monotonic trend with no sign reversal.

Chapter 6

RESULTS – II: ELLIPTIC FLOW

In this chapter, I present the elliptic flow results at $\sqrt{s_{NN}}$ = 7.7, 11.5, 19.6, 27 and 39 GeV for AuAu collisions and at $\sqrt{s_{NN}}$ = 22.4 GeV for CuCu collisions.

6.1 AuAu Collisions at 7.7, 11.5, 19.6, 27 and 39 GeV

At these energies, the first-order event plane from the BBC is used in the measurement of elliptic flow. In mid-central collisions, the BBC event plane resolution for v_2 measurement is more than adequate. However, in the most central and in very peripheral collisions, the event plane resolution becomes poor.

6.1.1 Pseudorapidity and Transverse Momentum Dependence

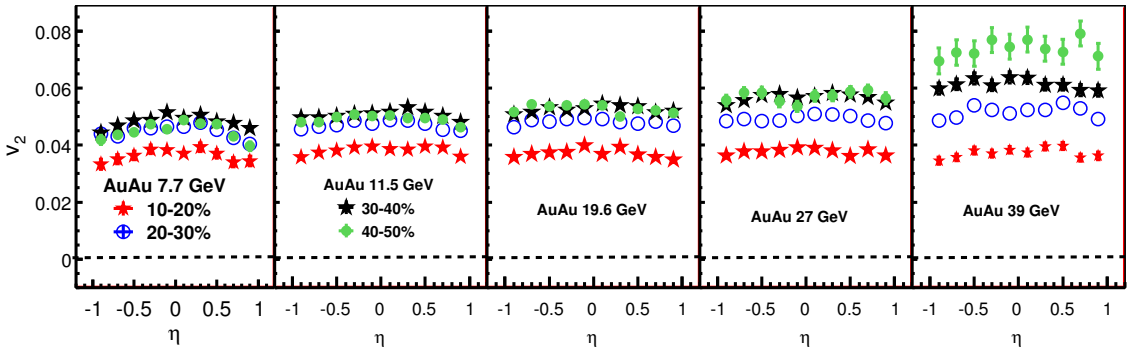

Figure 6.1: $v_2\{\mathrm{BBC}\}$ vs. η at midrapidity in AuAu at $\sqrt{s_{NN}}$ = 7.7, 11.5, 19.6, 27 and 39 GeV. The results are shown for four collision centrality classes: 10–20%, 20–30%, 30–40%, and 40–50%.

In Fig. 6.1, the centrality dependence of $v_2\{\mathrm{BBC}\}$ as a function of η is shown for AuAu collisions at $\sqrt{s_{NN}}$ = 7.7, 11.5, 19.6, 27 and 39 GeV. The results are

shown for collision centralities 10–20%, 20–30%, 30–40%, and 40–50%, where the BBC event plane resolution is close enough to its maximum. For more central and more peripheral collisions, errors grow because of poor event plane resolution.

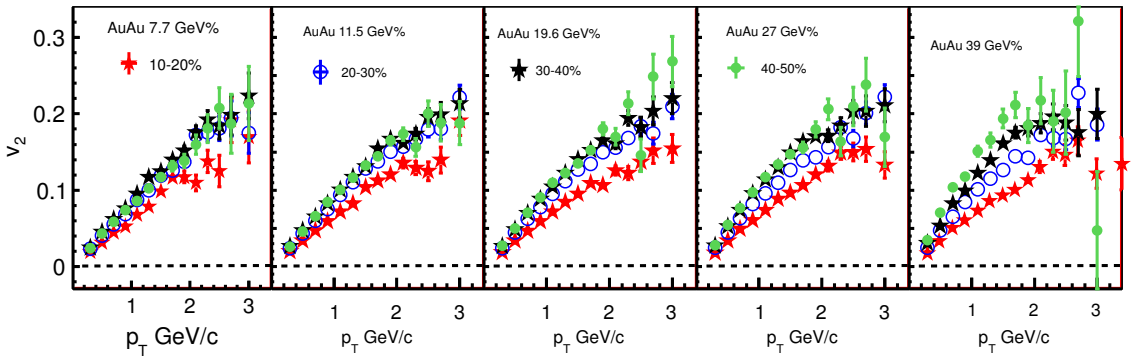

Figure 6.2: $v_2\{\mathrm{BBC}\}$ vs. p_T at mid-rapidity for $\sqrt{s_{NN}}$ = 7.7, 11.5, 19.6, 27 and 39 GeV AuAu collisions. Results are shown for four collision centrality classes: 10–20%, 20–30%, 30–40%, and 40–50%.

In Fig. 6.2, the centrality dependence of $v_2\{\mathrm{BBC}\}$ as a function of p_T is shown for AuAu collisions at $\sqrt{s_{NN}}$ = 7.7, 11.5, 19.6, 27 and 39 GeV. The results are shown for collision centralities 10–20%, 20–30%, 30–40%, and 40–50%, where the BBC event plane resolution is close enough to its maximum. For more central and more peripheral collisions, errors grow because of poor event plane resolution. For these beam energies, the centrality dependence of $v_2(\eta)$ and $v_2(p_T)$ is similar to what has been already reported at higher beam energies (62.4 and 200 GeV) for AuAu and CuCu colliding systems [94, 95]. The increase in magnitude of v_2 from central to peripheral collisions could be explained by the larger initial eccentricity in the coordinate space of the more peripheral collisions.

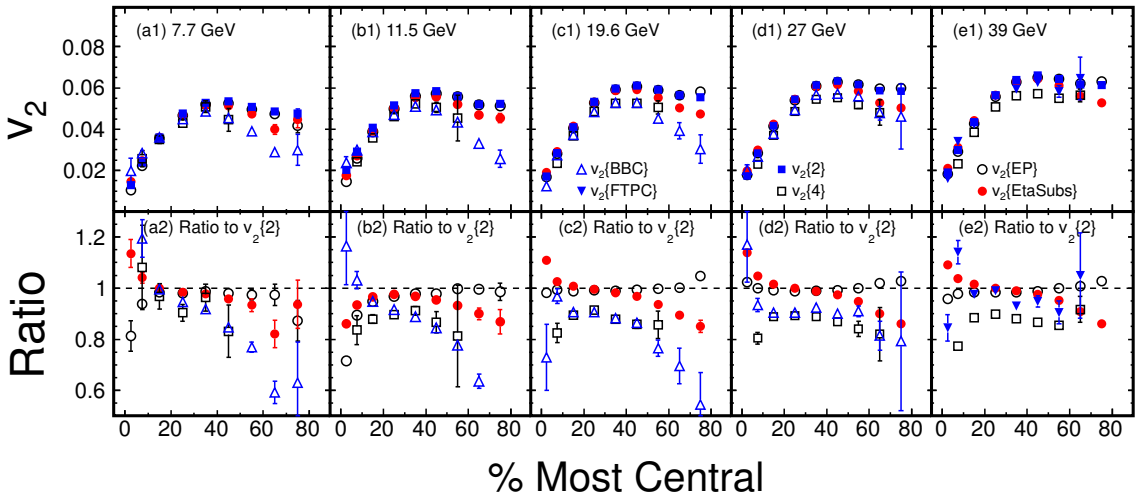

Figure 6.3: The p_T- and η-integrated v_2 ($p_T > 0.2$ GeV/c and $|\eta| < 1$) as a function of collision centrality for AuAu collisions at $\sqrt{s_{NN}}$ = 7.7 GeV (a1), 11.5 GeV (b1), 19.6 GeV (c1), 27 GeV (d1) and 39 GeV (e1). The results in the top panels are presented for several methods of obtaining v_2. The bottom panels show the ratio of v_2 obtained using the various techniques, relative to $v_2\{2\}$ [93].

6.1.2 Method Comparison

Method comparisons are shown in Fig. 6.3 and 6.4 for charged hadrons in AuAu collisions at $\sqrt{s_{NN}}$ = 7.7–39 GeV. Figure 6.3 shows the p_T- and η-integrated v_2 ($p_T > 0.2$ GeV/c and $|\eta| < 1$) as a function of collision centrality. The bottom panels show the ratio of v_2 obtained using the various techniques, relative to $v_2\{2\}$ [93] (the 2-particle cumulant method). Within statistical errors, the results of $v_2\{\mathrm{BBC}\}$ at $\sqrt{s_{NN}}$ = 7, 11.5, 19.6 and 27 GeV and $v_2\{\mathrm{FTPC}\}$ at $\sqrt{s_{NN}}$ = 39 GeV for Au+Au are consistent with $v_2\{2\}$, $v_2\{\mathrm{EP}\}$ and $v_2\{\mathrm{EtaSubs}\}$ in central and semi-central collisions (10–20% through 40–50%) [93]. The results of $v_2\{\mathrm{BBC}\}$ and 4-particle cumulant methods are systematically lower than other methods in more central (0–10%) and more peripheral (50–80%) collisions. In peripheral collisions, non-flow contributions may play a role in these differences, and in central collisions,

fluctuations may have a role.

The p_T differential v_2 from various methods for the 20–30% centrality bin is shown in the upper panels of Fig. 6.4. For comparison, the v_2 from other methods is divided by the results of the 2-particle cumulant method and shown in the lower panels of Fig. 6.4. It can be seen that the difference of $v_2\{2\}$ compared to $v_2\{\mathrm{FTPC/BBC}\}$, $v_2\{2\}$ and $v_2\{\mathrm{EtaSubs}\}$ depends on the p_T range. A relatively large difference can be observed in the low p_T region ($p_T < 1$ GeV/c)

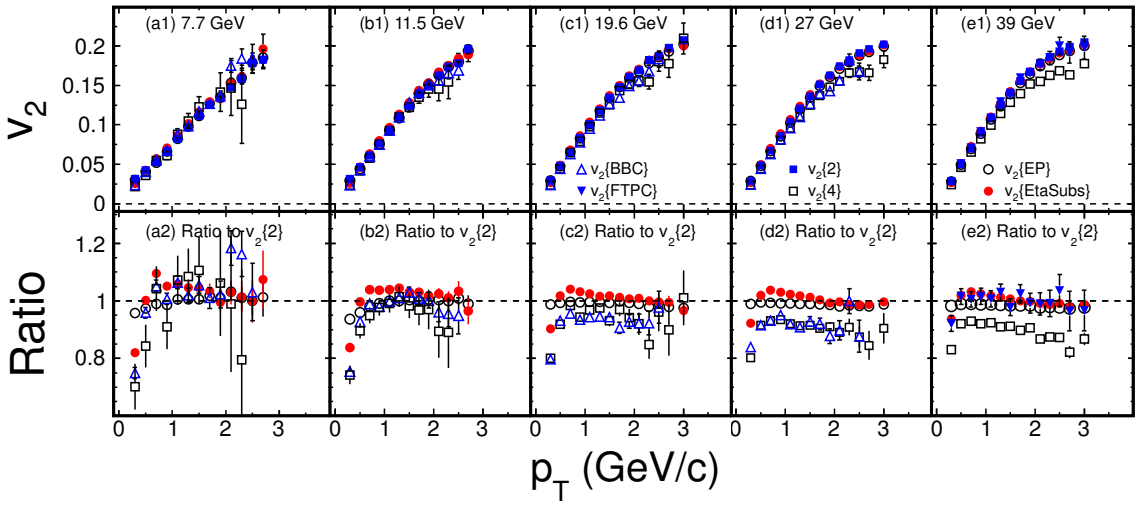

Figure 6.4: v_2 as a function of p_T for $20-30\%$ central AuAu collisions at mid-rapidity for $\sqrt{s_{NN}}$ = 7.7 - 39 GeV. The top panels show v_2 vs. p_T using various methods as labeled in the figure. The bottom panels show the ratio of v_2 measured using various methods with respect to the fitted $v_2\{2\}(p_T)$.

and beyond p_T = 1 GeV/c, the difference stays constant. The difference between $v_2\{\mathrm{FTPC/BBC}\}$ and $v_2\{4\}$ is relatively small and less dependent on p_T. It suggests that the non-flow contribution to the event plane and 2-particle correlation methods depends on p_T. Based on the interpretation in Ref. [75], the difference between $v_2\{2\}^2$ and $v_2\{4\}^2$ is related to a combination of non-flow and v_2 fluctuations. The

fact that the ratio of $v_2\{4\}$ to $v_2\{2\}$ is closer to 1 at the lower collision energies suggests that the non-flow and/or v_2 fluctuations in the v_2 measurement depends on the collision energy. One possible explanation is that the non-flow correlations from jets presumably decrease as the collision energy decreases. The results of $v_2\{\mathrm{BBC}\}$ are found to be consistent with $v_2\{4\}$ at 7.7, 11.5, 19.6 and 27 GeV, while the $v_2\{\mathrm{FTPC}\}$ is larger than $v_2\{4\}$ at 39 GeV. This consistency can be also observed in Fig. 6.3 for 10–20% through 40–50% centrality bins. It suggests that the use of the first-order reaction plane (BBC event plane) to study the second harmonic flow eliminates flow fluctuations which are not correlated between different harmonics.

6.1.3 Beam Energy Dependence

One of the most important experimental observations at RHIC is the significant v_2 signal at the top energy of AuAu collisions [94, 95] (more than 50% larger than at the SPS [40]). This could be interpreted as the observation of a higher degree of thermalization than at lower collision energies. The Beam Energy Scan data from STAR offers an opportunity to study the beam energy dependence of v_2. Figure 6.5 shows the results of p_T dependence of $v_2\{4\}$ from $\sqrt{s}_{NN}$ = 7.7 GeV to 2.76 TeV in the 20–30% centrality bin [93]. The ALICE results at $\sqrt{s}_{NN}$ = 2.76 TeV are from a different but very similar colliding system (PbPb) [96]. At low p_T ($p_T < 2$ GeV/c), where hydrodynamic calculations are applicable, the v_2 values increases with increasing beam energy. Beyond $p_T = 2$ GeV/c, the v_2 results show comparable values within statistical errors. There is no saturation behavior in v_2 up to collisions at $\sqrt{s}_{NN}$ = 2.76 TeV. This suggests that a higher degree of thermalization could be reached at higher beam energy.

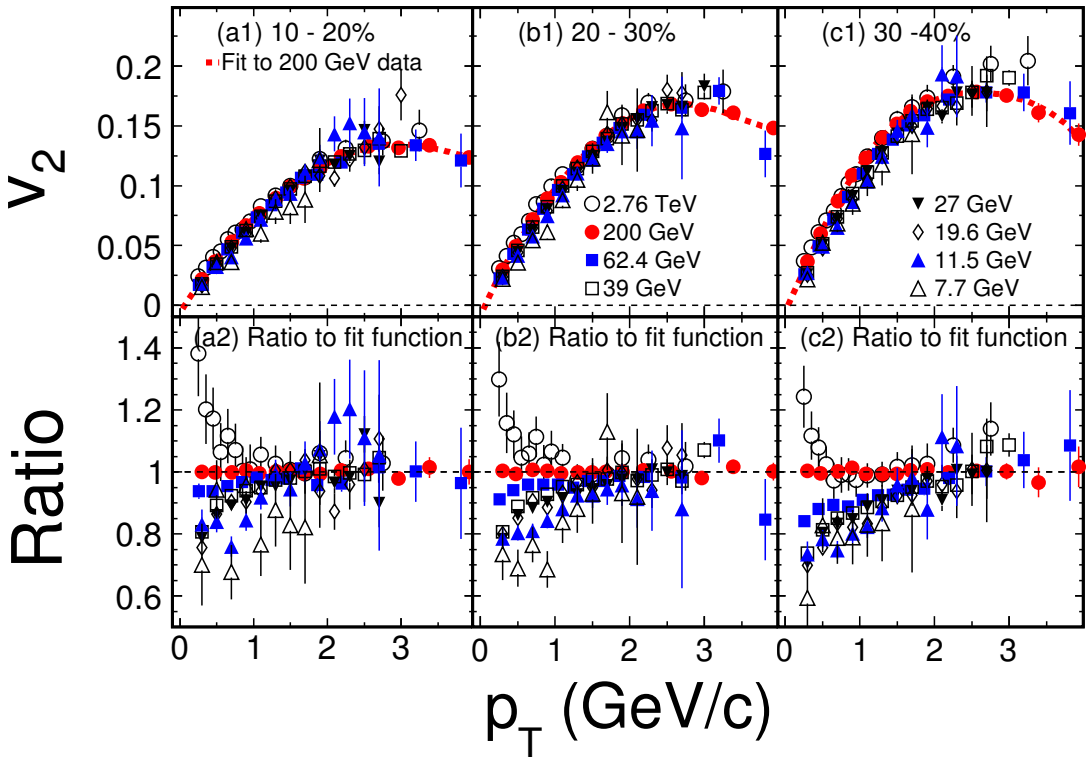

Figure 6.5: The top panels show $v_2\{4\}$ vs. p_T at mid-rapidity for various beam energies ($\sqrt{s_{NN}}$ = 7.7 GeV to 2.76 TeV). The results for $\sqrt{s_{NN}}$ = 7.7 to 200 GeV are for AuAu collisions and those for 2.76 TeV are for Pb + Pb collisions. The red line shows a fit to the results from AuAu collisions at $\sqrt{s_{NN}}$ = 200 GeV. The bottom panels show the ratio of $v_2\{4\}$ vs. p_T for all $\sqrt{s_{NN}}$ with respect to this fitted curve. The results are shown for three collision centrality classes: 10–20% (a), 20–30% (b) and 30–40% (c) [93].

6.2 CuCu Collisions at 22.4 GeV

In the elliptic flow measurement, we have used the η sub-event method with a gap of 0.3 units in pseudorapidity (η), such a gap suppresses short-range correlations such as Bose-Einstein interference and Coulomb final-state interactions. To study possible systematic effects associated with short-range non-flow correlations, a four-particle cumulant [75] analysis $v_2\{4\}$ as a function of centrality has been investigated.

This method removes non-flow correlations involving fewer than four particles. The results from this $v_2\{4\}$ analysis agree, within statistical errors, with the $v_2\{\mathrm{TPC}\}$ results presented here. The statistical errors on our $v_2\{4\}$ measurements are small enough to be useful for the most central collisions (where the error is about 14%) but grow to a few tens of percent at the other end of our studied centrality range.

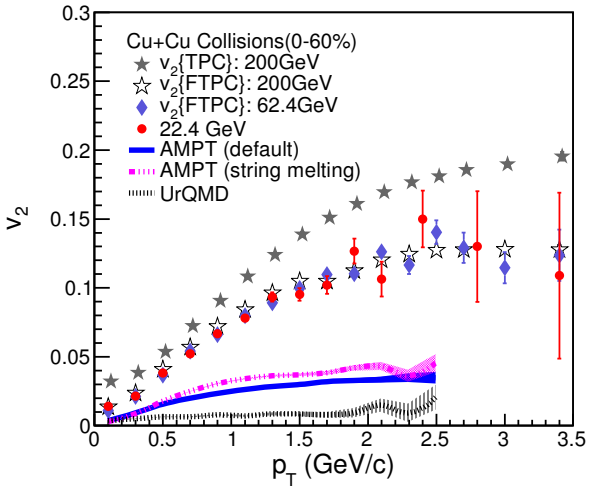

Figure 6.6: Elliptic flow versus p_T for charged hadrons from CuCu 0–60% centrality collisions at $\sqrt{s_{NN}} = 22.4$ GeV, measured by the sub-event method with a pseudorapidity gap of 0.3 units, compared with STAR results for 200 and 62.4 GeV CuCu [94] measured with the full TPC event-plane method $v_2\{\mathrm{TPC}\}$ and full FTPC event plane method $v_2\{\mathrm{FTPC}\}$. Results are also compared to $v_2(p_T)$ model calculations [74].

Figure 6.6 shows $v_2(p_T)$ for charged hadrons from CuCu collisions at $\sqrt{s_{NN}} = 22.4$ GeV measured by the sub-event method with a pseudorapidity gap of 0.3 units. Also shown are the previously published STAR results for 200 and 62.4 GeV CuCu [94] measured by the full TPC event-plane method $v_2\{\mathrm{TPC}\}$ and full FTPC event-plane method $v_2\{\mathrm{FTPC}\}$. We observe that the elliptic flow at 22.4 GeV is systematically lower than $v_2\{\mathrm{TPC}\}$ at 200 GeV. However, it is similar to $v_2\{\mathrm{FTPC}\}$ at 200 and 62.4 GeV, consistent with an earlier observation [97]. For

comparison, we also show $v_2(p_T)$ from the UrQMD and AMPT models. The models do not agree with the data, but they do show an increase in v_2 with transverse momentum, similar to the data, and they reach a plateau at much lower values of p_T. The small sample size in the present analysis precludes an extension of the measurements to identified particle v_2.

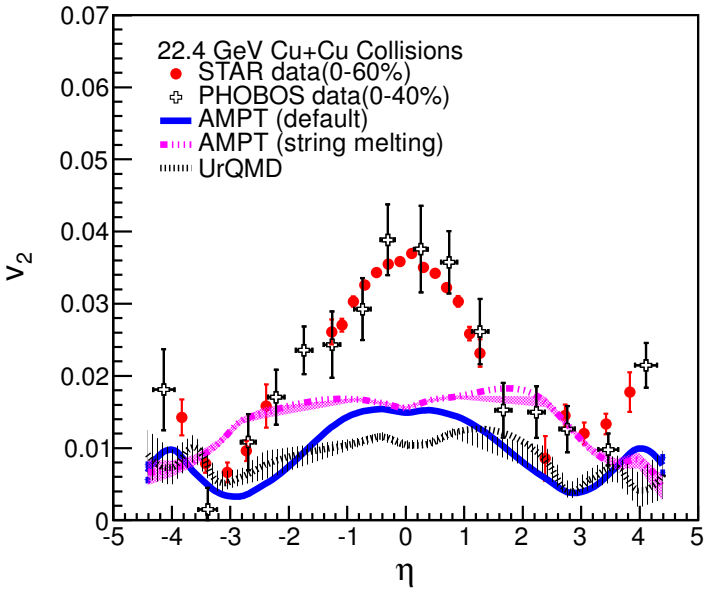

Figure 6.7: Elliptic flow $v_2(\eta)$ for charged hadrons from CuCu collisions at 0–60% centrality at $\sqrt{s_{NN}} = 22.4$ GeV. The present STAR results are compared to the measurement from the PHOBOS [98] collaboration for CuCu at 22.4 GeV. The PHOBOS results include statistical and systematic errors whereas the STAR results are plotted with statistical uncertainties only [74]. Results are also compared to $v_2(\eta)$ calculations from the indicated models.

Figure 6.7 shows $v_2(\eta)$ for charged hadrons from 0–60% centrality CuCu collisions at $\sqrt{s_{NN}} = 22.4$ GeV. These STAR results are compared to published measurements from the PHOBOS Collaboration for 0–40% central collisions at $\sqrt{s_{NN}} = 22.4$ GeV [98]. The PHOBOS error bars include statistical and systematic errors, whereas the STAR data are plotted with statistical error bars only. The

STAR results for $v_2(\eta)$ are consistent within errors with the PHOBOS data. We also compare with corresponding predictions from the AMPT and UrQMD models. These models underpredict the data at midrapidity, but do show a trend that is similar to the data for $|\eta| > 2.0$.

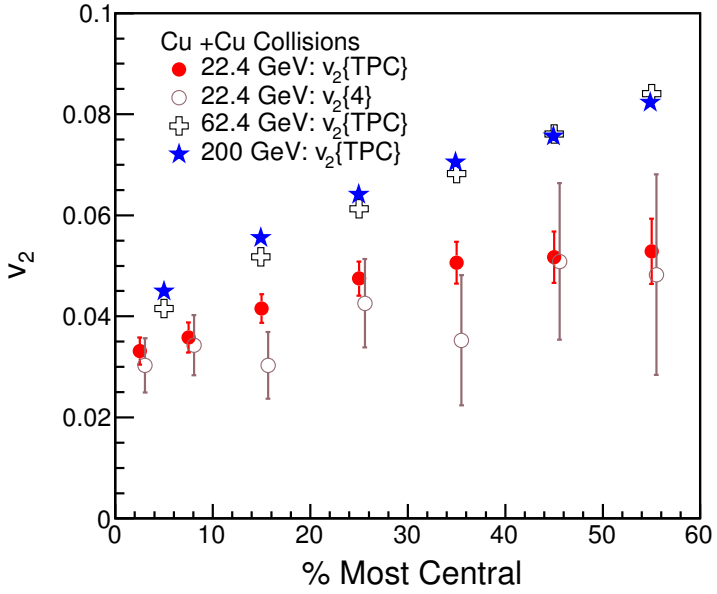

Figure 6.8: Elliptic flow $v_2\{\text{TPC}\}$ as a function of centrality for charged hadrons from CuCu collisions at $\sqrt{s_{NN}} = 22.4$ GeV [74], compared with previously published results from the STAR collaboration at 200 GeV and 62.4 GeV [94].

Figure 6.8 presents $v_2\{\text{TPC}\}$ for $0.1 < p_T < 2.0$ GeV/c and $|\eta| < 1.0$, as a function of centrality for charged hadrons from CuCu collisions at $\sqrt{s_{NN}} = 22.4$ GeV, plotted along with previously published results from the STAR collaboration at 200 GeV and 62.4 GeV [94]. The present result is obtained with the $v_2\{\text{TPC}\}$ method using η sub-events [74] with a gap of 0.3 units in pseudorapidity, while the prevously published results are based on the full TPC. The beam energy dependence of integrated v_2 mainly comes from the energy dependence of the mean p_T and the

difference between the event plane reconstruction with and without a pseudorapidity gap.

6.3 Systematic Uncertainties

For AuAu collisions at 7.7, 11.5, 19.6, 27 and 39 GeV, the non-flow correlations are highly suppressed in our $v_2\{\mathrm{BBC}\}$ method because of the large η gap between the TPC and BBC. Furthermore, we measure v_2 with respect to the first-order event plane, which suppresses contributions from flow fluctuations. Therefore these measurements are very similar to the results from the four-particle cumulant method. Estimated systematic uncertainty arising from event-plane flattening methods are found to be negligible (below 1%). An additional 5% systematic uncertainty is estimated by varying cut parameters (e.g. collision vertex position, the distance of closest approach of tracks to the primary vertex, and the number of fit points used for reconstruction of the tracks).

In CuCu collisions at 22.4 GeV, our measurements of elliptic flow are based on the TPC event plane, $v_2\{\mathrm{TPC}\}$. Unlike in the case of $v_2\{\mathrm{BBC}\}$, we do not have the advantage of a wide η gap to help ensure that non-flow background effects are minimized. To study possible systematic effects associated with short-range non-flow correlations, a four-particle cumulant [75] analysis $v_2\{4\}$ as a function of centrality has been investigated. This method suppresses non-flow correlations involving fewer than four particles. The statistical errors on our $v_2\{4\}$ measurements are small enough to be useful for the most central collisions, but grow to a few tens of percent at the other end of our studied centrality range. The $v_2\{\mathrm{TPC}\}$ and $v_2\{4\}$ measurements agree within statistical errors, although the observed systematic difference, which might arise from non-flow effects, amounts to about 9% for the

0–10% most central collisions. In the $v_2\{\mathrm{TPC}\}$ method, the η sub-event method with a gap of 0.3 units in pseudorapidity (η) has been used. Such a gap suppresses short-range correlations such as Bose-Einstein interference and Coulomb final-state interactions. To estimate the non-flow contributions to the measurement of $v_2\{\mathrm{TPC}\}$ due to these short-range correlations, a systematic study has been performed with variations in the resulting $v_2\{\mathrm{TPC}\}$ induced by varying the event vertex selection along the beam direction, by varying the DCA cut value, and by varying the size of the pseudorapidity gap between the sub-events in the η sub-event method. Tests of this type suggest that the systematic error on v_2 is on the order of 10% [74].

6.4 Summary

I presented measurements of elliptic flow, $v_2\{\mathrm{BBC}\}$, in AuAu collisions at $\sqrt{s_{NN}}$ = 7.7, 11.5, 19.6, 27 and 39 GeV for charged hadrons at mid-rapidity. I measured elliptic flow with respect to the first-order event plane reconstructed at larger rapidity. This method is effective in suppressing non-flow and flow fluctuation effects. The results from this method are consistent with the $v_2\{4\}$ method. This method is very helpful to estimate the systematic uncertainties from non-flow effects and flow fluctuations, by comparing these results to the other measurement methods like $v_2\{\mathrm{TPC}\}$ and 2-particle cumulant $v_2\{2\}$ methods, which are commonly used in elliptic flow analysis. The centrality, η and p_T dependence of v_2 are similar to those observed at higher RHIC beam energies. The integrated v_2 signal increases from central to mid central collisions, and it drops back down in peripheral collisions. The comparison with AuAu collisions at higher RHIC energies ($\sqrt{s_{NN}}$ = 62.4 and 200 GeV) and at LHC (PbPb collisions at $\sqrt{s_{NN}}$ = 2.76 TeV) shows that the v_2 values increase with increasing beam energy at low p_T ($p_T < 2.0$ GeV/c) where

hydrodynamic calculations are applicable.

Measurements of the elliptic flow for 22.4 GeV CuCu collisions are also presented. We compare p_T-integrated v_2 with measurements at higher energies. The p_T dependence of the measured v_2 at 22.4 GeV is similar to that at 62.4 and 200 GeV. Comparisons with UrQMD and AMPT models (the latter both with and without string melting) do not agree with the present measurements [74].

Chapter 7

RESULTS – III: TRIANGULAR FLOW

In this chapter, I present the third harmonic coefficient for azimuthal anisotropy, popularly known as triangular flow, for charged particles as a function of pseudo-rapidity, transverse momentum and centrality, for AuAu collisions at $\sqrt{s_{NN}} = 200$ GeV, based on data taken in 2004 (run IV). Triangular flow is a relatively new observable and provides extra information concerning initial-state fluctuations, and the subsequent evolution of the collision system [20, 43].

7.1 Centrality dependence

Figure 7.1 shows the width and amplitude of the wide Gaussian (introduced in Chapter 4) as a function of centrality on the left, and as a function of p_T for centralities 0–5% and 30–40% on the right. Above $p_T = 0.8$ GeV/c, the distribution can be described by a single wide Gaussian. The amplitude increases with p_T and then saturates around $p_T = 3$ GeV/c. The p_T dependence of the width seems to depend on centrality, with the 0–5% most central data showing first an increase and then a gradual decrease, while at 30–40% centrality, the data appear to gradually decrease for all p_T.

The Fig. 7.2, left panel, shows the centrality dependence for p_T-integrated v_3 from several different analyses: two-particle cumulants with a minimum pseudorapidity separation of one unit between particles, $v_3\{2\}$ evaluated using the wide Gaussian

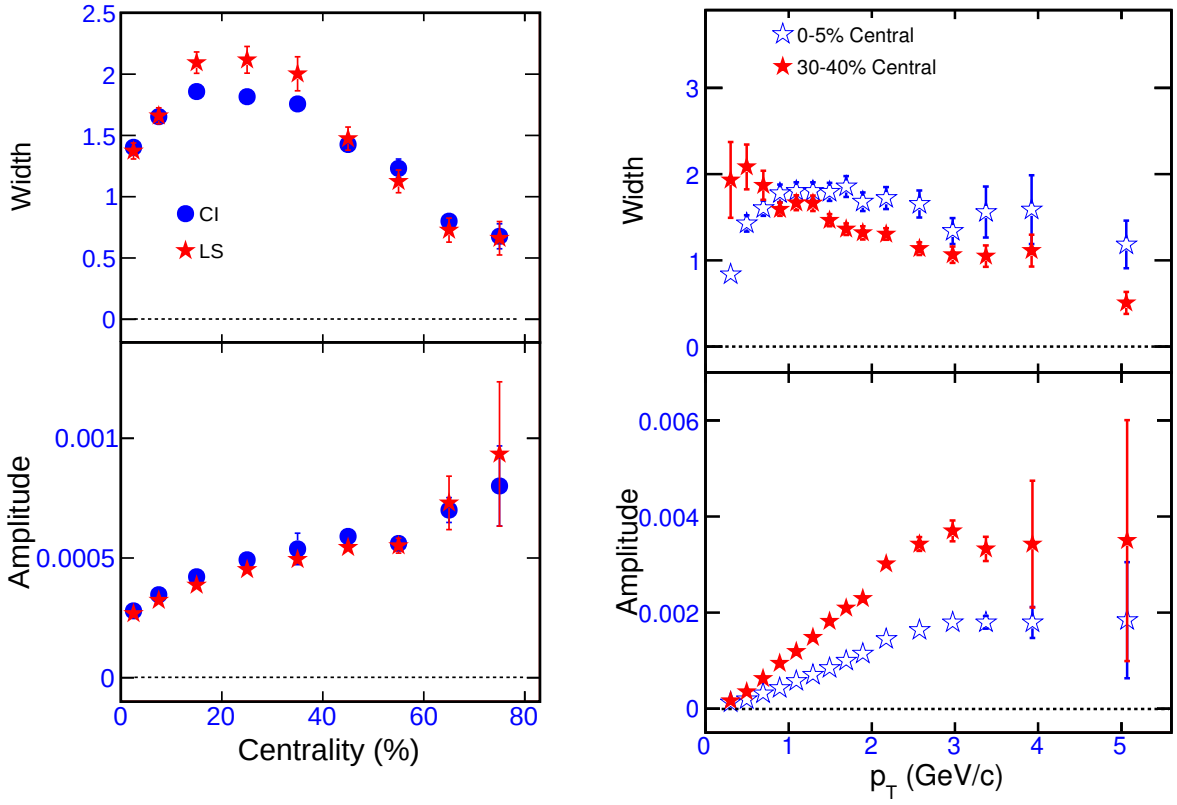

Figure 7.1: The two panels on the left show the width and amplitude of the wide Gaussian as a function of centrality for charge-independent (CI) and like-sign (LS) particles. The two panels on the right show the same width and amplitude as a function of transverse momentum for most central (0–5%) and for mid-central (30–40%) collisions. The plotted errors are statistical, and all cases are for $\sqrt{s_{NN}}$ = 200 GeV AuAu events.

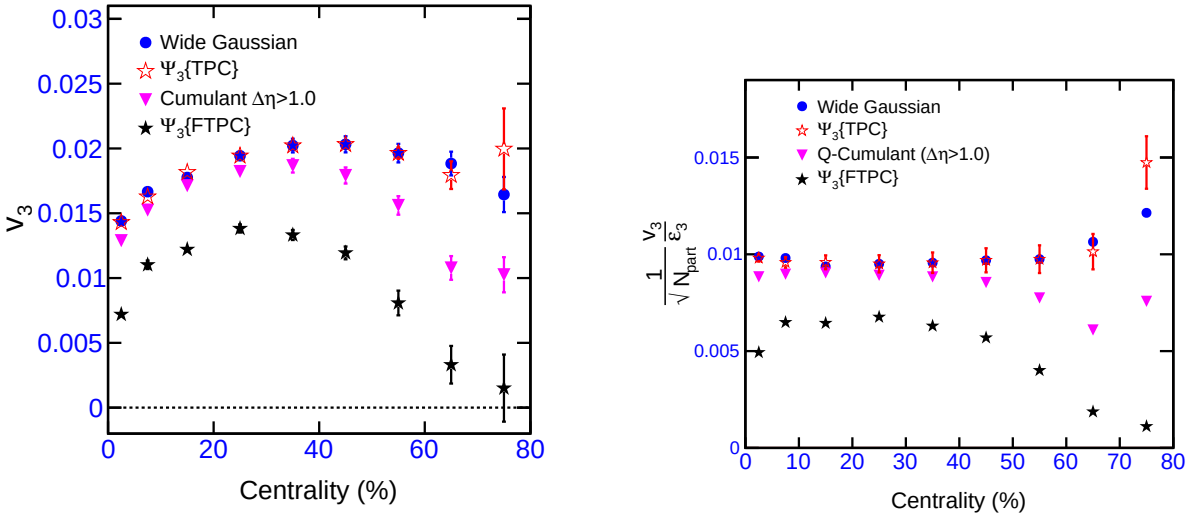

Figure 7.2: The third harmonic coefficient as a function of centrality from different methods of measurement for Au+Au collisions at $\sqrt{s_{NN}}$ = 200 GeV, with track selections $0.15 < p_T < 2.00$ GeV/c and $|\eta| < 1.0$ in the left panel, and the ratio of v_3 to the third harmonic participant eccentricity ε_3 [99] scaled by $1/\sqrt{N_{\rm part}}$ in the right panel.

parameters, $v_3\{\mathrm{TPC}\}$ and $v_3\{\mathrm{FTPC}\}$ where v_3 is measured relative to the third-harmonic event plane reconstructed either in the TPC or the FTPCs. Figure 7.2, right panel, shows the ratio of v_3 to the third harmonic participant eccentricity ε_3 [99] scaled by $1/\sqrt{N_{\rm part}}$. This assumes that $v_3 \sim \varepsilon_3$ with a proportionality constant that includes $1/\sqrt{N_{\rm part}}$. $N_{\rm part}$ and ε_3 are calculated using a Monte Carlo Glauber model [17]. Three of the curves agree well up to moderate centralities, but the case where the event plane comes from the FTPC does not.

7.2 $\Delta\eta$ dependence

The $\Delta\eta$ dependence of v_3 is shown in Fig. 7.3. This dependence may have its origin in a decrease in non-flow correlations with increasing $\Delta\eta$ separation, or in initial-state fluctuations decreasing with large $\Delta\eta$, or possibly both effects

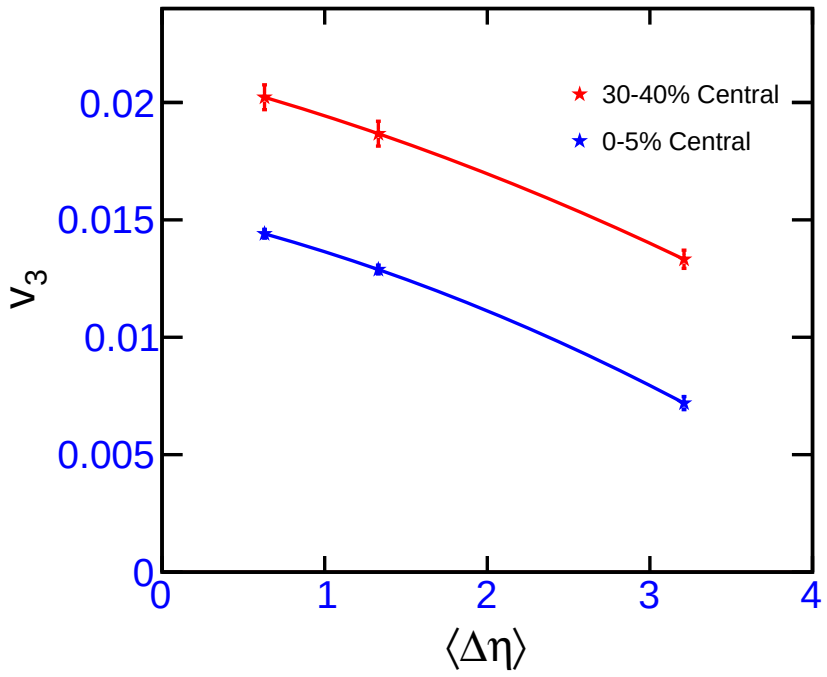

Figure 7.3: The third harmonic coefficient as a function of mean $\Delta\eta$. The points at $\Delta\eta = 0.63$ are from the method using the TPC with $|\eta| < 1$. The points at $\Delta\eta = 1.33$ are from the cumulant with $|\Delta\eta| > 1$. The points at $\Delta\eta = 3.21$ are from correlations using the FTPC event plane.

may contribute. If $v_3^2\{2\}$ is related to the initial eccentricity fluctuations, then the reduction of $v_3^2\{2\}$ at large $\Delta\eta$ would presumably require a decrease of the initial-state fluctuations at large rapidity separations. Recent work has found such a decoherence effect with a hadron and parton cascade model [106]. Thus it is not clear if one should extrapolate to large $\Delta\eta$ to avoid non-flow, or to small $\Delta\eta$ to measure all the fluctuations [106]. More theoretical input is necessary to advance our understanding of the $\Delta\eta$ dependence of this signal.

7.3 η and p_T dependence

Figure 7.4 shows the η dependence of v_3 using event plane methods. For particles in the TPC using the η sub-event method, v_3 is somewhat peaked at mid-rapidity in peripheral collisions. With the event plane in the FTPCs, there is a large η gap and v_3 is flat at all centralities. This suggests that acceptance effects at the edges of the TPC are not important. Thus, even though a large $\Delta\eta$ means that one of the particles is probably at large η, this evidently does not have a large effect on the η dependence of the signal. Figure 7.5 shows the third harmonic coefficient as a function of p_T at different centralities for AuAu collisions at $\sqrt{s}_{NN}$= 200 GeV, measured with respect to the event planes constructed either in the TPC or FTPCs. The average $\Delta\eta$ is 0.63 using the TPC event plane, and is 3.21 using the FTPC event plane. The difference between the two methods can be understood in terms of a $\Delta\eta$ dependence of the signal.

7.4 Comparisons with other experiments

In Fig. 7.6, it is evident that STAR v_3 results with the event plane from the TPC are very similar to those of PHENIX [101]. This is surprising, because the

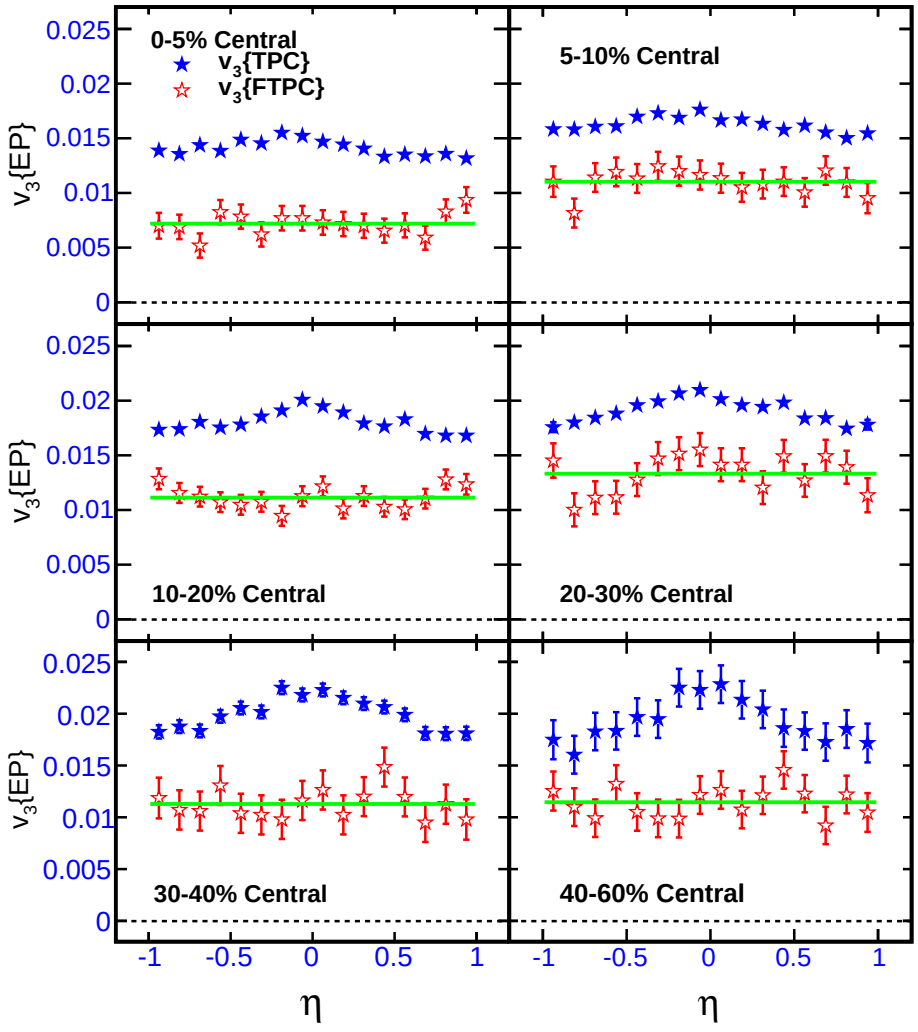

Figure 7.4: The third harmonic coefficient as a function of η at different centralities for AuAu collisions at $\sqrt{s_{NN}}$= 200 GeV, measured with respect to the event planes constructed either in the TPC or FTPCs.

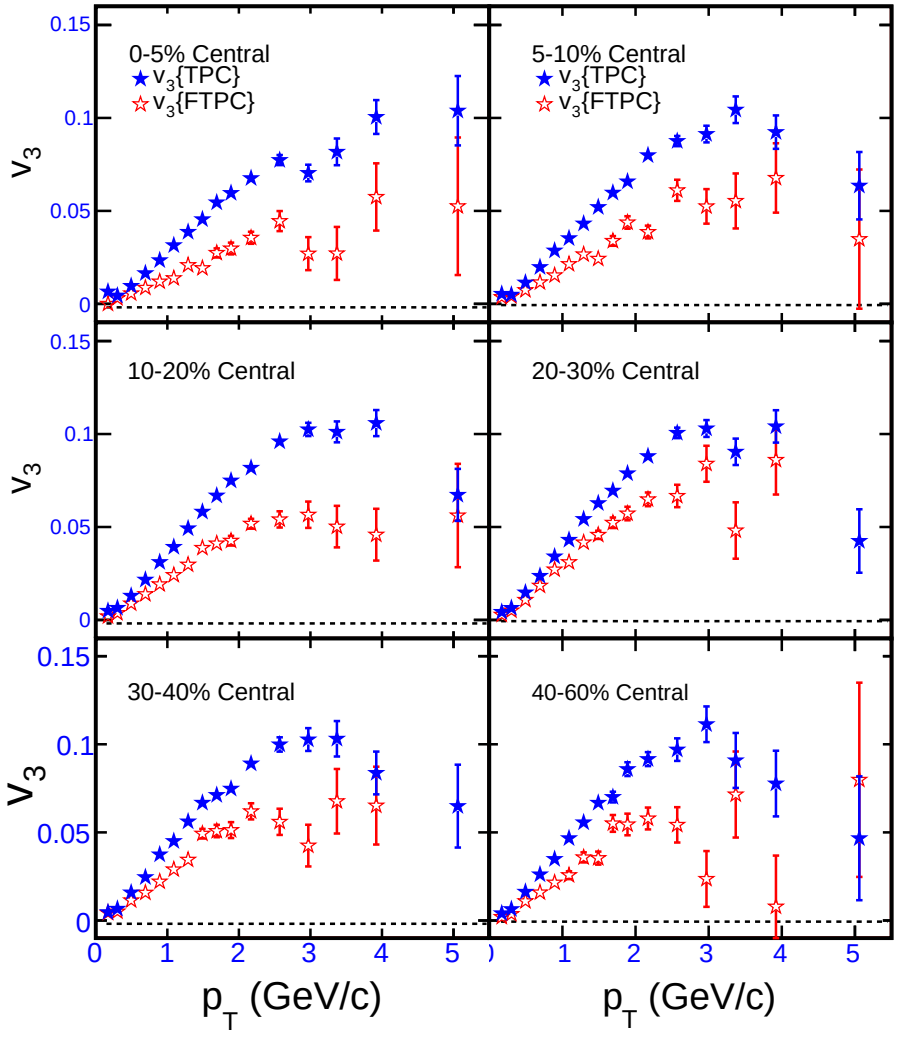

Figure 7.5: The third harmonic coefficient as a function of p_T at different centralities for AuAu collisions at $\sqrt{s}_{NN}$= 200 GeV, measured with respect to the event planes constructed either in the TPC or FTPCs.

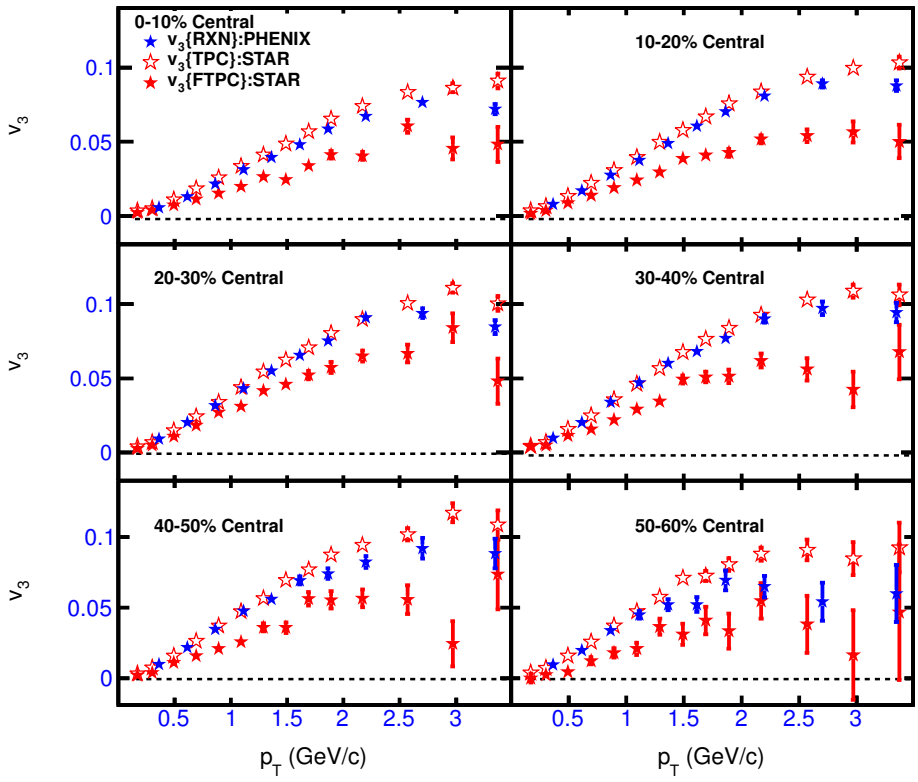

Figure 7.6: The third harmonic coefficient as a function of p_T for both event plane methods at different centralities, compared to results from the PHENIX experiment [101]. The PHENIX pseudorapidity selection is $|\eta| \leq 0.35$ while for STAR, it is $|\eta| \leq 1.0$. For the STAR results from the TPC, the mean $\Delta\eta$ was 0.63, whereas using the FTPC event plane, the average $\Delta\eta$ was 3.21. The PHENIX results used the event plane from their RXN detector at an intermediate η, namely $1.0 < \eta < 2.8$.

mean η of their RXN detector is larger than the same for sub-events in the STAR TPC. Our FTPC results are lower than the PHENIX v_3 measurements. This is expected, because the mean $\Delta\eta$ is considerably larger in the STAR FTPC than in the PHENIX RXN detector.

7.5 Model Comparisons

Event-by-event ideal hydro calculations of v_3 have been reported by Qiu and Heinz [103]. These authors concluded that instead of averaged initial conditions, event-by-event calculations are necessary to compare with experimental data. The first prediction of v_3 with viscous hydro was in Ref. [46]. In Fig. 7.7, v_2 and v_3 as a function of transverse momentum are compared with several models for 0–5% and 30–40% central collisions. The specific models are the viscous hydrodynamic model of Ref. [45], where the ratio of viscosity to entropy is $\eta/S = 0.08$ and 0.16, and the AMPT model [**?**]. Predictions of v_3 from the Parton-Hadron-String Dynamics model [105] at 30–40% centrality for $|\eta| < 0.5$ have been reported using the sub-event method with the event planes at $1.0 < |\eta| < 4.0$, and are also plotted in Fig. 7.7, at the lower right.

Elliptic flow results are mostly described by ideal hydrodynamics in the case of the most central collisions, and by $\eta/S = 0.08$ in the case of mid-central collisions. We find that the third harmonic coefficient results are also described by the same model with similar viscosities. The PHSD model [105] also agrees with data.

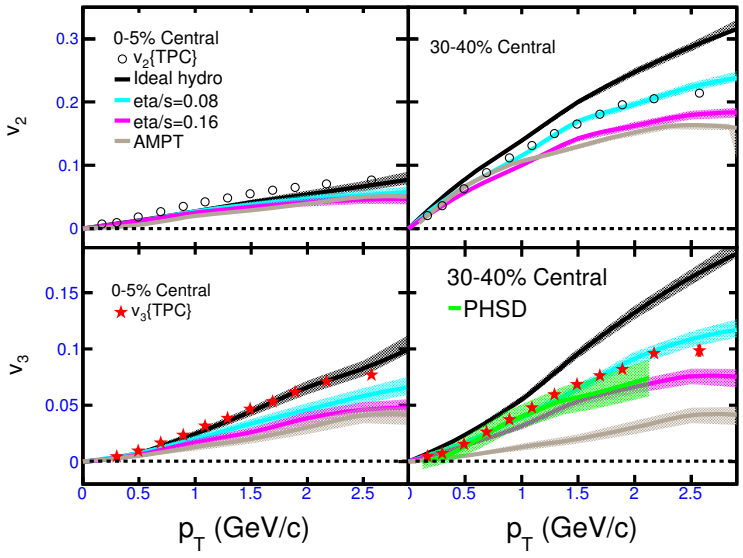

Figure 7.7: v_2 (top) and v_3 (bottom) for Au+Au collisions at $\sqrt{s_{NN}} = 200$ GeV in 0–5% and 30–40% central collisions as a function of transverse momentum, compared with ideal [46] and viscous [45] hydro, AMPT transport [**?**], and Parton-Hardon-String Dynamics [105] models. The STAR v_2 values (top) come from Ref. [95].

7.6 Systematic Uncertanities

Results are plotted showing statistical errors only. In these studies, contributions from short-range correlation such as Bose-Einstein correlations and Coulomb interactions are suppressed using a pseudorapidity gap of at least 0.5 units between the event vector and the particle of interest, and a gap of one unit in pseudorapidity between the two sub-event vectors. Furthermore, we used a transverse momentum weight only up to 2 GeV/c, and a constant weight thereafter, which reduces the possible influence of jet/minijets at higher transverse momentum. The remaining non-flow contribution from jets/minijets is unknown and might be a significant contributor to the systematic uncertainties, especially in peripheral collisions. We estimate systematic uncertainty by changing event and track quality cuts from their

central values. The total systematic uncertainty is evaluated by adding the uncertainties measured in different cases in quadrature. Based on the factors mentioned above, the resulting error estimate is about 10%, but this does not include the unknown jet/minijet contribution.

7.7 Summary

I presented measurements of triangular flow of charged particles from Au+Au collisions at $\sqrt{s}_{NN}$ = 200 GeV as a function of pseudorapidity, transverse momentum, and centrality. Short-range correlations are eliminated by an η gap or by eliminating the narrow Gaussian in pseudorapidity separation. Results are reported based on a two-particle method for particle pairs, fitted with a wide Gaussian in pseudorapidity separation, as well as from the standard event-plane method at mid-rapidity or at forward rapidity. The measured values of v_3 continuously decrease as mean $\Delta\eta$ increases. It is not know whether this decrease is due to a decrease in non-flow correlations or a decrease in fluctuations.

It is observed that v_3 increases with transverse momentum before it levels-off between 2 and 3 GeV$/c$, similar to the case of elliptic flow. We observe that the ratio of v_3 to ϵ_3 is almost linear, except for the case when the event plane is derived from the FTPCs. This observation supports the view that v_3 originates from initial-state density fluctuations. Our results are mostly described by hydrodynamic models with small viscosity.

Chapter 8

RESULTS – IV: DIPOLE ASYMMETRY

In this chapter, I present measurements of azimuthal anisotropy at mid-rapidity originating from dipole asymmetry in AuAu collisions at $\sqrt{s_{NN}} = 200$ GeV. With this type of observable, conventional rapidity odd directed flow is suppressed and momentum conservation effect is corrected, leaving only a correlation which can be attributed to fluctuations in the initial geometry. This measurement is a first-harmonic flow coefficient, and is reported as a function of pseudorapidity and transverse momentum for different centralities. The dataset under investigation comes from run IV (from the year 2004). This is the first measurement of this new observable at RHIC, and it provides an additional way to study initial-state fluctuations, and the subsequent evolution of the collision system [43].

8.1 Pseudorapidity Dependence

Figure. 8.1 presents the first flow harmonic associated with dipole asymmetry in AuAu collisions at $\sqrt{s_{NN}} = 200$ GeV as a function of η. Each panel corresponds to a different centrality, ranging from 0–5% through 70–80%. As explained in Ref. [44], not much η dependence is expected, which our measurements confirm for central collisions. However, in more peripheral collisions, much increased η dependence is observed, which might be a viscous effect and/or may arise from non-flow correlations. We are not aware of any pertinent model calculations, and future theoretical study may shed light on it.

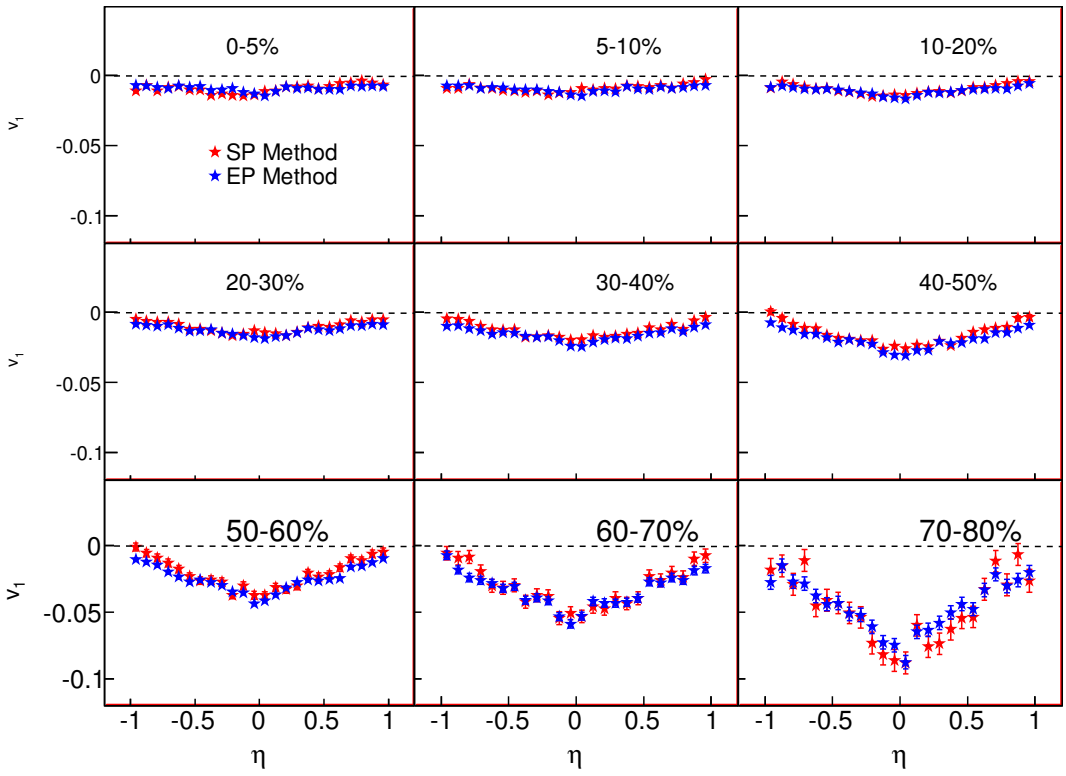

Figure 8.1: First flow harmonic associated with dipole asymmetry, from central to peripheral collisions of 200 GeV AuAu, as a function of pseudorapidity (η).

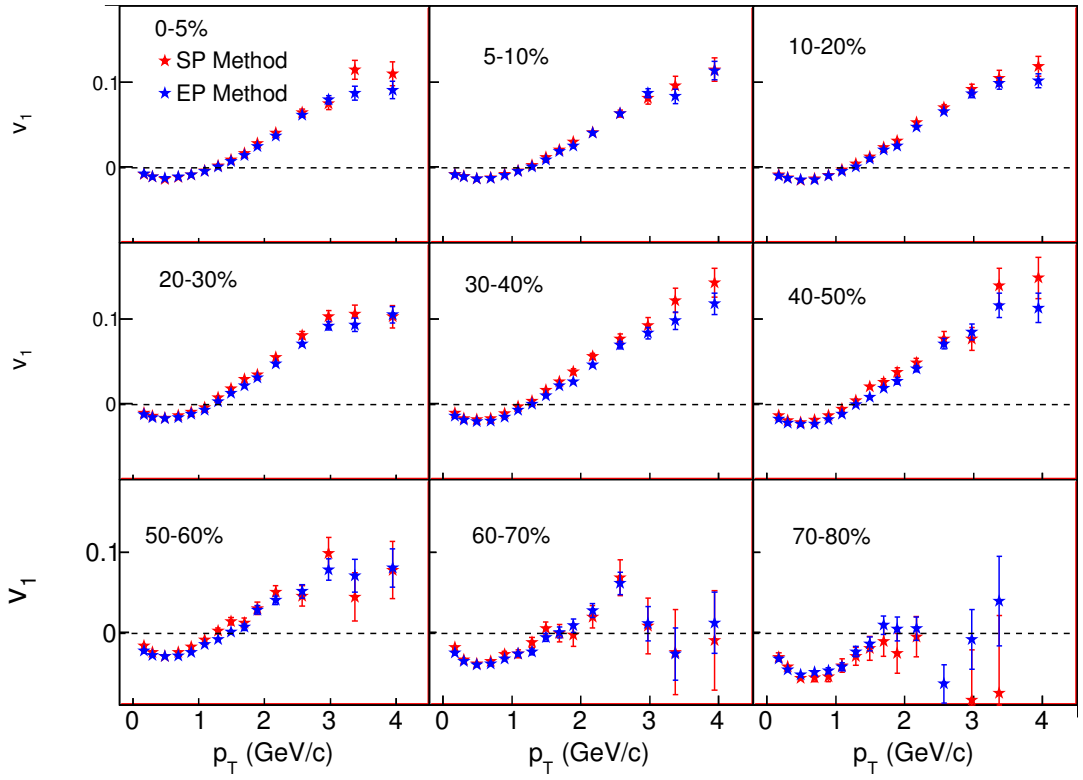

Figure 8.2: First flow harmonic associated with dipole asymmetry, from central to peripheral collisions of 200 GeV AuAu, as a function of transverse momentum. Two analysis methods are shown — the standard event-plane method and the scalar product method.

8.2 Transverse Momentum Dependence

Figure 8.2 presents the first flow harmonic associated with dipole asymmetry in AuAu collisions at $\sqrt{s_{NN}} = 200$ GeV as a function of p_T. Each panel corresponds to a different centrality, ranging from 0–5% through 70–80%. Recently, the ATLAS collaboration has released their measurement of a similar observable [110]. They used two-particle correlation data and employed a two-component fit ansatz to separate this signal from the background due to momentum conservation. STAR and ATLAS results are quite close.

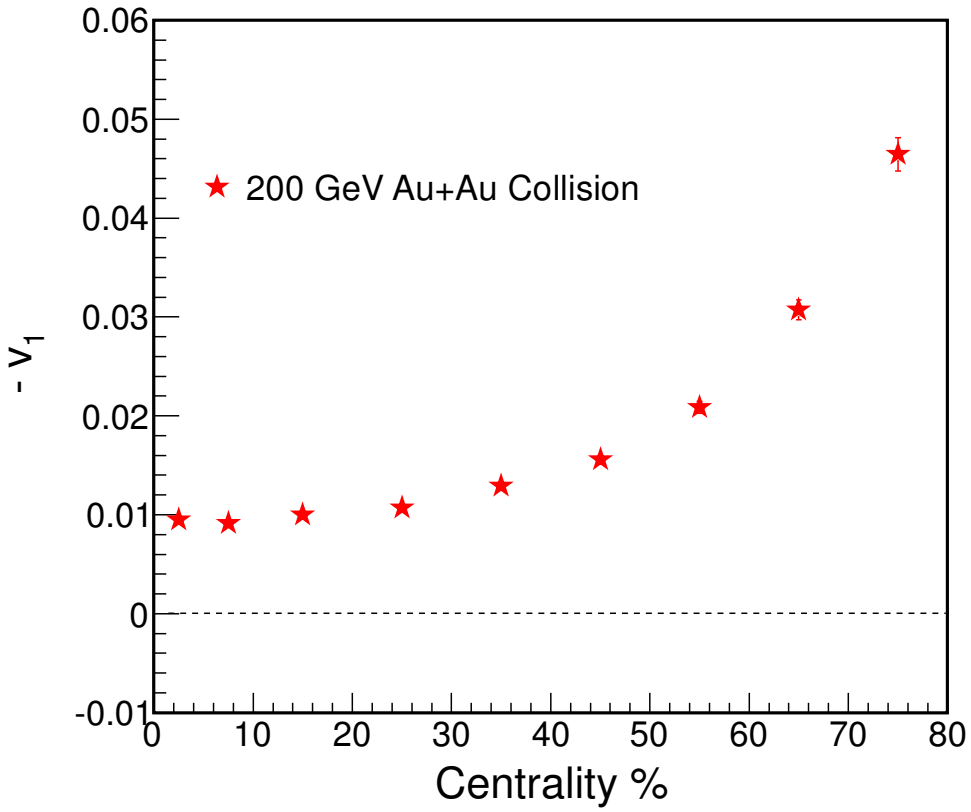

Figure 8.3: Centrality dependence of integrated ($|\eta| < 1$ and $0.15 < p_T < 2.00$ GeV/c) directed flow associated with dipole asymmetry.

8.3 Centrality Dependence

In Fig. 8.3, the integrated ($|\eta| < 1$ and $0.15 < p_T < 2.00$ GeV/c) first flow harmonic signal associated with dipole asymmetry is plotted for AuAu collisions at $\sqrt{s_{NN}} = 200$ GeV as a function of centrality. As expected from model calculations [44, 109], the centrality dependence is weak up to mid-central collisions, but grows stronger in peripheral collisions.

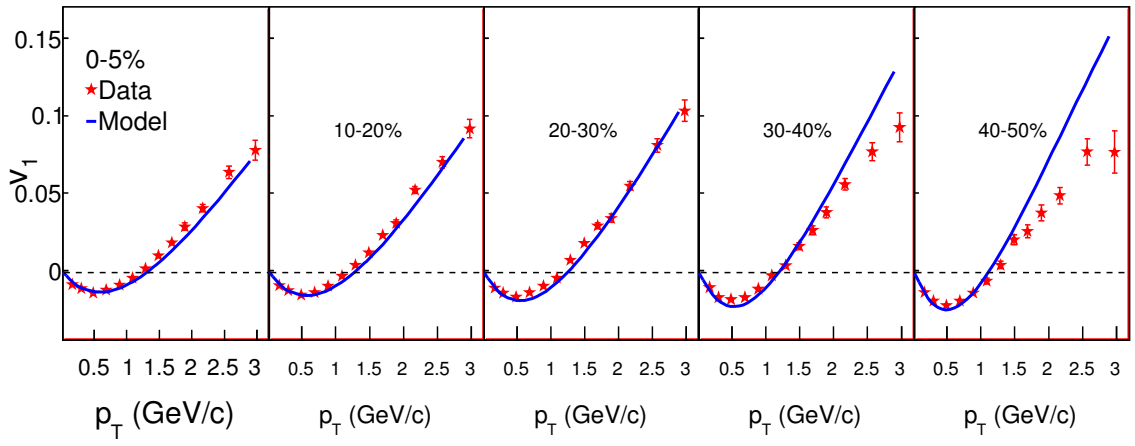

Figure 8.4: Transverse momentum dependence of dipole asymmetry in 200 GeV AuAu collisions, compared with a hydrodynamic model [109].

8.4 Model Comparisons

Figure 8.4 presents the first flow harmonic associated with dipole asymmetry in AuAu collisions at $\sqrt{s_{NN}} = 200$ GeV as a function of p_T, compared to the hydrodynamic model of Retinskaya, Luzum, and Ollitrault [109]. Each panel corresponds to a different centrality, ranging from 0–10% through 40–50%. The hydrodynamic calculations incorporate viscous corrections, where the ratio of viscosity to entropy is $\eta/s = 0.16$. In central collisions and at low values of transverse momentum, these model predictions describe the data very well. However they deviate in peripheral collisions and at higher values of transverse momentum.

8.5 Systematic Uncertainties

Short-range correlations such as Bose-Einstein correlations, Coulomb interactions, and correlations from resonances are the main source of non-flow correlations. Some of these are suppressed by the η sub-event method with a small gap. Non-flow

originating from jets/minijets [111] cannot be estimated. We use a constant weighting factor of 2 GeV/c for all particles with $p_T > 2$ GeV/c, which reduces the possible influence from high transverse momentum jets/minijets. We estimate the systematic uncertainty by means of changing event and track quality cuts from the optimal values. The total systematic uncertainty is evaluated by adding the uncertainties from the different sources in quadrature, which leads to an estimated overall systematic error of about 10%.

8.6 Summary

The first measurements of the first harmonic coefficient associated with dipole asymmetry in Au + Au collisions at $\sqrt{s_{NN}} = 200$ GeV are presented. Results are reported using the the standard event-plane method and the scalar product method, with the flow vectors reconstructed with a pseudorapidity gap of 0.1 units between the sub-event vectors, and at least 0.05 units of pseudorapidity between the flow vector and the particle of interest. Results from both methods are consistent with each other. It is observed that the centrality dependence of this flow is weak up to mid-central collisions, and there is a large change in centrality dependence thereafter, which may come from non-flow or from imperfect correction for the unwanted correlation from momentum conservation. Recently, the ATLAS collaboration has released their dipole asymmetry measurement at LHC energy. They used two-particle correlation data and employed a two-component fit ansatz to separate the pseudorapidity-even first harmonic coefficient from the signal due to momentum conservation. The results presented here are quite similar to the ATLAS results, and are mostly described by hydrodynamic models with a small viscosity for central collisions, however, the models deviate from the data in peripheral collisions

at higher values of transverse momentum.

Chapter 9

SUMMARY AND CONCLUSIONS

Anisotropic flow sheds light on the early stage in high-energy heavy-ion collisions. To minimize various systematic effects, especially the correlations that in practice set a limit on how accurately flow can be measured, we have used a detector subsystem called Beam Beam Counters (BBC) and developed a new method to reconstruct the reaction plane from the energy deposition of the charged particles collected by the BBC. This work focuses on the contribution of the BBC to the estimation of the first-order event plane used in anisotropic flow analysis at Beam Energy Scan (BES) energies ($\sqrt{s}_{NN}$ = 7.7, 11.5, 19.6, 27 and 39 GeV). This new method $v_n\{\mathrm{BBC}\}$ has proven itself to be reliable as evidenced by the agreement with other independent methods, and is useful to suppress non-flow, because of the large pseudorapidity gap between the BBCs and the central TPC. The first-order event plane resolution is a quality factor such that unity represents a perfect reaction plane determination. The event plane resolution is calculated by correlating east and west BBC event planes. This resolution has a centrality dependence which reaches a maximum around mid-central collisions, and also has a beam energy dependence which decreases with increasing beam energy.

In the directed flow analysis, I studied all charged particles as well as identified pions $(\pm)$, kaons $(\pm)$, protons and antiprotons in 7.7, 11.5, 19.6, 27 and 39 GeV AuAu collisions. For CuCu collisions at 22.4 GeV and AuAu collisions at 9.2 GeV, I studied directed flow for charged particles. Because of limited statistics, I was

not able to study identified particle flow at 22.4 and 9.2 GeV. I studied the flow of charged particles in the pseudorapidity region covered by the STAR TPC and FTPCs (up to η = 4.2) and for identified charged particles in the pseudorapidity region covered by the STAR TPC.

I observed that charged particle v_1 approaches zero close to the spectator rapidities. This is an unremarkable effect predicted by all models, and can be understood in terms of a change in the relative abundances of protons and pions at forward pseudorapidities, where proton v_1 and pion v_1 likely have opposite signs, but neither might have a wiggle shape. The rapidity dependence of v_1 provides further support for the limiting fragmentation picture in AuAu collisions as well as in CuCu collisions.

Directed flow of identified particles is reported. Differences in directed flow are observed between between positive and negative hadrons, and especially between protons and antiprotons. This difference becomes smaller for higher beam energies. For mid-central collisions, the proton v_1 slope in the mid-rapidity region changes sign from positive to negative between 7.7 and 11.5 GeV and remains small but negative up to 200 GeV, while the slope for pions, kaons and antiprotons and remains always negative. Based on transport model comparisons, the observed trends in these data above 11.5 GeV can qualitatively be understood in terms of anisotropic emission of produced particles from a tilted disk. A striking observation is that the v_1 slope for net protons, which is an estimate of the directed flow contribution from initial-state baryon number transported to the midrapidity region, changes sign twice within the energy range 7.7–39 GeV studied here. This result is qualitatively different from the UrQMD transport model, which exhibits a monotonic trend with

no sign reversal, and has the potential to be the most unexpected and far-reaching finding to emerge from this dissertation project. It is also noteworthy that a three-fluid hydrodynamic model with a first-order phase transition [89] predicts a double sign change that is qualitatively very similar to the STAR measurement. However, the ultimate implication of this observation will most likely not be understood until theoretical study with a specific focus on this signal has been completed, as well as a new experimental study with higher statistics required for a measurement as a function of centrality.

I measured the elliptic flow, v_2, in AuAu collisions at $\sqrt{s_{NN}}$ = 7.7, 11.5, 19.6, 27 and 39 GeV for charged hadrons at mid-rapidity with respect to the first-order event plane reconstructed at larger rapidity. This method is effective in suppressing non-flow and flow fluctuation effects. The results from this method are consistent with the $v_2\{4\}$ method. Comparing these results to the other measurement methods like $v_2\{\mathrm{TPC}\}$ and the two-particle cumulant $v_2\{2\}$ methods which are commonly used in elliptic flow analysis, one can estimate the systematic uncertainties from non-flow effects and flow fluctuations. The centrality, η and p_T dependence of v_2 are similar to those observed at higher RHIC beam energies. The integrated v_2 signal increases from central to mid-central collisions, and it decreases in peripheral collisions. The comparison with Au+Au collisions at higher RHIC energies ($\sqrt{s_{NN}}$ = 62.4 and 200 GeV) and at LHC (PbPb collisions at $\sqrt{s_{NN}}$ = 2.76 TeV) shows that the v_2 values increase with increasing beam energy at low p_T ($p_T < 2.0$ GeV/c) where hydrodymanic calculations are applicable.

Measurements of the elliptic flow for 22.4 GeV CuCu collisions are also presented. We compare p_T-integrated v_2 with measurements at higher energies. The

p_T-dependence of the measured v_2 at 22.4 GeV is similar to that at 62.4 and 200 GeV. UrQMD and AMPT models (the latter both with and without string melting) do not agree with the present measurements.

In triangular flow analysis, I concentrated on AuAu collisions at $\sqrt{s}_{NN} = 200$ GeV from the year 2004 (run 4). I present measurements of triangular flow of charged particles as a function of pseudorapidity, transverse momentum, and centrality. I report result from a two-particle method for particle pairs fit with a wide Gaussian in pseudorapidity separation, as well as from the standard event-plane method at mid-rapidity or at forward rapidity. The measured values of v_3 continuously decrease as mean $\Delta\eta$ increases. It is not known whether this decrease is due to a decrease in non-flow correlations or a decrease in fluctuations. We observe that v_3 increases with transverse momentum before it levels-off between 2 and 3 GeV$/c$, similar to the case of elliptic flow. Our results are mostly described by hydrodynamic models with small viscosity. It is observed that the ratio of v_3 to ϵ_3 is almost linear, except for the case with the event plane in the FTPCs. This observation supports the view that v_3 originates from initial-state density fluctuations.

I presented the first measurements of the first harmonic coefficient associated with dipole asymmetry from AuAu collisions at $\sqrt{s_{NN}} = 200$ GeV. I report results from the standard event plane method and the scalar product method, with the flow vectors reconstructed with a pseudorapidity gap of 0.1 units between the sub-event vectors, and at least 0.05 units of pseudorapidity between the flow vector and the particle of interest. Results from both methods are consistent with each other. It is observed that the centrality dependence of this flow is weak up to mid-central collisions, and there is a large change in centrality dependence thereafter, which may

come from non-flow or non-perfect correction for momentum conservation. These results are mostly described by hydrodynamic models with a small viscosity for central collisions. However, the models deviate from the data in peripheral collisions at higher transverse momentum. Measurements related to initial density fluctuations are a new area of physics analysis in STAR, and they help us to understand the collision dynamics.

There is general agreement in the heavy-ion collision community that a new form of matter is being produced at the top RHIC energy, and that it has many of the characteristics expected of a strongly-interacting Quark-Gluon Plasma (sQGP). We are now in the follow-on stage of studying the properties of this new phase of matter, and STAR has now progressed to the stage of mapping the evolution of these properties with beam energy. During the beam energy scan program at RHIC, we are looking for the disappearance of the QGP signatures observed at top RHIC energy. We also are searching for signatures of the hypothesized critical point and first-order phase boundary. The RHIC energy scan program is in its first phase. I have presented some interesting experimental observations and new theoretical input is necessary to fully understand these observations. Elliptic flow study with respect to the first-order event plane certainly helps to disentangle the flow from non-flow and flow fluctuations. We are now just beginning to study triangular flow and first flow harmonics due to dipole asymmetry at RHIC, one of the main topics of this dissertation. Therefore, we emphasize that it is too early to expect this work to have well-understood consequences for the "big picture" at RHIC, and in the meantime, I make the argument that the analyses in this dissertation have strongly challenged the theoretical community, especially in the area of directed flow for transported

baryon number. Moreover, this work has paved the way for the next rounds of experimental analyses.

Bibliography

[1] *Quark-Gluon Plasma 3*, edited by R. C. Hwa and X. N. Wang, World Scientific, Singapore (2003).

[2] *Introduction to High-Energy Heavy-Ion Collisions*, C.-Y. Wong, World Scientific, Singapore (1994).

[3] For recent developments, see Proceedings of Quark Matter 2011, Annecy, France, J. of Phys. G **38** (2011).

[4] K. Geiger, Phys. Rev. D **46**, 4965 (1992).

[5] Y. Aoki *et al.*, Nature **443**, 675 (2006); Y. Aoki *et al.*, Phys. Lett. B **46**, 643 (2006); M. Cheng *et al.*, Phys. Rev. D **74**, 054507 (2006).

[6] F. R. Brown *et al.*, Phys. Rev. Lett. **65**, 2491 (1990); A. Bazavov *et al.* (HotQCD Collaboration), Phys. Rev. D **80**, 014504 (2009); S. Borsanyi *et al.* (Wuppertal-Budapest Collaboration), J. High Energy Phys. **11**, 077 (2010).

[7] S. Ejiri, Phys. Rev. D **78**, 074507 (2008); E. S. Bowman, J. I. Kapusta, Phys. Rev. C **79**, 015202 (2009); Y. Hatta and T. Ikeda, Phys. Rev. D **67**, 014028 (2003).

[8] B. I. Abelev *et al.* (STAR Collaboration), arXiv:1007.2613.

[9] The Phenix Collaboration: http://www.phenix.bnl.gov .

[10] A. Aduszkiewicz, Acta Phys. Polonica B **43**, 635 (2012).

[11] P. Staszel (for the CBM Collaboration), Acta Phys. Polonica B **41**, 2 (2010).

[12] The NICA Collaboration: http://nica.jinr.ru .

[13] B. I. Abelev *et al.* (STAR Collaboration), Phys. Rev. C **81**, 24911 (2010).

[14] A. M. Poskanzer and S. A. Voloshin, Phys. Rev. C **58**, 1671 (1998).

[15] B. I. Abelev *et al.* (STAR Collaboration), Phys. Rev. Lett. **99**, 112301 (2007); J. Adams *et al.* (STAR Collaboration), Phys. Rev. Lett **95**, 122301 (2005).

[16] M. H. Thoma and M. Gyulassy, Nucl. Phys. A **538**, 37c (1991); S. Mrowczynski, Phys. Lett. B **269**, 383 (1991); Y. Koike and T. Matsui, Phys. Rev. D **45**, 3237 (1992); M. Gyulassy and M. Plumer, Phys. Lett. B **243**, 432 (1990).

[17] M. L. Miller, K. Reygers, S. J. Sanders and P. Steinberg, Ann. Rev. Nucl. Part. Sci. **57**, 205 (2007); B. Alver *et al.*, Phys. Rev. C **77**, 014906 (2008).

[18] B. I. Abelev *et al.* (STAR Collaboration), Phys. Rev. C **80**, 064912 (2009).

[19] S. Gavin and G. Moschelli, Phys. Rev. C **85**, 014905 (2012); A. Dumitru, F. Gelis, L. McLerran, and R. Venugopalan, Nucl Phys. A **810**, 91 (2008); S. Gavin, L. McLerran, and G. Moschelli, Phys. Rev. C **79**, 051902 (2009); G. Moschelli and S. Gavin, Nucl. Phys. A **836**, 43 (2010); K. Dusling, D. Fernandez-Fraile, and R. Venugopalan, Nucl. Phys. A **828**, 161 (2009).

[20] B. Alver and G. Roland, Phys. Rev. C **81**, 054905 (2010).

[21] P. Sorensen, B. Bolliet, A. Mocsy, Y. Pandit and N. Pruthi, Phys. Lett. B **705**, 71 (2011).

[22] B. I. Abelev *et al.*, Phys. Rev. Lett. **103**, 251601 (2009).

[23] S. A. Voloshin, Phys. Rev. C **70**, 057901 (2004).

[24] J. Brachmann, S. Soff, A. Dumitru, H. Stöcker, J. A. Maruhn, W. Greiner, L. V. Bravina, and D. H. Rischke, Phys. Rev. C **61**, 024909 (2000); L. P. Csernai and D. Roehrich, Phys. Lett. B **458**, 454 (1999); M. Bleicher and H. Stöcker, Phys. Lett. B **526**, 309 (2002).

[25] T. Csorgo, PoS CPOD2009, 035 (2009) (arXiv:0911.5015v1 [nucl-th])

[26] C. Athanasiou, K. Rajagopal and M. Stephanov, Phys. Rev. D **82**, 074008 (2010).

[27] M. A. Stephanov, Phys. Rev. Lett. **102**, 032301 (2009).

[28] J. Adams *et al.* (STAR Collaboration), Phys. Rev. C **72**, 044902 (2005).

[29] M. A. Stephanov, Phys. Rev. Lett. **102**, 032301 (2009).

[30] X. F. Luo for the STAR Collaboration, J. Phys. Conf. Ser. **316**, 012003 (2011).

[31] R. Hanbury-Brown and R. Q. Twiss, Phil. Mag. **45**, 663 (1954); S. E. Koonin, Phys. Lett. B **70**, 43 (1977); F. B. Yano and S. E. Koonin, Phys. Lett. B **78**, 556 (1978); S. Pratt, Phys. Rev. Lett. **53**, 1219 (1984); S. Pratt, Phys. Rev. D **33**, 1314 (1986); U. Heinz, Nucl. Phys. A **610**, 264c (1996).

[32] M. A. Lisa and S. Pratt, arXiv:0811.1352.

[33] N. Herrmann, J. P. Wessels, and T. Wienold, Annu. Rev. Nucl. Part. Sci. **49**, 581 (1999); M. Bleicher and H. Stöcker, Phys. Lett. B **526**, 309 (2002); J. Y. Chen *et al.*, Phys. Rev. C **81**, 014904 (2010).

[34] P. Huovinen in *Quark-Gluon Plasma 3*, Eds: R. C. Hwa, X. N. Wang (World Scientific, Singapore, 2003), p. 616.

[35] J . Adams *et al.* (STAR Collaboration), Phys. Rev. Lett. **101**, 252301 (2008).

[36] P. Bozek and I. Wyskiel, Phys. Rev. C **81**, 054902 (2010).

[37] R. J. Snellings, H. Sorge, S. A. Voloshin, F. Q. Wang and N. Xu, Phys. Rev. Lett **84**, 2803 (2000).

[38] G. Burau *et al.*, Phys. Rev. C **71**, 054905 (2005).

[39] STAR-TOF software documentation:
http://drupal.star.bnl.gov/STAR/system/files/TOFSoftware.2.pdf.

[40] C. Alt *et al.* (NA49 Collaboration), Phys. Rev. C **68**, 034903 (2003).

[41] Heiselberg and A.-M. Levy, Phys. Rev. C **59**, 2716 (1999).

[42] A. Bialas, M. Bleszynski and W. Czyz, Nucl. Phys. B **111**, 461 (1976).

[43] D. Teaney and L. Yan, Phys. Rev. C **83**, 064904 (2011).

[44] M. Luzum and J. Y. Ollitrault, Phys. Rev. Lett. **106**, 102301 (2011).

[45] B. Schenke, S. Y. Jeon, and C. Gale, Phys. Rev. Lett. **106**, 042301 (2011).

[46] B. H. Alver, C. Gombeaud, M. Luzum and J. Y. Ollitrault, Phys. Rev. C **82**, 034913 (2010).

[47] J. Y. Ollitrault, A. M. Poskanzer, and S. A. Voloshin, Phys. Rev. C **80**, 014904 (2009).

[48] A. Adare *et al.* (PHENIX Collaboration), Phys. Rev. Lett. **107**, 252301 (2011).

[49] B. Alver *et al.* (PHOBOS Collaboration), Phys. Rev. C **81**, 034915 (2010).

[50] H. Sorge, H. Stöcker, and W. Griener, Ann. Phys. **192**, 266 (1989); H. Sorge, Phys. Lett. B **402**, 251 (1997); Phys. Rev. Lett. **82**, 2048 (1999).

[51] T. Maruyama *et al.*, Prog. Theor. Phys. **96**, 263 (1996).

[52] S. A. Bass *et al.*, Prog. Part. Nucl. Phys. **41**, 225 (1998); M. Bleicher *et al.*, J. Phys. G **25**, 1859 (1999); L. A. Winckelmann *et al.*, Nucl. Phys. A **610**, 116c (1996).

[53] Z. W. Lin and C.-M. Ko, Phys. Rev. C **65**, 034904 (2002); L.-W. Chen, C.-M. Ko, J. Phys. G **31**, S49 (2005).

[54] K. H. Ackermann *et al.* (STAR collaboration), Nucl. Instr. Meth. A **499**, 624 (2003).

[55] M. Anderson *et al.*, Nucl. Instr. Meth. A **499**, 659 (2003); K. H. Ackermann *et al.* (STAR collaboration), Nucl. Phys. A **661**, 681c (1999).

[56] F. Bergsma *et al.*, Nucl. Instr. Meth. A **499**, 629 (2003).

[57] Y. Bar-Shalom, X. R. Li and T. Kirubarajan, *Estimation With Applications to Tracking and Navigation*, John Wiley Sons (New York), 2001.

[58] K. H. Ackermann *et al.*, Nucl. Instr. Meth. A **499**, 713 (2003).

[59] C. A. Whitten, Jr. (for the STAR Collaboration), AIP Conf. Proc. **980**, 390 (2008).

[60] B. Bonner *et al.*, Nucl. Instr. Meth. A **508**, 181 (2003); W. J. Llope *et al.*, Nucl. Instr. Meth. A **522**, 252 (2004); M. Shao *et al.*, Nucl. Instr. Meth. A **492**, 344 (2002).

[61] Figures are obtained from the Brookhaven National Laboratory Flickr web page under Creative Commons Attribution-Noncommercial-No Derivative Works 2.0 Generic License; http://www.flickr.com/photos/brookhavenlab/sets/72157613690851651/.

[62] A. Schmah, private communication.

[63] F. S. Bieser *et al.*, Nucl. Instr. Meth. A **499**, 766 (2003). C. Alder *et al.*, Nucl. Instr. Meth. A **470**, 488 (2001). J. W. Harris *et al.*, Nucl. Phys. A **566**, 277c (1994).

[64] B. Christie, S. White, P. Gorodetzky and D. Lazic, STAR Note SN0175, 1994.

[65] D. Kharzeev and M. Nardi, Phys. Lett. B **507**, 121 (2001).

[66] K. Nakamura *et al.* (Particle Data Group), J. Phys. G **37**, 075021 (2010).

[67] B. B. Back *et al.* (PHOBOS Collaboration), Phys. Rev. C **70**, 021902 (2004).

[68] B. I. Abelev *et al.* (STAR Collaboration), Phys. Rev. C **81**, 024911 (2010).

[69] The online monitoring of the BBC subsystem during data-taking is accessible at http://online.star.bnl.gov/bbc/ .

[70] I. Selyuzhenkov and S. Voloshin, Phys. Rev. C **77**, 034904 (2008).

[71] J. Barrette *et al.* (E877 Collaboration), Phys. Rev. C **55**, 1420 (1997).

[72] P. Danielewicz, Phys. Rev. C **51**, 716 (1995); J. Barrette *et al.* (E877 Collaboration), Phys. Rev. C **55**, 1420 (1997).

[73] J. Barrette *et al.* (E877 Collaboration), Phys. Rev. C **56**, 3254 (1997).

[74] G. Agakishiev *et al.* (STAR Collaboration), Phys. Rev. C **85**, 014901 (2012).

[75] A. Bilandzic, R. Snellings, and S. A. Voloshin, Phys. Rev. C **83**, 044913 (2011).

[76] A. Bilandzic, Ph.D. Dissertation, National Institute for Subatomic Physics (NIKHEF), Amsterdam, The Netherlands, 2011.

[77] C. Alder *et al.* (STAR Collaboration), Phys. Rev. C **66**, 034904 (2002); N. Borghini, P. M. Dinh, and J. Y. Ollitrault, Phys. Rev. C **63**, 054906 (2001).

[78] M. Anderson, P. M. Dinh, J. Y. Ollitrault, A. M. Poskanzer, and S. A. Voloshin, Phys. Rev. C **66**, 014901 (2002).

[79] G. Wang, Ph.D. Dissertation, Kent State University, Kent, OH, 2006.

[80] Y. Pandit for the STAR Collaboration, J. Phys. Conf. Ser. **316**, 012001 (2011).

[81] J. Brachmann *et al.*, Phys. Rev. C **61**, 024909 (2000).

[82] H. Sorge, Phys. Rev. Lett. **78**, 2309 (1997).

[83] H. A. Gustafsson *et al.*, Phys. Rev. Lett. **52**, 1590 (1984).

[84] D. H. Rischke *et al.*, Heavy Ion Phys. **1**, 309 (1995).

[85] L. Adamczyk *et al.* (STAR Collaboration), Phys. Rev. Lett. **108**, 202301 (2012).

[86] Y. Pandit for the STAR Collaboration, Acta Phys. Pol. B, Proc. Supp. **5**, 439 (2012).

[87] L. P. Csernai and D. Rohrich, Phys. Lett. B **458**, 45 (1999).

[88] L. V. Bravina *et al.*, Phys. Lett. B **470**, 27 (1999).

[89] H. Stöcker, Nucl. Phys. A **750** 121 (2005).

[90] J. Xu, L.-W. Chen, C. M. Ko, and Z. W. Lin, arXiv:1201.3391.

[91] B. B. Back *et al.* (PHOBOS Collaboration), Phys. Rev. Lett. **97**, 012301 (2006).

[92] S. A. Bass *et al.*, Prog. Part. Nucl. Phys. **41**, 255 (1998); M. Bleicher *et al.*, J. Phys. G **25**, 1859 (1999).

[93] G. Agakishiev *et al.* (STAR Collaboration), BES v_2 paper to be submitted.

[94] B. I. Abelev *et al.* (STAR Collaboration), Phys. Rev. C **81**, 044902 (2010).

[95] J. Adams *et al.* (STAR Collaboration), Phys. Rev. Lett. **95**, 122301 (2005); J. Adams *et al.* (STAR Collaboration), Phys. Rev. C **72**, 014904 (2005).

[96] K. Aamodt *et al.* (ALICE Collaboration), Phys. Rev. Lett. **107**, 032301 (2011).

[97] B. I. Abelev *et al.* (the STAR Collaboration), Phys. Rev. C **75**, 054906 (2007).

[98] R. Nouicer for the PHOBOS Collaboration, J. Phys. G **34**, 887 (2007).

[99] G. Y. Qin, H. Petersen, S. A. Bass, and B. Miller, Phys. Rev. C **82**, 064903 (2010).

[100] J. L. Nagle and M. P. McCumber, Phys. Rev. C **83**, 044908 (2011).

[101] A. Adare *et al.* (PHENIX Collaboration), Phys. Rev. Lett. **107**, 252301 (2011) [arXiv:1105.3928 [nucl-ex]].

[102] J. Xu and C. M. Ko, Phys. Rev. C **84** 014903 (2011).

[103] Z. Qiu and U. W. Heinz, Phys. Rev. C **84**, 024911 (2011) [arXiv:1104.0650 [nucl-th]].

[104] M. R. Haque, M. Nasim and B. Mohanty, Phys. Rev. C **84**, 067901 (2011) [arXiv:1111.5095 [nucl-ex]].

[105] V. P. Konchakovski, E. L. Bratkovskaya, W. Cassing, V. D. Toneev, S. A. Voloshin and V. Voronyuk, Phys. Rev. C **85**, 044922 (2012) [arXiv:1201.3320 [nucl-th]].

[106] K. Dusling, F. Gelis, T. Lappi and R. Venugopalan, Nucl. Phys. A **836**, 159 (2010).

[107] H. Petersen, G.-Y. Qin, S. A. Bass, and B. Müller, Phys. Rev. C **82**, 041901(R) (2010).

[108] H. Petersen, C. Greiner, V. Bhattacharya and S. A. Bass, arXiv:1105.0340 [nucl-th].

[109] E. Retinskaya, M. Luzum, and J. Y. Ollitrault, Phys. Rev. Lett. **108**, 252302 (2012).

[110] G. Aad *et al.* (ATLAS Collaboration), arXiv:1203.3087v2 [hep-ex].

[111] M. Daugherity for the STAR Collaboration, J. Phys. G **35**, 104090 (2008); D. Kettler for the STAR Collaboration, PoS C ERP2010, 011 (2010); T. A. Trainor and D. T. Kettler, Phys. Rev. C **83**, 034903 (2011).

Appendix A

AUTHOR'S CONTRIBUTION TO COLLABORATIVE RESEARCH

In addition to the physics analysis work described in this dissertation, I have completed a number of "community service" tasks within the STAR collaboration, i.e., tasks that are of benefit to part or all of the entire collaboration. I am one of the proposers of using the STAR BBC as a reaction plane detector at lower beam energies. I participated in the repair of the BBC hardware and during STAR data-taking in 2010 and 2011, I worked as a STAR detector operator and BBC expert. My BBC hardware work included monitoring the subsystem performance and calibrating it.

In the area of community service software, I have worked on determining the first-order event plane from BBC information. I developed software that uses the hit pattern of charged particles in the BBC to open up multiple new physics opportunities for other members of the STAR collaboration.

I am among the principal authors (PAs) of a paper devoted to 9.2 GeV AuAu (this is a long paper published in Physical Review C), and my advisor and I are the sole PAs of another paper on directed and elliptic flow at 22.4 GeV (also published in Physical Review C). I am one of several PAs of a paper on elliptic flow of charged particles at beam energies between 7–39 GeV, which has been recently submitted for publication, and another jointly-led paper on triangular flow at 200 GeV is almost ready for submission. Directed flow results at 7-39 GeV (a paper based 100% on work in Chapter 5 of this dissertation) is now under review

in the Bulk Correlations Physics Working Group, and has been recommended by STAR management as a suitable paper for submission to the prestigious physics-wide journal Physical Review Letters. In my early studies, I carried out a simulation study related to BBC event plane resolution using RQMD events. The result was incorporated into a long STAR writeup now published in arXiv:1007.2613.

There are some additional data analysis projects which are still in a preliminary stage, and have not been included in this dissertation. Measurement of a signal related to possible local parity violation at lower beam energies, based on the first-order BBC event plane, and a study of beam-energy and system-size dependence of triangular flow are two such examples. Likewise, triangular flow results for identified pions, kaons and protons in 200 GeV AuAu collisions are not included in this dissertation.

I have presented invited talks or contributed presentations on this work at various conferences and workshops. I presented at the RHIC and AGS Users Meeting, June 7-11, 2010, BNL, Upton NY, at the 27th Winter Workshop on Nuclear Dynamics, Feb 6-13, 2011, Winter Park, Colorado, at the 11th International Conference on Nucleus-Nucleus Collisions (NN2012), May 27- June 1, 2012, San Antonio, TX, and at the premier conference in my field, Quark Matter 2011 (QM'11), and at Strange Quark Matter (SQM 2011). Recently, my abstract on directed flow and higher flow harmonics has been accepted for oral presentation in Quark Matter 2012 (August 2012 in Washington, DC). I am the sole listed author of the associated paper in the proceedings of WWND 2011 and SQM 2011. I have also presented a contributed short talk at the American Physical Society in 2010, and an invited colloquium at the Central Department of Physics, Tribhuvan Univ., Kathmandu,

Nepal. A selected list of publications where I am among the principal authors for papers and presentations can be found in Appendix B. STAR policy, following the normal practice of large collaborations in High Energy and Nuclear Physics, lists all authors on refereed publications strictly in alphabetical order.

Appendix B

PRESENTATIONS AND PUBLICATION

PRESENTATIONS

- **Oral Presentation:**

  "Triangular Flow of Charged Particles in Heavy Ion Collisions from STAR Experiment at RHIC" NN2012, May 27-June 1, 2012, San Antonio, Texas

- **Oral Presentation:**

  "Directed Flow of Identified Charged Particles from the RHIC Beam Energy Scan " SQM2011, September 18-24, 2011, Karkow, Poland

- **Poster** :

  "Triangular Flow of Identified Particles in Au +Au Collisions at $\sqrt{s_{NN}}$ = 200 GeV from the STAR Experiment " RHIC AGS Users Meeting, June 20-24, 2011, Brookhaven National Lab, Upton, NY

- **Poster**:

  "Directed Flow of Identified Particles in Au +Au Collisions at $\sqrt{s_{NN}}$ = 39,11.5 and 7.7 GeV from the STAR Experiment " QM2011, March 13-18,

2011, Annecy, France

- **Invited Talk** :

  " Beam Energy Dependence of Directed and Elliptic Flow Results from STAR experiment," 27th Winter Workshop on Nuclear Dynamics, Feb 6-13, 2011 Winter Park, Colorado.

- **Oral Presentation:**

  " Directed and Elliptic Flow of Charged Hadrons in Cu+Cu collisions at $\sqrt{s_{NN}}$ = 22.4 GeV", American Physical Society, 2010 Fall Meeting of the APS Division of Nuclear Physics, November 2-6, 2010, Santa Fe, New Mexico

- **Invited Talk** :

  " Directed Flow Results from STAR Experiment," RHIC and AGS Users Meeting June 7-11, 2010, BNL, Upton NY

- **Invited Talk** :

  " Heavy Ion Collisions at RHIC, STAR Experiment and Kent State University", Central Department of Physics, TU, Kathmandu, March 19, 2010

- **Oral Presentation:**

  " Directed and Elliptic Flow of Charged Hadrons at $\sqrt{s_{NN}}$ = 22.4 GeV Cu+Cu Collisions", American Physical Society, APS April Meeting 2010, February 13-16, 2010, Washington DC.

SELECTED PUBLICATIONS

- " STAR BBC as a Reaction Plane Detector at Low Beam Energies" Paper in progress (to be submitted for Nucl. Instr. and Methods)

- " Directed flow in Au+Au Collisions at $\sqrt{s_{NN}}$ = 7.7, 11.5, 19.6, 27 and 39 GeV " Paper in progress (to be submitted for Physical Review Letters)

- " Triangular Flow of Charged Particles in Au + Au Collisions at $\sqrt{s_{NN}}$ = 200 GeV " Paper in Progress (to be submitted for Physical Review C)

- " Inclusive Charged Hadron Elliptic Flow in Au + Au Collisions at $\sqrt{s_{NN}}$ = 7.7 - 39 GeV" Paper submitted for Physical Review C)

- "The Rise and Fall of the Ridge in Heavy Ion Collisions" Phys. Lett. B **705**, 71(2011) (Paul Sorensen, Boris Bolliet, Agnes Mocsy, Yadav Pandit, Navneet Pruthi)

- " Directed and Elliptic Flow of Charged Particles in Cu+Cu Collisions at $\sqrt{s_{NN}} = 22.4$ GeV" G. Agakishiev *et al* [STAR Collaboration], Phys. Rev. C **85**, 014901 (2012)

- " Beam Energy Dependence of Directed and Elliptic Flow Measurement from the STAR Experiment " Yadav Pandit(for the STAR collaboration) 2011 J. Phys.: Conf. Ser. **316** 012001 [arXiv:1109.2799v1 [nucl-ex]]

- " Identified Particle Production, Azimuthal Anisotropy, and Interferometry Measurements in Au+Au Collisions at $\sqrt{s_{NN}}$ = 9.2 GeV," B. I. Abelev *et al*[STAR Collaboration] Phys. Rev. C **81**, 024911 (2010) [arXiv:0909.4131 [nucl-ex]].

- " An Experimental Exploration of the QCD Phase Diagram: The Search for the Critical Point and the Onset of De-confinement," M. M. Aggarwal *et al.* [STAR Collaboration], arXiv:1007.2613 [nucl-ex].